UNIVERSIDADE DE
COIMBRA

Fátima Margarida dos Santos Rosa

APPLICATION OF THE EXPERIMENTAL TECHNIQUES OPTICAL MICROSCOPY, XRF, SEM-EDS AND MICRO-RAMAN TO THE STUDY OF PAINTWORKS

Dissertação de Mestrado Integrado em Engenharia Física, com especialização em Metrologia e Qualidade,
orientada pelo Professor Doutor Francisco Paulo de Sá Campos Gil
e apresentada ao Departamento de Física da Faculdade de Ciências e Tecnologia
da Universidade de Coimbra

Setembro de 2018

UNIVERSIDADE Ð
COIMBRA

FACULDADE
DE CIÊNCIAS
E TECNOLOGIA

APPLICATION OF THE EXPERIMENTAL TECHNIQUES OPTICAL MICROSCOPY, XRF, SEM-EDS AND µ-RAMAN TO THE STUDY OF PAINTWORKS

Fátima Margarida dos Santos Rosa

Dissertation submitted to the Faculty of Science and Technology (FCTUC) to bestow the Master's degree in Physics Engineering with specialization in Metrology and Quality.

Supervised by: Prof. Dr. Francisco Paulo de Sá Campos Gil

September 2018

This project was developed in collaboration with:

CFisUC

centro
de
geo
ciências
universidade de coimbra

· U C ·
Química-Física Molecular
Unidade de I&D

MUSEU
NACIONAL
DE MACHADO
DE CASTRO
CENTENÁRIO

Acknowledgements

First of all, I would like to thank my supervisor, Prof. Dr. Francisco Paulo Gil, for his guidance, enthusiasm and for such captivating conversations during the last year. I would also like to thank Dr. Virgínia da Assunção Gomes and Prof. Dr. Lídia Maria Catarino for their availability and support during this project and for providing a relaxed work environment.

I would like to extend my thanks to Prof. Dr. José António Paixão for the access to TAIL-UC, funded under QREN-Mais Centro ICT_2009_02_012_1890, to Prof. Dr. Luís Alberto Carvalho for the access to "Molecular Physical-Chemistry" R&D Unit – University of Coimbra facilities and to the "Geosciences Center" R&D Unit – University of Coimbra for lending the PXRF instrument employed during this project. A special thanks to Prof. Dr. Pedro Sidónio Silva for his assistance with the SEM/EDS instrument and once more to Prof. Dr. Lídia Maria Catarino for her help handling the PXRF instrument.

I also wish to acknowledge the National Museum Machado de Castro and the Directorate General for Cultural Heritage for the access to the artworks and the José de Figueiredo Institute, in particular Dr. Maria das Mercês Lorena Taquenho, for the extraction of micro-samples.

Finally, I would like to thank my family for supporting me, providing a great familiar environment, and helping me get where I am today. And to my friends for all the fun times and support in the last years, and in particular to Alexandre Jesus, for the hours spent reading this dissertation and all the encouragement and advice given.

Abstract

Physicochemical techniques, in particular spectroscopic, have been an important tool in the characterisation of Cultural Heritage assets. In the case of paintworks, several techniques can be easily applied due to their flat and smooth (without irregularities) surfaces. In this work, the techniques OM, PXRF, SEM/EDS and µRS are used in the analysis of pigments and gold alloys from a set of four paintings attributed to Bernardo Manuel, the last generation of painters of the Workshop of Coimbra.

The complementary use of these techniques allowed a good characterisation of the artworks, without jeopardising them. As such, PXRF was the first approach selected, allowing for both an overview of the artworks and selection of the samples for extraction. It also allowed to determine conclusively the presence of vermilion and lead tin yellow, mainly on red and yellow regions, respectively, and suggested the use of copper-based pigments to colour green and black areas, as well as red ochres in red and brown areas. The PXRF analysis also suggested the use of Flemish white in most white samples, which may be have been purposeful or a consequence of an intervention or incorrect cleaning action.

As for the µRS analysis of the samples extracted, it allowed to determine the presence of *gesso* on the preparatory layers of three of the four paintings as well as the composition of the surface layers (proteinaceous or polysacchariedeous media) and the use of green earth (*terre-verte*) as the *imprimatura* of one of the paintings. It also suggested the presence of carbon-based pigments to achieve black tones.

Regarding the study of gold alloys, SEM/EDS indicated that a high purity alloy (in general, 23 C) was employed in the four paintings, which is evidence of the importance of the Workshop of Coimbra during its last stage.

Lastly, the results obtained support the attribution of the four paintings to the same workshop/artist, although a few aspects seem to have been modified.

Keywords: Cultural Heritage, OM, PXRF, SEM/EDS, µRS, Bernardo Manuel.

Resumo

A utilização de técnicas físico-químicas, em particular espectroscópicas, tem auxiliado a caracterização de objectos de cariz cultural. No caso da Pintura, várias técnicas podem ser facilmente aplicadas devido às superfícies planas e lisas (sem irregularidades) dos objectos. Nesta dissertação, as técnicas OM, PXRF, SEM/EDS e µRS são utilizadas na análise de pigmentos e ligas de ouro de um conjunto de quatro obras atribuídas a Bernardo Manuel, a última geração da Oficina de Coimbra.

O uso complementar destas técnicas permitiu uma boa caracterização das obras de arte, sem as prejudicar ou colocar em risco. Assim, PXRF foi a primeira abordagem seguida, permitindo obter uma visão geral das obras de arte e seleccionar amostras para posterior extracção. Também permitiu determinar conclusivamente a presença de vermelhão e amarelo de chumbo e estanho, sobretudo em regiões vermelhas e amarelas, respectivamente, e sugeriu a utilização de pigmentos à base de cobre para colorir áreas verdes e pretas, assim como vermelhos ocres em áreas vermelhas e castanhas. A análise PXRF também sugeriu o uso de *Flemish white* na maioria das amostras brancas, o qual pode ter sido propositado ou consequência de uma intervenção ou ação de limpeza incorrecta.

Quanto à análise µRS das amostras extraídas, permitiu determinar a presença de *gesso* nas camadas preparatórias de três das quadro obras, bem como a composição das camadas superficiais (material proteico ou polissacarídico) e o uso de terra verde (*terre-verte*) como *imprimatura* de uma das obras. Também sugeriu a presença de pigmentos à base de carbono para obter tons de preto.

Em relação ao estudo de ligas de ouro, SEM/EDS indicou a utlização de ligas com elevado grau de pureza (em geral, 23 C) nas quatro obras, o que é uma prova da importância da Oficina de Coimbra durante os seus últimos anos.

Por fim, os resultados obtidos apoiam a atribuição das quatro obras à mesma Oficina/artista, embora alguns aspectos possam ter sido modificados.

Palavras-Chave: Património Cultural, OM, PXRF, SEM/EDS, µRS, Bernardo Manuel.

Contents

Acknowledgements **i**

Abstract **iii**

Resumo **v**

List of Figures **xi**

List of Abbreviations **xiii**

1 Introduction **1**

1.1 Context and Motivation 1

1.2 Objectives 3

1.3 Case Study 3

1.4 Dissertation Outline 7

2 State-of-the-art **9**

2.1 Physicochemical techniques in Cultural Heritage studies 9

2.2 Similar projects in Portugal 13

2.2.1 White Pigments 15

2.2.2 Black Pigments 16

2.2.3 Red Pigments 17

2.2.4 Green Pigments 18

2.2.5 Blue Pigments 20

2.2.6 Yellow Pigments 22

2.2.7 Earthy Pigments 23

2.3 The specific case of gold alloys 24

3 Techniques employed 27

3.1 Energy Dispersive X-ray Fluorescence (ED-XRF) 27
    3.1.1 Operating principle 27
    3.1.2 Sample preparation and requirements 29
    3.1.3 Advantages and limitations 30
    3.1.4 Instrumentation, settings and methods employed 31
3.2 Scanning Electron Microscopic coupled with Energy Dispersive Spectroscopy (SEM/EDS) 32
    3.2.1 Operating principle 32
    3.2.2 Sample preparation and requirements 36
    3.2.3 Advantages and limitations 36
    3.2.4 Instrumentation, settings and methods employed 38
3.3 Microscopic Raman Spectroscopy (µRS) 38
    3.3.1 Principles of operation 38
    3.3.2 Sample preparation and requirements 42
    3.3.3 Advantages and limitations 42
    3.3.4 Instrumentation, settings and methods employed 43

4 Sampling and Data Analysis 45

4.1 Sampling 45
4.2 Data Analysis 50
    4.2.1 PXRF Data Analysis 50
    4.2.2 SEM/EDS Data Analysis 72
    4.2.3 µRS Data Analysis 73

5 Results and Discussion 75

5.1 Multivariate Analysis 75
5.2 Preparatory and surface layers 80
5.3 Background layer 85
    5.3.1 *Annunciation (P25)* 85
    5.3.2 *Lamentation of Christ (P26)* 86
    5.3.3 *Apparition of Christ to the Virgin (P27)* 87

5.3.4 *Trinity (Eternal Father) (P90)* 87
5.4 Chromatic layer 88
5.4.1 White Areas 89
5.4.2 Black Areas 91
5.4.3 Red Areas 92
5.4.4 Green and Blue Areas 94
5.4.5 Yellow Areas 96
5.4.6 Brown Areas 100
5.5 Gold alloys 104

6 Conclusions **111**
6.1 Future Work 115

Bibliography **117**

A Calculated rates and clusters

List of Figures

1.1 *Annunciation (P25)* 4
1.2 *Lamentation of Christ (P26)* 5
1.3 *Apparition of Christ to the Virgin (P27)* 6
1.4 *Trinity (Eternal Father) (P90)* 7
1.5 Outline of possible altarpiece by Bernardo Manuel 8

3.1 Photoelectric absorption coefficient of Ca 29
3.2 NITON XL3t GOLDD+ XRF Analyser 31
3.3 Diagram of Scanning Electron Microscopic (SEM) 33
3.4 Schematic of Rayleigh and Raman scattering 40

4.1 Samples from *Annunciation (P25)* 46
4.2 Samples from *Lamentation of Christ (P26)* 47
4.3 Samples from *Apparition of Christ to the Virgin (P27)* 48
4.4 Samples from *Trinity (Eternal Father) (P90)* 49
4.5 Regions of PXRF spectra concerning questionable elements. 54
4.6 Example of spectra unfiltered and filtered 68
4.7 Example on how to find a peak and its parameters. 71

5.1 Factor loadings of a first exploratory PCA 76
5.2 Factor loadings of a second exploratory PCA 78
5.3 PCA results using relative concentrations 79
5.4 PCA results using rates calculated 79
5.5 Image and spectra of sample P26-3 81
5.6 Image and spectra of sample P27-5 82

5.7 Raman spectra of preparatory layers 83
5.8 Raman spectra of surface layers 83
5.9 Proteinaceous and polysacchariedeous media for reference. 84
5.10 Background samples from *Annunciation (P25)* 86
5.11 Background samples from *Trinity (Eternal Father) (P90)* 88
5.12 Raman spectra of white grains 90
5.13 Red samples from *Lamentation of Christ (P26)* 93
5.14 Green samples from *Apparition of Christ to the Virgin (P27)* 95
5.15 Raman spectra of green grains 96
5.16 Raman spectra of yellow grains 97
5.17 Sample containing Sn and Au 99
5.18 Dark yellow samples 100
5.19 Samples from the mantle of the Father *Trinity (Eternal Father) (P90)* 101
5.20 Samples of the hair of the characters 102
5.21 Raman spectrum of sample P27-9 103
5.22 Ternary diagram (Au-Ag-Cu) of gold alloys 107
5.23 Image and spectra of sample P90-3 108

List of Abbreviations

DGPC Directorate General for Cultural Heritage

EDS Energy Dispersive Spectroscopy

ED-XRF Energy Dispersive X-ray Fluorescence

ICP-MS Inductively Coupled Plasma - Mass Spectrometry

JFI José de Figueiredo Institute

IR Infrared Spectroscopy

LA-ICP-MS Laser Ablation-ICP-MS

LIBS Laser Breakdown Induced Spectroscopy

µRS Microscopic Raman Spectroscopy

µXAS Microscopic XAS

MNAA National Museum of Ancient Art

MNMC National Museum Machado de Castro

NIST National Institute of Standards and Technology

OM Optical Microscopy

PCA Principal Component Analysis

PXRD Powder X-ray Diffraction

PXRF	Portable X-ray Fluorescence
SDD	Silicon Drift Detector
SEM	Scanning Electron Microscopic
SERS	Surface-Enhanced Raman Spectroscopy
SORS	Spatially Offset Raman Spectroscopy
SR-XRF	Synchrotron Radiation X-ray Fluorescence
TAIL-UC	Coimbra Trace Analysis and Imaging Laboratory
XAS	X-ray Absorption Spectroscopy
XRD	X-ray Diffraction

Chapter 1

Introduction

This chapter focuses on establishing the relevance of studies using physicochemical techniques in the field of Cultural Heritage, specifying the goals of this dissertation and its contributions to the field. It also provides a short description of the case study and an outline of this dissertation.

1.1 Context and Motivation

Studies of cultural objects are usually focused on their origin, dating, attribution to artists or workshops, and appreciation through the ages. Stylistic and art-historical examinations, information from technological treatises and secondary literature provide reasonable assumptions, however, this approach often leaves questions unanswered, since an artwork may change drastically due to restoration attemps, storage and transportation, to name a few. Also, according to Mantler and Schreiner, "styles were sometimes copied at locations and periods completely different from those of their origin" [64]. Therefore, analytical procedures, namely pigment identification, can be very useful in dating not only the artwork but also its posterior restorations, which might be an indicator of its importance and previous allocations, and in determining the prestige of its painter, workshop and/or previous owners, suggested by the quality of materials used [64]. The use of non-local pigments may also be an evidence of trade routes, in particular when only a few sources of a mineral were known, as it is the case of natural lapis lazuli, which was inexistent in Europe and had to be exported [52].

From a restoration point of view, the identification of pigments as well as the other materials that compose a cultural asset is a critical step, given that the effects of the restoration techniques vary from material to material and may jeopardize the asset. Moreover, pigments may represent layers of previous restorations or in some cases reutilisation of canvas, and knowing their physicochemical properties is essential to revert them, exposing a more culturally valuable artwork [49]. As for conservation purposes, understanding how the pigments interact with the environment (for example, several pigments tend to darken when in presence of sulphides) is of importance in establishing how the artwork should be kept [80]. On a related note, some materials are more prone to biological organisms, such as fungus which proliferate very rapidly and can infect entire collections [105], when stored in inadequate conditions. Therefore, detecting these microorganisms and understanding how they may deteriorate existing pigments once again justifies the use of analytical methods. Furthermore, pigment identification plays a key role on verifying the authenticity of a given artwork, either by clarifying its attribution or detecting a forgery [80].

A polyptych painted by Bernardo Manuel was chosen as case study, since it represents the last stage of an important workshop (in fact, the only well documented Portuguese workshop functioning in both the 15th and 16th centuries) started by his grandfather, Vicente Gil, who was appointed royal painter by King João II, and continued by his father, Manuel Vicente. In addition to their influence in the region of Coimbra, Vergílio Correia proposed that Vicente Gil and Manuel Vicente may have been the well-known Mestres do Sardoal[1] [97]. This hypothesis is endorsed by the Câmara Municipal do Sardoal[2] [13] and the art historian Pedro Dias has attributed nearly thirty paintings to the Workshop of Coimbra, which had previously been vaguely credited to the Mestre do Sardoal [97]. As for the works of Bernardo Manuel, they are examples of the employment of Mannerism in Portugal, its influence by Italian trends (*Bella Maniera*), and how the Counter-Reformation and the independency loss of Portugal affected local painters, expressed mostly by

---

[1] The Master of Sardoal, or as it is proposed, the Masters of Sardoal were prolific painters who produced a set of seven paintings for the Church of Sardoal.

[2] Municipal Council of Sardoal.

iconography [6].

1.2 Objectives

The aplicability of the experimental techniques of Optical Microscopy (OM), Energy Dispersive X-ray Fluorescence (ED-XRF) (portable and bench-top),Scanning Electron Microscopic coupled with Energy Dispersive Spectroscopy (SEM/EDS), and Microscopic Raman Spectroscopy (µRS) will be tested in the study of several pigments present in a polyptych by Bernardo Manuel, belonging to the National Museum Machado de Castro (MNMC).

Each technique will be evaluated concerning its suitability depending on the situation, namely the extraction of micro-samples. Given the need and possibility, other techniques may be employed, such as X-ray imaging (radiography).

The expected results will be useful for the characterisation of the paintworks in terms of pigments and materials used, and allow a better understanding of the historical and economic context of the time.

A similar analysis will be provided for gold alloys, addressing, when possible, its purity and gilding technique. Moreover, this analysis is integrated in a larger project started in 2016 with the MSc. dissertation of Afonso Coxito and supervised by Prof. Dr. Francisco Gil [31], supervisor of this dissertation also.

1.3 Case Study

A polyptych by Bernardo Manuel will serve as case study. Bernardo Manuel is the third and last generation of painters from the Workshop of Coimbra, succeeding his father, Manuel Vicente, and his grandfather, Vicente Gil. He started as a scribe and possibly an illuminator in 1549, by 1567/1568 he was already a painter, having received a series of orders from the Câmara Municipal do Coimbra[3], and between 1570 and 1580 he painted the polyptych here studied for the monastery of Santa Clara-a-Velha[4]. He also carried out small works for the monastery of Santa

---

[3] Municipal Council of Coimbra.

[4] The monastery of Old St. Clare was built in the 14th century, at the behest of Saint Elizabeth, queen consort of Portugal, and later abandoned in 1677 due to frequent floods.

Figure 1.1: *Annunciation (P25)*. Image provided by MNMC.

Cruz[5] and worked on the cloister of the Sé Velha [of Coimbra][6]. Bernardo Manuel experienced the Counter-Reformation, which he expresses in his paintings.

The polyptych is constituted by four oil paintings over wood, *Trinity (Eternal Father) (P90)*, *Lamentation of Christ (P26)*, *Apparition of Christ to the Virgin (P27)* and *Annunciation (P25)*, which can be observed in Figures 1.1 to 1.4. It

---

[5] The Monastery of the Holy Cross was founded in 1131 and was later considered the National Pantheon, since it is the burial site of the first two kings of Portugal. It is still well-preserved in the centre of the city.

[6] The Old Cathedral of Coimbra was erected in the 12th century, when Coimbra was the capital of Portugal. It is a place of great importance for academic traditions, where once per year university students play *Fado de Coimbra.*

Figure 1.2: *Lamentation of Christ (P26)*. Image provided by MNMC.

portrays the Death and Resurrection of Christ, a religious theme commonly addressed by his ancestors, although he was largely influenced by Italian trends (*Bella Maniera*) and became a Mannerist painter with special attention to symbolism. Therefore, vivid colours (mostly reds and gilds) are preferred in detriment of neutrals, chronological events are displayed along three levels (more evidently in *Lamentation of Christ (P26)* and *Apparition of Christ to the Virgin (P27)*), the characters have elongated torsos, necks and faces, uncommon elements, such as a cat in *Apparition of Christ to the Virgin (P27)*, as well as multiple colours cover the floors.

Originally made for the monastery of Santa Clara-a-Velha, the polyptych was

Figure 1.3: *Apparition of Christ to the Virgin (P27)*. Image provided by MNMC.

allocated to the monastery of Santa Clara-a-Nova[7] along with the nuns in 1677 due to successive floods, becoming property of the MNMC[8] in 1915-1917. Moreover, it may have belonged to the Instituto de Coimbra[9], in-between.

As for its physical characterisation, the paintings vary in number and dimensions of clapboards: *Lamentation of Christ (P26)* and *Apparition of Christ to the Virgin (P27)* were painted on five vertical clapboards, *Annunciation (P25)* on four (vertical) and *Trinity (Eternal Father) (P90)* on seven in the horizontal direction.

In 1994, Ana Maria Goulão, then a MSc. student in Art History, proposed that

---

[7] The monastery of New St. Clare was built to allocate the Poor Clares (nuns) due to multiple floods.

[8] The National Museum Machado de Castro is an art museum in the historical area of Coimbra. It was named after the Portuguese sculptor Joaquim Machado de Castro, and actual Roman ruins can be visited on the lower floors.

[9] The Institute of Coimbra was an academy in activity between 1852 and 1982.

Figure 1.4: *Trinity (Eternal Father) (P90)*. Image provided by MNMC.

this set may have been part of an altarpiece along with two other paintings by Bernardo Manuel (*St. John the Baptist* and *St. John the Evangelist*), which had as centrepiece *Trinity (Eternal Father) (P90)*. These two paintings now belong to the monastery of Santa Clara-a-Nova, whom allowed a visit and preliminary analysis, during which Dr. Virgínia Gomes, Paint Curator of the MNMC, pointed several aspects in favour of this hypothesis. Figure 1.5 represents the possible constitution of the altarpiece and the dimensions of each element.

1.4 Dissertation Outline

This dissertation is divided in six chapters. Chapter 1 corresponds to an introduction, which includes the motivation and main goals of this dissertation; in Chapter 2, a state-of-the-art review concerning techniques employed in the study of Cultural Heritage assets and similar studies is performed; Chapter 3 addresses the

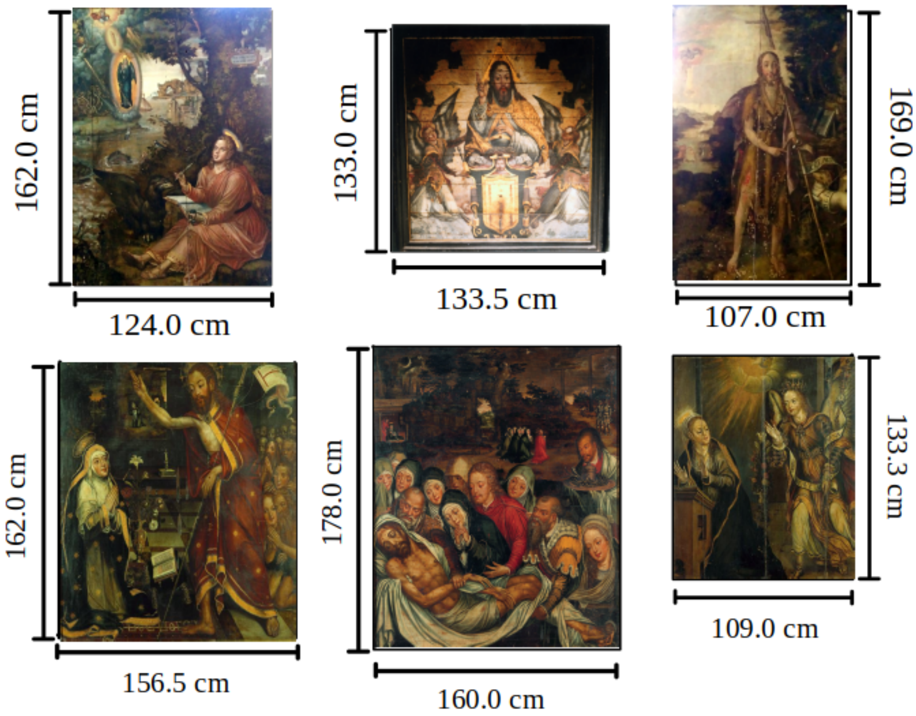

Figure 1.5: Representative scheme of the altarpiece proposed by Ana Maria Goulão with the individual dimensions of the paintworks marked; *Trinity(Eternal Father)* is displayed on the center with the images of *St. John the Evangelist* and *St. John the Baptist* on the left and right respectively, whereas, the bottom panel consists of, as seen from left to right, the artworks *Apparition of Christ to the Virgin (P27)*, *Lamentation of Christ (P26)* and *Annunciation (P25)*.

methodologies and techniques used throughout this work, reporting their advantages and disadvantages in general; in Chapter 4, the data analysis methodology for each technique is presented; Chapter 5 provides the discussion of the obtained results, in particularly regarding the chromatic layer; and lastly, Chapter 6 serves as a conclusion and proposal for future work.

Chapter 2

State-of-the-art

Cultural Heritage characterisation studies require a multidisciplinary approach and, thus, findings from other fields of knowledge, such as stylistic interpretations, should not be disregarded. In regard to physicochemical methods, consideration of the several available techniques is demanded in order to make a suitable choice.

Therefore, the following is a literature review concerning techniques and instrumentation associated, and their use in Cultural Heritage studies, focusing on the ones related to pigment identification in artworks. Next, the use of several pigments by Portuguese artists during the 16th century is discussed.

2.1 Physicochemical techniques in Cultural Heritage studies

In the characterisation of pigments, assumptions about a sample should not be derived only from elemental analysis, since multiple pigments have the same elemental composition but yet differ in their proportions and molecular bonds. Sometimes these differences result in a complete change of aspect. For example, lead sulphate, $PbSO_4$, is a white pigment while lead sulphide, $PbSO_3$, is a common impurity of black coal. Therefore, a multi-analytical method, including both molecular analysis and elemental analysis, is preferred. Among molecular analysis methods, Fourier Transform Infrared (FTIR), Microscopic Raman Spectroscopy (µRS) and X-ray Diffraction (XRD), in particular in powder form (PXRD), are nowadays the most widely used due to their versatility in characterising both organic and inorganic compounds, little to none sample preparation, reasonable price in the cases of FTIR and µRS, and valuable information regarding crystalline structures in case of PXRD. Nonetheless, identified pigments should be confirmed by means of an elemental analysis, such as ED-XRF, Laser Breakdown Induced Spectroscopy (LIBS) or SEM/EDS. The latter two can also perform morphologic analysis [80].

Regardless of the technique to be applied, observation of mounted cross sections under OM should always be performed, seeing as some knowledge on the painting techniques adopted by the painter and overpainting resulting of previous restorations can be gathered. Moreover, the structure and morphology of the sample layers can be documented [95].

Unfortunately, given the importance and fragility of the artworks studied, extraction of samples, or at times even transportation of the assets, is not feasible. Thus, in the last few years, portable instrumentation has been developed, allowing non-invasive *in situ* analysis of artworks, particularly regarding ED-XRF and µRS [80]. Still, despite portable instruments being faster and more practical, bench-top equipment is preferred in many instances, for example, when heavy elements are present on the sample or when elements exist in low concentrations [63].

With the exclusive intent of dating an asset, radiocarbon dating has been used on the study of the support (e.g. wood) and other organic media existent on paintings, although in most cases stylistic interpretation combined with literature review provides more precise assumptions [112]. The support and inner layers are also sometimes investigated using radiography, if there is reason to believe that previous restorations may have altered details of a painting [4] or if the canvas was previously used for a sketch or other artwork [49]. This technique has been particularly successful, however, it can be difficult to transport and fit large canvas in a radiography machine. Therefore, these analysis are frequently performed *in situ* using portable scanners, with the disadvantage that this may take a long time, since the scanner can only cover a relatively small area [96]. Also, for purposes other than pigment identification, such as the study of dyes, binders and oils, chromatographic techniques, atom based techniques [80] and DNA analysis techniques [118] have been employed with success.

Regarding molecular composition analysis, FTIR can operate in different modes such as Transmission, known as FTIR inasmuch as it is the classical mode, Total Reflectance (FTIR-TR), Attenuated Total Reflectance (FTIR-ATR), and Diffuse Reflectance Infrared Fourier Transform (DRIFT) spectroscopy coupled to Far Infrared (FIR). In general, all modes of FTIR are highly affected by diffuse reflection, however, this does not constitute a major disadvantage in the study of samples from paintings, since their surfaces are flat and smooth. Furthermore, all FTIR modes mentioned experience a phenomenon called Surface-Enhanced Infrared Reflection Absorption (SEIRA), consequence of the adsorption of molecules on a metal surface. In the particular case of the transmission mode, it can only be applied on thin sections, which once again is not a problem regarding pigment analysis, however, it does require sample preparation, making it susceptible to contamination. It should also be noted that, while comparing FTIR-TR and FTIR-ATR, FTIR-TR is often disregarded on the fact that it produces highly distorted spectra. Lastly, FTIR-ATR is not able to analyse sections as thin as pigment characterisation requires, unless perhaps if coupled with µRS equipment [95]. Concerning DRIFT, in [80], the authors point to a lack of use of DRIFT spectroscopy compared to other FTIR spectroscopy modes and propose as a possible reason the fact that the spectra resulting from this mode is significantly different from the ones of the other modes; in [9], it is further suggested the creation of a suitable DRIFT spectra database, which would take into account distortions from specular reflection. Moreover, this mode has more intense secondary bands (combination bands and overtones), providing more complete spectra (with a greater number of bands) [9].

The use of Raman spectroscopy in Cultural Heritage studies is more recent than FTIR [1], yet it is as prominent, if not more, as FTIR on pigment identification research with very complete and well-tested databases both printed and online [27]. As such, efforts have been made to increase its spatial resolution and to lower its detection limits, which eventually led to µRS being introduced [27]. Similar to infrared spectroscopy, Fourier Transforms were also introduced on spectroscopy (FT-Raman) in order to eliminate the fluorescence of given materials, however, it was later proved that FT-Raman merely attenuated the fluorescence, and thus, strong bands should be carefully evaluated [5].

---

[1] In the field of cultural heritage, Raman spectroscopy spectroscopy was firstly used in 1984 in France for the analysis of painted manuscripts and coloured archaeological findings [80].

In [27], the use of Spatially Offset Raman Spectroscopy (SORS), a variant of Raman spectroscopy first shown in 2005, is discussed. SORS has produced good results regarding elimination of fluorescence of the top layer, although the same cannot be said about inner layers. Furthermore, unlike the conventional Raman spectroscopy, SORS allows the differentiation of spectral contributions of the surface from those on the subsurface, even when the chemical composition of the former is unknown. Nonetheless, it cannot be used if the top layer is of metallic nature, meaning highly reflective, highly absorbing or if its constituents have Raman scattering cross-sections much higher than the target subsurface. This method has been adapted to art applications as defocused µ-SORS on account of the rather thinner layers compared to industrial or pharmaceutical applications and later improved as full µ-SORS, a modality that presents deeper penetration and better results regarding subsurface. Still, for the time being, defocused µ-SORS is chosen at the expense of full µ-SORS for its ease of implementation with conventional confocal µRS microscopes, and analytical procedures are implemented to enhance the signal of deeper layers. Moreover, defocused µ-SORS has also been reported to be capable of distinguishing mixtures of pigments from subsequent layers even through an additional surface turbid layer. As for limitations, samples heavily degraded, with multiple or highly inhomogeneous layers may produce undesirable and of difficult interpretation results. Also, contributions from extremely thin layers or middle layers with weaker Raman scatter than the top and bottom layers can be missing. For the study of dyes and lake pigments [2]. Surface-Enhanced Raman Spectroscopy (SERS) has been used in the past few years as well as FTIR [27].

Seeing as it provides vital information concerning crystallographic properties, PXRD is often complemented with ED-XRF, an elemental analysis method [18]. In [18], the authors also report more reliable chemical composition determinations when XRD and ED-XRF are combined in a single instrument, though with dedicated detectors, and a Rietveld-like approach for both XRD and ED-XRF data is performed. In substitution to XRD, X-ray Absorption Spectroscopy (XAS) is sometimes used [12].

Regarding elemental analysis techniques, ED-XRF is the most widely used, since it is non-invasive, non-destructive, multi-elemental and easily applicable *in*

---

[2] Organic pigment manufactured by precipitating dye with an inert binder.

situ, with the first portable device used in 1979 and henceforth the development of lower-power, smaller and better detectors at lower prices increased their applicability until they eventually became one of the first strategies applied in art analysis [80]. Improvements have also been made regarding elemental imaging of artworks, such as new Macroscopic X-ray Fluorescence (MA-XRF) scanners have been developed, which report good performance concerning resolution and measurement time, although lower performance when compared to bench-top 2D ED-XRF scanners. Microscopic X-ray Fluorescence (µ-XRF) is another variant widely used, in particular to visualise the elemental distribution of key elements present in multi-layers (1 µm to 100 µm) and instrumentation combining µ-XRF and µ-XRD/µXAS has been developed [96]. Concurrently, LIBS, a micro-destructive technique, has proved to be resourceful, detecting elements that ED-XRF was not able to unequivocally identify and providing a stratigraphic sequence of layers from the surface to the preparatory layer, although not excluding the use of ED-XRF [2]. SEM/EDS, which although invasive is not destructive, is one other technique employed in stratigraphic studies, including particle size, shape and distribution within layers. In addition, SEM/EDS is able to suggest the elemental composition of samples containing elements with atomic masses between 5 u (B) and 95 u (Am), presents good performance in residue analysis, and modern devices are also capable of acquiring microscopic images [28, 80]. Considering that most case studies require a large number of samples, SEM/EDS is often paired with other techniques (ordinarily µRS, if molecular analysis is preferred, or ED-XRF, for elemental analysis) and SEM/EDS results are extrapolated for all samples, meaning that sampling selection should be cautiously addressed.

Though a comparison between techniques has here been drawn, describing advantages, disadvantages and application purposes, none of these techniques should be regarded as mutually-exclusive and as many techniques as possible should be employed as a means of confirmation [18, 68, 2].

2.2 Similar projects in Portugal

In Portugal, the Directorate General for Cultural Heritage (DGPC) is the governmental institution tasked with “the management, safeguarding, enhancing, conserving and restoring" of Cultural Heritage assets [38]. In order to complete these tasks, DGPC enlisted the José de Figueiredo Institute (JFI) as the main responsible for conducting restoration interventions, carrying out preventive conservation actions and promoting research projects, among others [38].

The first Portuguese physicochemical examinations took place in 1923 due to the efforts of Carlos Bonvalot, who, also during the 1920s, convinced Herculano de Carvalho, from the Instituto Superior Técnico, to perform chemical analysis on several paintings in order to identify their preparatory layer and pigments composition [10]. In addition, João Couto, director of National Museum of Ancient Art (MNAA) during the 1930s, tried to set up an analytical laboratory, however, he was unsuccessful due to the lack of an experienced analyst [32].

Recently, the JFI has been involved in several studies concerning the analysis of pigments employed in paintings from 15th, 16th and 17th centuries[38]. Furthermore, academic research projects employing physicochemical techniques have been conducted in different fields of expertise, including Analytical Physics, Art History and Conservation/Restoration [26]. Moreover, universities have invested on state-of-the-art infrastructures, as for example the HERCULES Lab established in 2009 by the University of Évora [66]. In Coimbra, the most prominent researching institution in the Cultural Heritage field is the University in cooperation with MNMC and other infrastructures. As such, the University has several R&D Units, which cooperate with each other. In the case of this dissertation, it is integrated at Coimbra Trace Analysis and Imaging Laboratory (TAIL-UC) and counted with the collaboration of the "Molecular Physical-Chemistry" R&D Unit and the "Geosciences Center" R&D Unit.

The following is a review of the pigments used in Portugal during the 16th century, categorized by their colour, and examples of their use, for a better understanding. Note that an artwork created during the 16th century may have materials that were only synthesised in posterior centuries, since an artwork may suffer alterations. Therefore, the presence of pigments with Cr, Ti, Zn and/or Ba as major elements, indicates that an artwork as been altered or that its initial dating was incorrect.

2.2.1 White Pigments

Lead white, $2\,PbCO_3 \cdot Pb(OH)_2$, has been produced artificially since very early, and typically preferred over its mineral form, hydrocerussite, given that it can be easily prepared by mixing lead and vinegar [48]. Thereby, and taking into account its bright colour, it was the most widely used white pigment until its harmful effects were rediscovered[3] in the 20th century, when lead white was substituted by titanium white, TiO_2, which is also very bright. As for impurities in artificial lead white, usually the most significant are the elements Cu, Ag and Sn, however, in the literature reviewed none of these impurities was found.

Given that lead white is highly compatible with other pigments, it can be mixed with other pigments, including other pigments of white colour. Therefore, calcium carbonate, or calcite, $CaCO_3$, mixed with lead white in the chromatic layer was found in a painting by 16th century painter Diogo Teixeira [108], although a later study, which comprised said painting and fifteen more, did not reported it [109].

Lead was also associated to Flemish white, $PbSO_4$, which was described as a "white precipitate of lead" [48]. Although this pigment is mentioned in a technological treatise of 1795 and was sold in bottles during the 1830s, it is not considered an historical pigment [48]. Before 1795, it is not clear if it was commercially available or not, but no reference to its use in Portugal was found. Lead sulphate also exists in Nature as the mineral anglesite, which in its turn is usually associated with the mineral hydrocerussite. In Portugal, it could be extracted from several deposits, such as the Mines of Braçal and Malhada [82]. In [107], the authors refer that a lead sulphate may be found as a result of the application of ethereal peroxide in the treatment of blackened lead white.

Calcium sulphates also present a white colour and were widely used by artists of the 16th century, however, they were mostly employed along the preparatory layer. Although its white aspect remained along this layer, its composition usually varied. Thus, anhydrite, $Ca(SO_4)$, overlaid or mixed with gypsum, $Ca(SO_4) \cdot 2\,H_2O$, is normally found within the inner layer, in contact with the support. The presence of gypsum provides a less porous surface easier to paint over [6] Still, traces of calcium

---

[3] Even though, the connection between lead exposure and lead poisoning symptoms was known in late Antiquity, this knowledge disappeared during the Middle Ages [67].

sulphates were found within the chromatic layers of several paintings attributed to Francisco Correia (both painters), although, they may be due to contamination from the preparatory layer [102].

Regarding the means of identification, lead white has a high X-ray absorption coefficient and therefore techniques involving X-rays, such as ED-XRF, SEM/EDS or X-radiography, often succeed in identifying lead. Infrared Spectroscopy (IR) and µRS spectra also provide several assignments that can be attributed to lead white, such as the strong carbonate stretching vibrations and the O−H stretch. Moreover, OM allows the distinction of other pigments mixed with lead white, such as calcium carbonate [48]. As for the identification of calcium carbonates and/or sulphates, the detection of high contents of the main constituents (C, S and Ca) through an elemental analysis technique (e.g. ED-XRF and SEM/EDS) is an indicator of the use of these compounds. However, molecular analysis techniques, such as IR and µRS, yield more conclusive results.

2.2.2 Black Pigments

The most common black pigments during the 16th century were carbon-based, which can have mineral, animal or vegetable origins. In the specific case of charcoal, it can be obtained via the carbonization of wood (vegetable charcoal) or via the carbonation of bones/ivory (animal charcoal). Sometimes the term *mineral charcoal* is used, however, charcoal is not properly a mineral species, since it is always the result of the carbonation of organic matter [86].

The names of the most used black carbon-based pigments are associated with their origin. Some examples of very common black pigments are lamp black, ivory black, bone black and vine black. Given that carbon-based pigments are very easily obtained (for example, lamp black can be produced using a candle flame or an oil lamp) and do not cause degradation of other pigments, they are still being used nowadays.

The differentiation of black carbon-based pigments can be achieved, however, it is not always a goal. The presence of Ca, S and P implies the use of an animal charcoal pigment while their absence is an indication of a vegetable charcoal pigment being used. µRS has also been used successfully to distinguish black carbon-based pigments from different sources, however, the setup employed must have a high resolving power [117].

2.2.3 Red Pigments

Similarly to lead white, the artificially obtained red lead, Pb_3O_4, was favoured over its mineral form, minium, since it is easily synthetized. As a result, its use was spread around the globe and, despite its toxicity due to the presence of lead, it is still being used in the glass and ceramics industries [39]. Nonetheless, it never reached the popularity of lead white, probably due to its orange aspect, a colour not usually employed during the Middle Ages or early Renaissance. Other potential issues might have been its incompatibility with certain pigments, such as orpiment, and its darkening when in contact with atmospheric agents [39]. For these reasons, red lead was in many instances mixed with vermilion, HgS, a very bright red pigment.

As for its application by Portuguese artists, both Francisco Correia painters used it occasionally mixed with vermilion [102] and the Masters of Ferreirim may have also employed it in several paintings as the presence of lead oxide indicates [15]. Furthermore, its use in contemporary manuscripts is well asserted [84, 87, 121].

Vermilion alone was also frequently used in artworks, since it displays a brilliant and vivid aspect, ideal to colour important central figures and to represent blood. Although a sulphide, it is highly compatible with other pigments, particularly those with lead in its composition [46]. Therefore, mixtures of it were not limited to red lead, but also, for example lead white, which provides a red half tone proper of carnations [46] Also, its durability under normal light and atmospheric conditions makes its presence very common in the palette of many artists.

As for its provenance, it can be acquired by grounding the mineral cinnabar, via a rather complex dry-process or, as discovered during the 17th century, a simpler wet-process. Cinnabar is also the name given to a crystalline form expressed as α-HgS, which confers the red aspect to vermilion while the denomination metacinnabar, $\alpha\prime-$HgS, confers a black aspect. Given that the crystalline structure of the mineral cinnabar can under certain conditions interchange, vermilion applied as α-HgS may darken over time, converting to $\alpha\prime-$HgS. Still, vermilion is regarded as a permanent pigment, since under normal circumstances its darkening takes centuries, and actions can be performed to prevent the transformation to metacinnabar or even revert it [46]. However, its darkening can be much quicker if subjected to radiation in the wavelength range of 400 nm to 570 nm (violet, blue or green lights) [46], or in a chloride ion-rich environment [110]. In addition, the association of cinnabar and chloride ions may form a white degradation product, granting a greyish aspect to vermilion, a consequence of the blend of both degradation products [110].

In the Iberian Peninsula, several accounts mention the extraction of the mineral cinnabar [34] and, in fact, the largest cinnabar deposit worldwide is located nearby in Almaden, Spain. However, after the Middle Ages (from 5th to the 15th century), natural cinnabar seems to have been deemed unimportant, since the artificial form was more widely employed [34]. Therefore, synthetic cinnabar was largely imported from Holland [34].

During this review, no Portuguese artists from the 14th to the 18th centuries were found that did not use vermilion. Furthermore, the Masters of Ferreirim and Grão Vasco, among others, used it to create orange tones. The former mixed it with lead white and lead tin yellow [45] while Grão Vasco mixed it with lead white, iron oxides and aluminosilicates [25].

Regarding the identification of red lead and vermilion, it can be achieved by means of observation through OM coupled with confirmation of Pb or Hg, respectively, through a elemental analysis technique, such as ED-XRF and SEM/EDS while differentiation of cinnabar and metacinnabar requires the use of XRD [39, 46].

2.2.4 Green Pigments

During the Middle Ages and Renaissance, green pigments were mostly copper-based, since other green pigments, such as cobalt green and chromium green, were only introduced at the end of 17th century [14]. The most usual copper based green pigments were malachite, verdigris, copper resinate. In its turn, terre-verte is a green pigment containing aluminosilicates and its use is discussed in Section 2.2.7.

Malachite, $Cu_2CO_3(OH)_2$, is very similar to azurite, in fact they grow in the same ore, and it is not uncommon to find traces of azurite when inspecting malachite with OM nor for malachite to have a blueish aspect. When finely ground, malachite reproduces a pale green, and, perhaps because of that, it was not as extensively used nor referred in European paintings and written documents as azurite, and it was even described as an unsuitable pigment for oil-paintings in some technological treatises [47]. Nevertheless, it was used in Portugal by a few artists, such as Francisco Correia (the older) [102], Garcia Fernandes on *Our Lady of Assumption* [8], Gregório Lopes on *Mater Misericordiae* [7] and José de Escovar [50, 65], the latter more extensively.

Another copper-based pigment extensively used was verdigris. Regarding its preparation, verdigris can be divided in *neutral* verdigris, $Cu(CH_3COO)_2 \cdot H_2O$, and *basic* verdigris, $Cu(CH_3COO)_2 \cdot [Cu(OH)_2]_3 \cdot 2\,H_2O$, however, when no indication is given, it is assumed that it is *neutral* verdigris, since *basic* verdigris was rarely used and virtually irrelevant when studying pigments [47]. Although both types experience a change of colour (green to blue) even within the first month of application, *neutral* verdigris was dubbed *Eternal Green* and it provided the most enthralling green available until the 19th century, being for this reason often used. Unfortunately, it is also described as an incompatible pigment, which causes degradation in others forming large dark masses over time, particularly if sulphur is present. In Portugal, it was used by Grão Vasco on *St. Peter* [25] and on *Deposition of Christ in the Tomb* by artist unknown [42].

Verdigris is often misinterpreted as copper resinate, $C_{19}H_{29}COOH$, which is, in some extent, a product of the former, since its preparation involves the dissolution of verdigris in resin, providing a similar aspect, in particular when verdigris has suffered some degree of degradation. However, copper resinate is highly toxic and easily affected by atmospheric agents, making its use almost restricted to *velaturas*. Still, both verdigris and copper resinate were used to reproduce the colour green within the chromatic layer, for example on *St. Peter* by Grão Vasco [25].

Since verdigris and copper resinate are very similar, distinction between the two is not always targeted, and thereby it can be difficult to find in the available literature proof of their explicit use. Nevertheless, their identification can be accomplished by means of IR and the use of both has been successfully determined on artworks by Grão Vasco [25]. On the other hand, doubts persist related to the distinction of both on artworks by Francisco João [101] and *Deposition of Christ in the Tomb* by artist unknown [42].

Despite the predominance of verdigris until the 19th century, green hues were frequently produced by mixing yellow pigments with blue or green pigments. It can be concluded from several technological treatises [36, 11, 93] that this practice was recommended for pigments but not dyes, and therefore a mixture of azurite and lead tin yellow was ordinarily used by Diogo Teixeira [109], while the Masters of Ferreirim [15] and both Francisco Correia [102] preferred the mixture of malachite and lead tin yellow, and Francisco João [101] used verdigris as a substitute for malachite/azurite.

As for unusual pigments, brochantite, $Cu_4(SO_4)(OH)_6$, was found as a pigment on paintings attributed to the workshop of Frei Carlos, particularly in vegetation and rocky landscapes [120]. Brochantite usually presents itself as an impurity or a product of degradation of malachite or verdigris, however, in this case neither were identified, implying its deliberated use by the artists. Analysis of similar areas of paintings by contemporary artists such as Francisco Henriques and Master of Lourinhã did not yield the presence of brochantite, suggesting its use as a material signature of the Workshop of Frei Carlos [120].

2.2.5 Blue Pigments

Of the blue pigments used in 15th-17th centuries, two stand out, ultramarine blue, $(Na, Ca)_8(AlSiO_4)_6(SO_4, S, Cl)_2$ and azurite, $2\,CuCO_3 \cdot Cu(OH)_2$.

Until 1828, ultramarine blue could only be acquired through its mineral form, lazurite [92]. In its turn, lazurite is one of the minerals that compose lapis lazuli, a metamorphic rock imported to Europe from Afghanistan, which along with its vivacious colour and difficult process of extraction, made ultramarine blue a high-quality and very expensive pigment. As a result, it was not available to many artists nor patrons and it was almost exclusively employed for colouring the robes of Christ and the Virgin [92]. In Portugal, it was used by the sculptor João de Ruão [83], by the painter Nuno Gonçalves in the artwork *Polyptych of St. Vincent* [32] and in the main altarpiece of the Monastery of Jerónimos painted by Lourenço de Salzedo [34]. Due to the semi-transparent nature of this pigment, a thick layer was required, and as such, azurite was commonly applied underneath to reduce costs.

Azurite was a very common option until the 19th century [4], which was less costly and generally considered the best blue pigment after ultramarine blue despite its varying quality. About the quality of azurite, two terms are often used, *azurite* itself and *ashes* [5], the latter displaying a less intense colour and greyish aspect, and thus more economic [34]. In Portugal, azurite was mainly imported or extracted from the Aljustrel mines and it was used by virtually all painters, including Jorge Afonso, who had access to this commerce [34]. Although it is described as a permanent pigment, azurite sometimes transforms itself into malachite, a similar pigment of green colour [40].

Another important blue pigment was smalt, $CoO \cdot nSiO_2$, which is very different from the other pigments, since it has a glassy appearance, almost granting the paintings a sense of vibration. It is a very unstable pigment and it is nowadays recognized in paintings by its brown-greyish aspect [101]. However, it was cheaper than the other blue pigments and it was used by several painters including Francisco João [101], Lourenço de Salzedo [34], José Escovar [51] and António Nogueira [71].

As for unusual pigments, vivianite, $Fe_3(PO_4)_2 \cdot 8\,H_2O$, was found in the work of art *Baptism of Christ* located at the church of St. John the Baptist in Tomar, being this the only verified use in Portugal and "the first case dated from that century [16th century] published with detail" [35]. However, it is believed that its author was Flemish and that it was made in Northern Europe, where although unusual, it was found in several artworks [35]. This pigment was identified by evaluating the concentrations of iron and phosphorous by SEM/EDS and their association through examination of cross sections with OM [35].

When analysing ultramarine blue it is relevant to ascertain if it originates from a mineral source or if it is artificially, since it can be used to date an artwork as well as the importance of the patron. This differentiation can be completed using several techniques, such as µRS or LIBS, as discussed on [92]. As for azurite,

---

[4] Azurite was gradually substituted by Prussian blue after the 19th century.

[5] Given the descriptions on technological treatises, it is believed to be, or at least very similar, to verditer, a synthetic form of azurite.

a multi-technique approach should be employed, given that it is a copper based pigment and the size of its particles vary. Thereby, an elemental technique, such as ED-XRF or SEM/EDS, can be used to identify Cu and Ca, and OM to confirm the blue colour as well as the size of particles, allowing to discern between *azurite* and *ashes*, which are significantly smaller. Furthermore, a molecular technique, such as µRS or IR, can be used to identify the carbonate band.

2.2.6 Yellow Pigments

Of the yellow pigments, lead tin yellow was one of the most widely used until 1750s, when it fell into disuse for unknown reasons [74]. Similarly to lead white it provides a very bright shade, which hinders the distinction between the two. This pigment exists as two types, I and II, where the former was preferred during the 15th, 16th and 17th centuries while the latter was used before then. Lead tin yellow is identified by the presence of Sn and Pb, while the distinction between Type I and Type II is usually done by XRD, though in some occasions it has been performed through µRS analysis [42]. Moreover, its use in Portugal is well documented by both technological treatises [33] and contemporary analysis.

Given their availability, cost and stability, yellow ochres were also commonly used and reported in all Portuguese studies here researched. The colour of ochres varies greatly depending of their composition, but are usually described as yellow or red. The use of ochres is further discussed in Section 2.2.7.

As for gilded surfaces, gold was not always accessible, thus other materials and techniques were sometimes used. Given their similar aspect, orpiment, As_2S_3, was an alternative for actual gold. However, orpiment is sensible to light, of difficult drying, toxic, and highly incompatible with other materials, particularly copper or lead based pigments [74]. Orpiment was used sparsely by Portuguese painters, nonetheless it was found in *Adoration of the Shepherds* by Diogo Teixeira combined with realgar [109]. Realgar, AsS, is a pigment whose chemical composition is very similar to orpiment, has an orange reddish colour and it was also used by only a few artists, such as Gregório Lopes in *Mater Misericordiae* [7]. The Masters of Ferreirim did not use orpiment to simulate a gilded surface, but instead lead tin yellow through a technique named glazing [15]. Chalcopyrite, $CuFeS_2$, is also known as "Fool's Gold" [83], however, the only reference to its use in Portugal found in the literature reviewed was applied during later interventions in sculptures by João de Ruão, contemporary and an acquaintance of Bernardo Manuel [6].

As for gilding techniques, a review concerning studies related to gilded objects can be found in [100] and related to the characterization of gold alloys applied at the main altarpiece of the Old Cathedral of Coimbra between 1502 and 1900 in [76]. Moreover, the subject of gold alloys analysis is further discussed in Section 2.3.

2.2.7 Earthy Pigments

Earthy pigments comprehend natural occurring minerals containing clay and iron oxides that can be used for colouring. This type of pigments has been used since prehistoric times and due to its stability and durability, remains popular today [69]. Furthermore, their easy extraction and high geological availability made them very popular throughout the ages, even though they are not as vivid or spectacular as most of the pigments previously discussed. Thereby, given their trivial aspect, spread-out availability, and common chemical composition, their characterisation is not always a goal, particularly if their provenance is not being investigated.

Taking into account their composition, earthy pigments can be distinguished as green earths, formed by aluminosilicates, and ochres which are characterised by the presence of iron oxides. The colour of ochres ranges from olive yellow to dark red, with red ochres owing their colour to the mineral hematite, Fe_2O_3, and yellow ochres to both goethite, $FeO(OH)$, and hematite [69].

The formula of green earth, $K[(Al_3{}^+, Fe_3{}^+), (Fe_2{}^+, Mg_2{}^+](AlSi_3, Si_4)O_{10}(OH)_2$, also known as *terre-verte*, is due to the combination of its source minerals, glauconite and celadonite. Glauconite has a larger content of Al and lesser of Si whereas in celadonite the opposite occurs. When analysing green earth pigments, the distinction between both minerals is not always a goal, since their main difference is geological, wherein glauconite is a sedimentary mineral and celadonite has volcanic origin. Nonetheless, they have been successfully differentiated by means of IR [60] and µRS [91].

Although green earth has been disregarded for colouring in favour of copper-

---

[6] João de Ruão was the godfather of the oldest daughter of Bernardo Manuel [6].

based green pigments, as verdigris, it did find other uses. Its availability, cost and green tone, made it appropriate for underpainting in rendering flesh, and as the ground for gilding in paintings, which is known as “green bole" [69]. The only reference of green earth being used within the chromatic layer during the 15th, 16th and 17th centuries in Portugal found during this literature review (excluding Roman frescos), is the green tones in the mural paintings of the Batalha Monastery, the oldest mural paintings of Portugal [119].

Indeed, ochres were much more widely used, and their use was so common that no reference of an artist not using them was found. The Masters of Ferreirim used it extensively both in mixtures with others pigments, namely lead pigments, and in separate layers to increase opacity (similar to the application of azurite underneath ultramarine) [15, 45].

Earthy pigments are not easily identified by elemental analysis techniques, since the elements associated with them can also correspond to impurities. However, if said elements are identified and no other elements justify a certain colour, then it is plausible to assume the presence of earths or ochres. On the other hand, molecular analysis techniques, such as IR and µRS, provide better results and even allow to distinguish between different earthy pigments and minerals [91].

2.3 The specific case of gold alloys

The research concerning gold alloys characterisation can be considered a contribution to a larger project started in 2016 with the MSc. dissertation of Afonso Coxito and supervised by Prof. Dr. Francisco Gil [31]. On his dissertation, Afonso Coxito used ED-XRF and SEM/EDS, both elemental analysis techniques, to analyse gold alloys. In addition, for several samples only PXRF was used, which is highly affected by copper contributions from bottom layers. Conclusions were drawn based on historical knowledge regarding Portuguese gold networks. As for future work, Afonso Coxito proposed the use of Inductively Coupled Plasma - Mass Spectrometry (ICP-MS) to determine the isotopic nature of gold alloys.

In [16], the authors refer the main advantages and disadvantages of the analysis of gold alloys using SEM/EDS. For one, it provides the relative weights of the major elements, Au, Ag and Cu, and may also provide information regarding trace elements. Some elements, such as Pt, Pd, Te and Sn, suggest a given provenance, however, they also report the difficulty of detecting and quantifying these elements, since their peaks are very close to Au, Ag and Ca peaks, usually very slight, and, in the case of Sn, it may have been purposely mixed. Also, in [61], the ratios of Pd/Au and Pt/Au of gold alloys found in Portuguese artworks have been related to time periods and provenance, based on historical knowledge regarding Portuguese gold networks.

For the detection of trace elements, other techniques have provided more satisfactory results, such as Synchrotron Radiation X-ray Fluorescence (SR-XRF) and ICP-MS [16]. SR-XRF is a non-destructive technique that provides information on the concentration of major, minor and some characteristic trace elements of gold alloys, although it requires very expensive equipment, while ICP-MS in liquid mode requires the dissolution of the sample [7], during which Ag can be lost [62]. Using Laser Ablation-ICP-MS (LA-ICP-MS), this problem was not reported and good results were achieved [77].

Regarding gilding techniques, two seem to be of importance during the 16th century, water gilding and oil gilding. If water gilding was employed, ochres and/or clays bound in a proteinaceous medium should be expected. Moreover, the surface should be smoothed by application of anhydrite and/or gypsum, a preparatory layer commonly found during the 16th century. Oil gilding is composed of a layer of drying-oil containing pigments rich in metallic oxides. Also, the latter requires less care in the preparation and execution [76].

---

[7] Given the dimension of the sample (2 mg), it is considered a micro-destructive technique.

Chapter 3

Techniques employed

3.1 Energy Dispersive X-ray Fluorescence (ED-XRF)

Energy Dispersive X-ray Fluorescence (ED-XRF) is usually the go-to tool in Cultural Heritage studies, since it does not only provides unique information regarding the palette of the artist but also has relatively low data acquisition times [79]. During this project, it was not possible to use a bench-top equipment and, thus, only the PXRF instrument was employed. Still, PXRF is a well-established technique and, being a non-invasive *in situ* technique, allowed extensive sampling of the artworks.

3.1.1 Operating principle

The interaction between matter and high energy X-rays (80–1000 keV) mainly results in photoelectric absorption, Compton (incoherent) scattering and Rayleigh (coherent) scattering [81].

In Physics, to evaluate the probability of an event the concept of *cross section*, i.e. the effective area for collision, is used. The probability (cross section), μ_{total}, of a photon experiencing any of these phenomena is considered an attenuation coefficient, which can be obtained by the sum of the coefficients of each of the three events, as suggested by Equation (3.1). When high energy X-rays are employed, the photoelectric absorption coefficient, τ, accounts for at least 95% of the whole attenuation coefficient μ_{total} [114, 81]. Luckily, photoelectric absorption is the reason why this technique is a success while the scattering phenomena are merely collateral effects.

$$\mu_{\text{total}} = \tau + \sigma_{\text{Compton}} + \sigma_{\text{Rayleigh}} \tag{3.1}$$

Incident X-rays transfer their energy to the electrons of the sample, causing them to eject. When an ejected electron belongs to an inner orbital shell, it leaves a vacancy and the atom becomes excited. The excited state is an unstable one and as a result, the atom will reorganize itself until it returns to its fundamental state. Consequently, the vacancy left by the ejected electron is filled by an outer electron which in its turn leaves another vacancy. This process repeats itself until all the inner shells are filled, i.e. until the atom has returned to its fundamental state. Meanwhile, these transitions involve a change of energy and often fluorescent photons are emitted; other times, the Auger effect takes place [1]. The energy of the fluorescent photon emitted is equal to the energy difference between the levels in which the transition has occurred [81]. The variation of the photoelectric absorption coefficient, τ, in function of the photon energy is characteristic of each element, peaking at the existent transitions. Figure 3.1 shows the photoelectric absorption coefficient, τ, of Ca as a function of photon energy, as an example. This variation ultimately leads to the identification of the elemental composition of the sample.

In order for these events to take place, adequate instrumentation is needed. The process starts in a X-ray tube, the excitation source. The main components of the X-ray tube are its cathode and anode. The cathode is an heated filament (normally W) which controls the emission of electrons while the anode is usually an elemental metal (Cr, Cu, Mo, W, etc.). The anode is exposed to a higher potential than the cathode, accelerating the electrons against the former, and consequently, emitting a small portion of energy as X-rays.

After the X-rays interact with the sample and X-ray photons from the latter are ejected and a detector is required, in order for ED-XRF to succeed. The X-ray

---

[1] When the Auger effect occurs, the energy that should result in a photon, is transferred to another electron, called the Auger electron, which is then ejected.

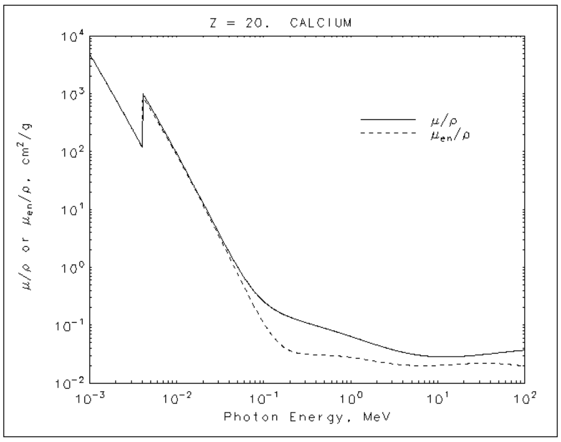

Figure 3.1: Photoelectric absorption coefficient, τ, of Ca as a function of photon energy. Taken from [90].

detector converts the energy released by the X-ray photons into electric signals. These are then readout and processed by electronics, which measure the energy released and arrival time of each event. These two devices, detector and signal processor, belong to the called spectrometer, as well as multichannel analysers, amplifiers, among others. Figure 3.2b illustrates the components of the device used, NITON XL3t GOLDD+ XRF Analyser.

As part of the instrumentation, there are also usually a digital interface with suitable spectra analysis software, a sample holder and a radiation shield for safety reasons.

3.1.2 Sample preparation and requirements

In the preparation of solid samples, the major concern is related with the surface of the samples, namely its smoothness. In the case of paintings, surfaces smoothed enough are guaranteed and therefore no sample preparation is needed. However, in order to avoid air interferences, the NITON XL3t GOLDD+ XRF Analyser was leaned against the paintings.

3.1.3 Advantages and limitations

In the following, some advantages and limitations of ED-XRF are discussed. Given that in this project only PXRF was used, some of these points only refer to it and not to the bench-top equipment.

In terms of advantages the following are worth mentioning:

- It is a non-invasive and non-destructive technique;
- It is a multi-elemental technique, providing more results in a shorter time;
- PXRF devices are lightweight, allowing *in situ* analysis;
- It provides reliable results for most elements, including base metals and main elements [103], as well as a broad range of materials, such as clays, glass and metals;
- It has low detection limits (ppm scale) for a large group of elements [103]; and
- It requires little to none sample preparation nor laboratory conditions. Furthermore, analysis of irregular and wet samples has being conducted with relative accurate results [103].

As for limitations, the following should be considered:

- It should not be used to analyse organic samples, since light elements (C, H, O, N) do not emit significant fluorescent signals;
- It does not differentiate paint layers nor the presence of the same element in multiple layers, although ratios of the K to L and L_α to L_β lines can serve as a indication of the depth of the interaction; and
- It cannot differentiate pigments with the same elemental composition, yet different molecular structure, nor pigments that only differ in the occurrence of light elements, e.g. malachite, $CuCO_3 \cdot Cu(OH)_2$, and verdigris, $Cu(CH_3COO)_2 \cdot nCu(OH)_2 \cdot mH_2O$.

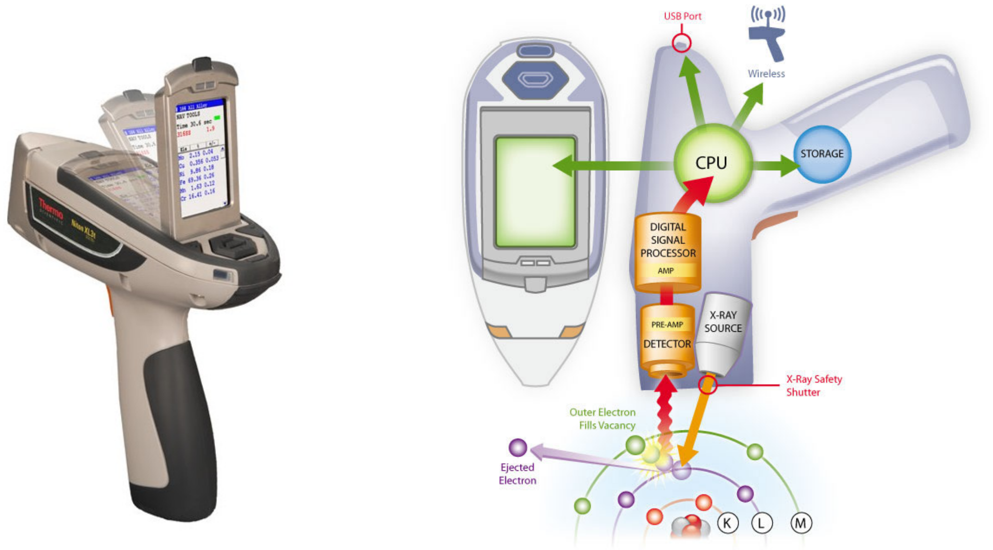

(a) Picture taken from [94]. (b) Diagram taken from [94].

Figure 3.2: NITON XL3t GOLDD+ XRF Analyser

3.1.4 Instrumentation, settings and methods employed

The PXRF analysis was carried out with a NITON XL3t GOLDD+ XRF Analyser. This device has a X-ray tube with a Ag anode (6–50 kV6-50 kV, 0–200 µA max) and a detector with Geometrically Optimized Large Area Drift Detector (GOLDD ™) technology, an upgrade to conventional Silicon Drift Detector (SDD). Figure 3.2 shows the NITON XL3t GOLDD+ XRF Analyser and its diagram.

According to [41], the NITON XL3t GOLDD+ XRF Analyser has a resolution better than 155 eV and a better performance than its predecessor, the NITON XL3t Analyser, concerning precision and analytical time, both due to its geometrical optimised SDD detector (GOLDD ™) and consequent ability to process a higher rate of X-ray counts. However, the NITON XL3t Analyser has a traditional silicon p-n diode X-ray detector, not a SDD. At a conference of The American Society for Nondestructive Testing, the director of Business Development of Thermo Fisher, James Pasmore, reports that GOLDD ™ technology shows “much higher count rates, with excellent resolution and shaping time, to produce, in general, three times better limits of detection than traditional SDD systems.” and the use of higher output currents, which can be employed due to the ability to process higher count rates, allows light element analysis without vacuum or helium purge [94]. NITON XL3t GOLDD+ XRF Analyser can operate in several modes depending of the nature of the sample, divided in categories *Metals*, *Plastic*, *Soils & Minerals*, *Consumer Goods*, *Spectral FingerPrint.* Given the composition of pigments, the category *Soils & Minerals* was chosen and in it the mode *TestAll Geo* was used, since it can test mineral and ore samples. This device also has four excitation filters to optimize sensitivity for groups of elements, which translates as four spectral ranges, the *Main Range* (for elements with $25 \leq Z \leq 83$), the *Low Range* (for elements with $22 \leq Z \leq 24$), the *High Range* (for elements with $47 \leq Z \leq 56$) and the *Light Range* (for elements with $Z < 17$) [125]. The *Light Range* is the only that operates with an He purge to avoid air interferences in the detection of very light elements (e.g., Mg, Al, Si,..) [125], however, the He purge was not used in this project. Data was acquired during 120 s, 30 s for each range, with an 8 mm collimator.

3.2 Scanning Electron Microscopic coupled with Energy Dispersive Spectroscopy (SEM/EDS)

Scanning Electron Microscopic coupled with Energy Dispersive Spectroscopy (SEM/EDS) is a resourceful and versatile technique that allows visual examination of a sample on a micro-scale. Its contribution to cultural heritage studies is extensive and it is particularly suited to analyse several layers of pigments [104].

3.2.1 Operating principle

SEM/EDS consists in the successive scanning of a sample by a finely focused electron beam in order to produce magnified images, which provides information regarding the morphology and elemental composition of a sample. Figure 3.3 illustrates the main components of a SEM (if elemental composition in a single point of the sample is to be investigated, an EDS detector is added).

First, the electrons are emitted from an electron source at a specified energy (typically in the range 0.1 keV–30 keV), accelerated to high energy throughout the anode (due to its negative nature) and manipulated by apertures, magnetic and/or

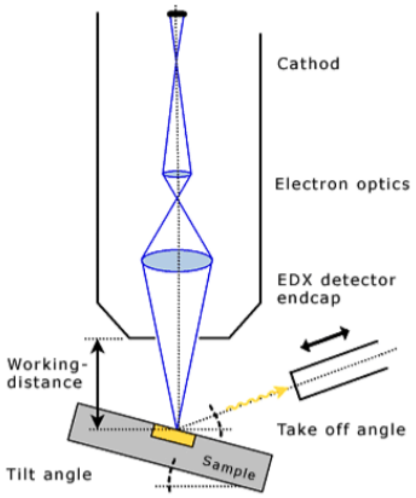

Figure 3.3: Schematic Diagram showing the main components of SEM. Taken from [21].

electrostatic lenses, and electromagnetic coils in order to reduce the beam diameter. The sample is then evaluated in a raster (x-y) pattern, and at each interaction two important effects take place, elastic scattering and inelastic scattering [57].

Inelastic scattering usually occurs when the electrons from the beam interact with the electrons from the atom. The electrons lose energy and continuum X-ray radiation is emitted, however, when too far away from the surface, the electrons are not ejected. The ejection of electrons occurs when the electrons from the beam collide with loosely bound outer electrons from the sample and these are called secondary electrons. After the ejection of an electron from the atom, an outer electron will frequently occupy the vacant energy level and thus characteristic X-ray lines are emitted. Sometimes, the Auger effect occurs, a phenomenon that also results in ejected electrons.

As for elastic scattering, it mainly results from Rutherford scattering, an interaction between the electrons of the beam and the nucleus, which can cause significant change of direction of the incident electrons. In addition, the electrons of the beam experience multiple scattering when passing through the electron cloud of the atom, which acts as a screening field for the nucleus. The electrons that have their direction significantly changed are called backscattered electrons and often have lower energy than the original beam due to several inelastic scatterings occurring deep inside the atom. Also, electrons diffuse through the sample randomly from a certain depth, which is called “depth of complete diffusion” [53].

At constant energy, the scattering cross section (probability) is proportional to the atomic number squared, Z^2, and the mean free path between scattering events decreases with increasing atomic number. Therefore, for low-Z elements, where the probability of scattering is low and the mean free path is large, only a few electrons are backscattered and hence the large majority is absorbed by the sample. Hence, high-Z elements will produce more backscattered electrons and complete diffusion will be achieved closer to the surface [53].

In its turn, image formation in SEM does not rely on optical transformation, unlike optical, given that the image is generated and displayed electronically. Thereby, at each location (x, y) the analog signal is measured and then converted to an equivalent digital value. Data packets containing the location of the beam and intensity measured (x, y, I_j), where the index j represents the various signals available (backscattered electrons, secondary electrons, among others) are then generated and stored in a matrix. To display the image, the stored data matrix is read into a corresponding pattern of (x, y) display pixels and the display brightness (“gray level”, varying from black to white) is adjusted according to the relative intensity of the measured signal [56].

To evaluate the composition of a sample, backscattered electrons are preferred given their predictable response to increasing Z and thus an “atomic number contrast” image is formed. The contrast, C_{tr}, between two locations can be calculated by either Equation (3.2), where S represents the signal measured at locations 1 and 2, or Equation (3.3), where η represents the backscattered electrons coefficient (ratio between the number of backscattered electrons and the number of electrons that enter the sample). If any of these locations is a mixture of elements, then the effective backscatter coefficient is the weighted average of the backscatter coefficients of the pure elements. Given the monotonic increase of η with atomic number, elements with consecutive atomic numbers will yield low contrast and therefore it may not be easy to form an image in the SEM, since contrasts below 10 % will require a careful approach [54].

$$C_{tr} = \frac{S_1 - S_2}{S_2} \text{ with } S_2 > S_1 \tag{3.2}$$

$$C_{tr} = \frac{\eta_1 - \eta_2}{\eta_2} \text{ with } \eta_2 > \eta_1 \tag{3.3}$$

On the other hand, topographic contrast is obtained by contributions from both secondary electrons and backscattered electrons and several components arise, such as a number component - a different number of electrons will leave the sample at each location of the raster at each time - and a trajectory component - after leaving the sample each electron travels a different path. As it is, the following effects should be considered [56]:

- The backscattered electron coefficient, η, increases gradually with the surface inclination, θ, contributing a number component to the observed contrast;
- If the surface of the sample is perpendicular to the electron beam, i.e. $\theta = 0°$, the backscattering follows a cosine distribution $n(\sigma) = cos\sigma$, where σ is measured from the surface normal, rotationally symmetric around the beam. Being a directional effect, a trajectory component arises;
- As the angle θ increases, backscattering becomes more highly directional and asymmetrical. This effect contributes a trajectory component to the contrast; and
- The secondary electron coefficient δ is related to the surface inclination as $\delta(\theta) \approx sec\ \theta$, contributing a number component to the observed contrast.

Given these effects, topography imaging is highly dependent on the electron detector, its location and solid angle of acceptance and not only on the characteristics of the sample. Therefore, topography imaging should be regarded as a qualitative approach.

Furthermore, SEM/EDS can also provide information regarding the elemental composition of a single point of the sample (similar to ED-XRF) by adding an

EDS detector. As explained before, inelastic scattering results in the ejection of an electron, which ultimately (frequently) results in the emission of characteristic X-ray lines. Therefore, a detector can be added to the setup, in order to identify and quantify the characteristic X-ray lines emitted.

3.2.2 Sample preparation and requirements

Although samples can be examined through SEM/EDS with virtually no preparation, some requirements still have to be met. For one, since SEM/EDS operates under high vacuum, the samples must be compatible with it, meaning that liquids, including water, and other volatile components cannot be studied directly. Also, in order to not contaminate the SEM/EDS sample holder, fine powder samples need to be fixed firmly to a sample holder. Lastly, if the sample is non-conductive, it will need to be attached to conductive sample holder coated with a thin conductive film of, for example, gold or palladium. Fortunately, these are not usually issues when dealing with pigments and/or gold alloys.

3.2.3 Advantages and limitations

The following are some advantages of using SEM to analyse pigments:

- It provides both morphologic and compositional information. Also, coupling an EDS spectrometer to a SEM is practical [2];
- It is a non-destructive technique, although it does require the extraction of micro-samples;
- Commercially available SEM/EDS instruments are capable of identifying lighter elements than ED-XRF[3];
- Allows elemental mapping;

---

[2] In fact, a low vacuum detector can be coupled to some SEM instruments, such as TESCAN Vega3 SBH SEM, the one used in this project [115].

[3] Recent SEM/EDS instruments are able to identify B ($m_a = 5\ u$) whereas ED-XRF devices cannot detect elements lower than Na ($m_a = 11\ u$)

- Except for non-conductive materials, it does not normally require sample preparation;

- Sample thickness is not an issue, since only the surface is evaluated (electrons do not penetrate further into the sample).

- Electron microscopes provide higher resolution than OM (values of the order of 10 nm are usually quoted for SEM/EDS commercial instruments while OM equipments have resolutions of 200 nm [58]) [4];

- Through rotation of the sample, a 3D analysis can be obtained; and

- Given the effects that take place in SEM (secondary electrons, backscattered electrons, cathodoluminescence, among others), several analytical modes are available.

As for limitations, the following should be considered:

- The images obtained are in a grey scale, unlike optical microscopy, therefore details related to colour are difficult to ascertained;

- Electron microscopes are extremely expensive as well as maintenance costs are high; and

- Some image defects may arise from various mechanisms such as charging, radiation damage, contamination, and moiré fringe effects, requiring a careful strategy and training. Sample charging occurs when a negative charge builds up at the hit location of the sample due to the absorption of electrons by the sample; irradiating a sample may damage it due to the transfer of heat; contamination may be caused by the original environment of the sample or by inadequate preparation of the sample; and, moiré fringe effects may occur when the structure of the sample has a regularly repeating pattern[55].

---

[4] The resolving power of a microscope is inversely proportional to the wavelength of incident radiation/particle.

3.2.4 Instrumentation, settings and methods employed

The SEM/EDS analysis was carried out with a TESCAN Vega3 SBH SEM equipped with BSE (annular, YAG crystal, 0.1 atomic resolution), SE (Everhart-Thornley type, YAG crystal), current (pA meter) and EDS (Bruker Xflash 410 M) detectors, belonging to TAIL-UC [28]. A 20 kV acceleration voltage was applied and data was obtained using a working distance of 15 mm to 15.1 mm. The magnification and pixel size varied from sample to sample. The acquisition time of each spectrum obtained was 60 s. Regions with dark halos or extremely bright were dismissed as charging artifacts.

3.3 Microscopic Raman Spectroscopy (µRS)

Microscopic Raman Spectroscopy (µRS) is considered an indespensable tool in the study of Cultural Heritage objects, particularly in the investigation of pigments. Moreover, it can in many situations allow the distinction of materials from their degradation products and, therefore providing a diagnostic of the conservation state of the object [27].

3.3.1 Principles of operation

The principles of operation here reviewed can be further consulted on [75].

When a monochromatic radiation (visible or near-IR) irradiates a sample, it will be reflected, absorbed and/or scattered. Light can either suffer Raman scattering, a two-photon inelastic light-scattering event, or Rayleigh scattering, a a two-photon elastic light-scattering process.

In both Raman and Rayleigh scattering, the incident photon is temporarily absorbed from an initial state (usually the ground state) into a virtual state, creating a new photon which is then scattered by a transition initiated in this virtual state. If this new photon results from the transition from the virtual state to the initial state, it is seen as an elastic scattering, called Rayleigh scattering. Given that no energy is lost, Rayleigh scattering occurs at the laser frequency, and therefore is easily identified in spectra. On the other hand, in Raman scattering, the scattered photon results from a transition from the virtual state to a state different from the initial. Therefore, it can be described as an inelastic collision between photon and molecule, where the molecule acquires different vibrational energy and the scattered photon now has different energy and frequency.

$$\mu = \alpha E \tag{3.4}$$

$$I_R \propto {v_0}^4 I_0 N \left(\frac{\alpha}{v_m}\right)^2 \tag{3.5}$$

From a classical approach, the Raman effect can be described as the interaction of an oscillating electric field. Light is classified as electromagnetic radiation, consisting of the alternation between electric and magnetic fields, and due to its interaction with the charged particles of the molecule, an induced dipole moment is produced. Equation (3.4) describes how the induced dipole moment, μ, the incident electric field, E and molecular polarizability, α, i.e. the ability of the electron cloud of a molecule to be distorted from its normal shape by an external field, are related. Both E and α may vary with time and consequently so may μ. On one hand, the electric field E oscillates at a frequency v_0, which may induce an oscillation of the dipole moment μ of the molecule at the same frequency, v_0; on the other hand, the polarizability α may vary slightly with time at the molecular vibrational frequency v_m, much slower than v_0. Figure 3.4 illustrates the frequencies v_0, v_m and the combination of both. It also depicts the Rayleigh frequency as only v_0, since no energy is transferred to the molecule, Raman anti-Stokes frequency as the sum $v_0 + v_m$ and Raman Stokes frequency as the difference $v_0 - v_m$. Stokes and anti-Stokes are two types of Raman scattering, where Stokes Raman scattering corresponds to the transition from a vibrational state (usually the ground vibrational state) to a more excited state and anti-Stokes Raman scattering corresponds to the transition from a vibrational state to a less excited vibrational state (usually the ground vibrational state). The intensity ratio of the Stokes relative to the anti-Stokes Raman bands depends on the absolute temperature of the sample, and the energy difference between the ground and excited vibrational states, being de-

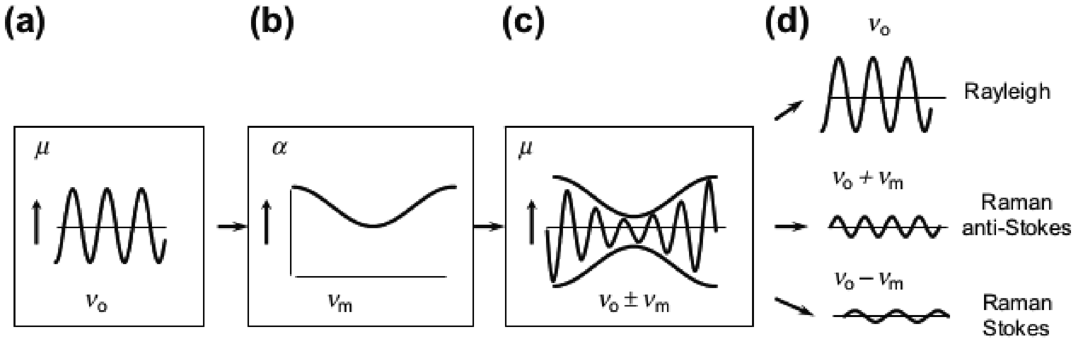

Figure 3.4: Schematic representing Rayleigh and Raman scattering, Stokes and anti-Stokes, in function of v_0 and v_m. Taken from [75].

scribed by Boltzmann law at thermal equilibrium. Since at ambient temperature most molecules are found at the ground state, the Stokes Raman lines are naturally much more intense than the anti-Stokes. As for total Raman intensity, even from a classical point of view is quite complex, and thereby Equation (3.5), which only proposes a proportionality, is more straightforward. In it, the intensity of the Raman scattered radiation I_R is proportional to the number of scattered molecules in a given state, N, to the frequency of the exciting laser, v_0 and to the incident laser intensity, I_0. Since Raman scattering only occurs when the polarizability α oscillates at frequency v_m, the last term, α/v_m is added. The proportionality with N allows the identification and quantification of molecules (concentration).

In Figure 3.4(a) the incident radiation makes the induced dipole moment of the molecule oscillate at the photon frequency; in (b) the molecular vibration can change the polarizability, α, which changes the amplitude of the dipole moment oscillation; the result, as shown in (c), is an amplitude modulated dipole moment oscillation; and the image (d) shows the components with steady amplitudes which can emit electromagnetic radiation.

In order for the Raman effect occur and be detected, suitable instrumentation is needed. Thus, a µRS instrument consists of a laser excitation source, a spectral analyser, a detector and collection optics. There is a wide choice of laser excitation sources commercially, since the suitability of each depends on the experimental setup and the material to be studied. One important choice is related to the laser wavelength. Higher wavelengths, which are less energetic, have less scattering efficiency, meaning that higher power lasers or longer integration times may be required for any bands to be visible. At low wavelengths, the fluorescence may be too intense, covering the whole spectrum, and therefore no bands are visible. Regarding pigment analysis, a low frequency of 532 nm provides good results according to [24], however, the coating layer and other binding medias, can cause high levels of fluorescence, not allowing the identification of the materials analysed [44].

In the spectra analyser, the radiation is spatially separated into monochromatic components. The light enters through a slit and is reflected by a mirror, ensuring that the light moves in parallel directions. Next, in the monochromator, the light is sorted spatially into its monochromatic components using a diffraction grating. A diffraction grating is composed by many parallel lines (or grooves) spaced at a distance similar to the laser wavelength employed and bends the radiation by an angle depending on the wavelength. Each component is therefore diffracted by the diffraction grating with a certain path length difference. Light with a certain wavelength is focused onto the exit slit, where the radiation will be in-phase for only the selected wavelength. This radiation and its multiples constructively interfere and finally pass through the exit slit. When radiation of different wavelength reaches the exit slit, it will suffer destructively interference, and be discarded.

For the detection of the light that leaves the monochromator a compromise must be made between spectral resolution and spectral range. One way to get good spectral resolution in a somewhat large range is to use array detectors and multi-channel equipment. Array detectors are usually photodiode arrays or CCDs (charge-coupled-devices), where each element or pixel records a different spectral band and sends it to an unique channel. The information of each channel is gathered and a high resolution Raman spectrum is achieved.

Given that the Raman effect is inherently weak it is fundamental that the maximum radiation possible is scattered and collected efficiently. To do so, an optical microscope is coupled to a µRS spectrometer, allowing to inspect a magnified image of the sample to select and focus the laser on a specific grain. Collection optics also comprehend systems of mirrors and fibre-optic components.

3.3.2 Sample preparation and requirements

Solid samples, in most cases, do not require any sample preparation. Similar to PXRF analysis, best results are achieved when the surface of the sample does not present irregularities. Fortunately, the samples analysed during this project are both solid and smooth.

One other aspect that leads to better results, in respect to pigments analysis, is the removal of coating from a sample, however, this is nearly impossible when samples are as small as the ones in this project.

3.3.3 Advantages and limitations

Next, a few advantages and limitations of µRS analysis are discussed. Given that it is not feasible to discuss all, these only pertain to the samples investigated.

As for advantages, the following should be considered:

- It is a non-destructive technique, assuming that the samples do not suffer degradation and even then it is usually in a single microscopical spot;
- It is suitable to analyse both organic and inorganic materials;
- It is suitable to analyse hydrated samples;
- It is suitable to analyse very small samples (<1 µm in diameter); and
- The recording of the spectra is very quick, even with several accumulations.

In terms of limitations, and particularly in the samples analysed in this project, the following are worth mentioning:

- It is not suitable to analyse metals nor alloys;
- The detection of bands can be rather difficult, since the Raman effect is very weak;
- Fluorescence of certain materials, such as coatings or impurities, can hide relevant bands; and
- It may cause degradation due to sample heating once it is irradiated by an intense laser.

3.3.4 Instrumentation, settings and methods employed

For the µRS analysis, the equipment WITec Alpha 300R was employed. It is equipped with a 532.115 nm green laser and its power is adjustable. Spectra were collected using ×10 and ×100 objectives, with integration times from 10 s to 30 s and 3 to 10 accumulations (depending on the samples). As for the detector, it is an array of charge-coupled-devices (CCDs) with a diffraction grating of 600 grooves mm and blazed wavelength of 500 nm. Moreover, the detector is cooled to −60 °C.

Procedures such as the calibration of the equipment and calculation of spectral resolution by inspection of the FWHM of a single band were not executed in this project, since they already had been performed by the researchers of the "Molecular Physical-Chemistry" R&D Unit – University of Coimbra, to whom this instrument belongs, however, the resolution of the instrument is unknown. From a theoretical point of view, the resolving power can be deduced by applying the Rayleigh criteria, expressed in Equation (3.6). In it, the resolving power, R, for the first diffraction order ($n = 1$) is equal to the total number of grooves illuminated, N. Moreover, $\Delta\lambda$ represents the resolvable wavelength difference at the wavelength λ. Unfortunately, the length of the diffraction grating is not known, but assuming a length of 10 mm, the resolving power is equal to $R = 6000$, and at, for example, a wavelength $\lambda = 600\ nm$, the resolvable wavelength difference is $\Delta\lambda = 0.1\ nm$. In Raman shift units, it corresponds to $2.77\,\mathrm{cm}^{-1}$, meaning that if two bands exist simultaneous in a spectrum at $2130.33\,\mathrm{cm}^{-1}$ and $2133.10\,\mathrm{cm}^{-1}$, they are (theoretically) distinguishable.

$$R = nN = \frac{\lambda}{\Delta\lambda} \tag{3.6}$$

Although Equation (3.6) provides a reasonable estimate, it does not take into account many factors, such as the slit width. Furthermore, other studies, [3, 20], using a similar setup reported a spectral resolution of $\sim 4\,\mathrm{cm}^{-1}$.

Chapter 4

Sampling and Data Analysis

In this chapter, the procedures of sampling and data analysis for each technique are discussed.

The sampling process was performed in order to be representative but not damaging to the artworks. As for the data analysis, each type of data was treated differently and user guides were consulted for further indications on how to interpret the data.

4.1 Sampling

PXRF was the first approach used in this project since it is a non-destructive and non-invasive technique, allowing an overall investigation of the subjects studied. As such, sampling using PXRF was more exhaustive than with the other two techniques employed (µRS and SEM/EDS). Therefore, one hundred and eighty five samples were collected using PXRF, covering the different aspects and colours of each painting. Moreover, given that in PXRF analysis it is not possible to distinguish the contributions from different layers, several samples were acquired in situations where it could be reasonably assumed that a pigment had been applied over other pigment. Figures 4.1 to 4.4 show the points sampled in each painting. Note that, in the figures the points sampled (white marks) are enumerated simply as 1,2,3,..., however, when referred during the text they are denoted as pxrf-inventory number of the painting-sample number. Also, the marks on the figures may cover some details, thus, if needed, the figures on Section 1.3 should be consulted.

Figure 4.1: Samples obtained using PXRF, at white, and samples extracted, at blue, from the painting *Annunciation (P25)*. Original image provided by MNMC.

The analysis of the samples obtained by PXRF provided new insights for which samples should be extracted for µRS and SEM/EDS analysis. The points where micro-samples were extracted are marked in blue in Figures 4.1 to 4.4 as `S1,S2,S3,...`, although throughout the text these samples are denoted as `inventory number of the painting-sample number`. It should be noted that samples were extracted in convenient regions, at flaws or at intersections of the boards, in order to not jeopardize the works of art. Table 4.1 summarizes the number of sam-

Figure 4.2: Samples obtained using PXRF, at white, and samples extracted, at blue, from the painting *Lamentation of Christ (P26)*. Original image provided by MNMC.

ples acquired using a non-invasive approach, meaning PXRF, and using invasive approaches, meaning SEM/EDS and µRS.

Since the study of gilded areas is of major importance in this project and future work, areas containing gold were sampled and examined with SEM/EDS. These correspond to samples P25-3, P25-4, P26-3, P27-3, P27-4, P27-5, P27-8, P90-3 and P90-4. Also, areas of carnations, both light and shade, were sampled to test the hypothesis that shade carnations were obtained by applying a carbon-based pigment, which is not detected by PXRF. Thus, samples P25-1, P26-1, P27-1 and P90-1 correspond to light carnations whereas samples P25-2, P26-2, P27-2 and P90-2 to darker ones. Lastly, areas where the results of PXRF were inconclusive

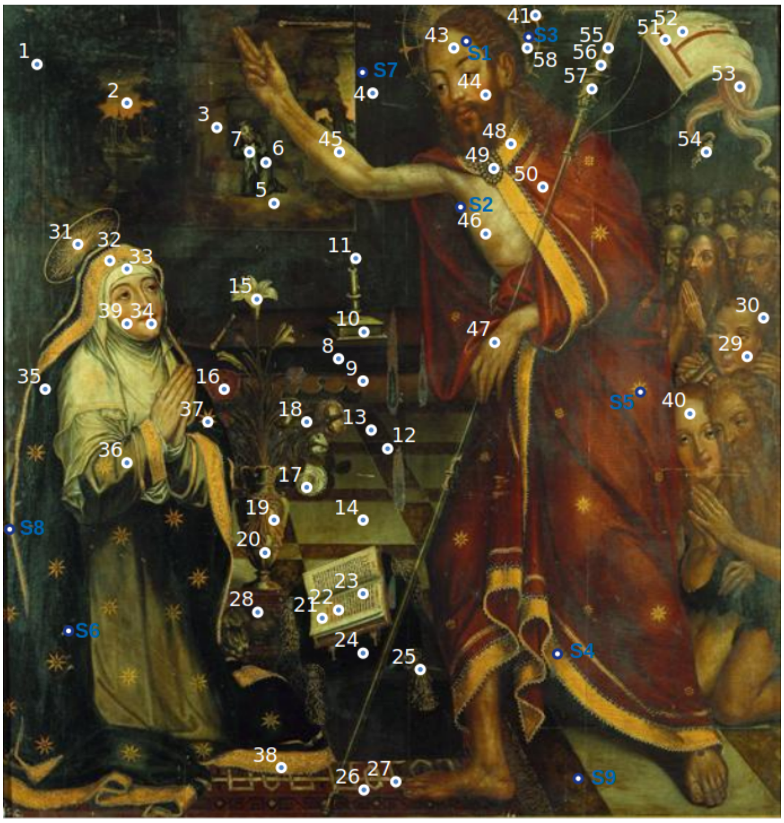

Figure 4.3: Samples obtained using PXRF, at white, and samples extracted, at blue, from the painting *Apparition of Christ to the Virgin (P27)*. Original image provided by MNMC.

and the extraction of samples did not endangered the artworks were also sampled. This includes all other marked points on Figures 4.1 to 4.4.

All extracted samples were observed and photographed using OM. Moreover, all samples were investigated with µRS, with the exception of samples containing gilded layers.

Figure 4.4: Samples obtained using PXRF, at white, and samples extracted, at blue, from the painting *Trinity (Eternal Father) (P90)*. Original image provided by MNMC.

Table 4.1: Number of samples acquired using invasive and non-invasive techniques per artwork.

	P25	P26	P27	P90	Total
Non-invasive	50	47	57	31	185
Invasive	8	5	9	7	29

4.2 Data Analysis

The data analysis depends on the type of data, but also on its characteristics, such as signal-noise ratio. Thereby, the data acquired by the three equipments employed was treated differently. The following sections describe the data analysis used for each technique.

4.2.1 PXRF Data Analysis

The PXRF analysis provides two sets of data, qualitative and semi-quantitative. However, the user guide refers three types of data: qualitative, semi-quantitative and quantitative. It does not offer any explanations other that "if the relative error is greater than 20 %, the result is considered qualitative or semi-quantitative at best" [125]. In [127], the authors refer that the term *semi-quantitative* is not used in a uniform way and that, through the use of matrix correction algorithms, *semi-quantitative* results can produce *quantitative* results. Moreover, *Bruker*, a competitor of *Thermo Fisher*, refers that in order to acquire quantitative data a calibration is required while semi-quantitative data only requires the number of counts per element (net peak area). Also, it describes the semi-quantitative data as "appropriate in situations where a calibration and/or samples of known concentrations do not exist, but comparing the samples in terms of element concentration is necessary" [22].

As for the qualitative data, i.e. the spectra, it is not clear if they are submitted to some kind of pre-processing, such as baseline correction and noise filtering, since the *bremsstrahlung* radiation present in these spectra is not as significant as in the spectra from SEM/EDS analysis [1]. However, the available user guide of the instrument, [125], does not indicate that any of these processes take place.

As for the quantitative analysis, when executed on mode *TestAll Geo*, it corresponds to a Compton normalisation of elements with low concentration and application of a Fundamental Parameters calibration for higher. Unfortunately, this quantification process occurs in a non-supervised manner, the threshold for choosing which method is not known and neither are the parameters for applying

---

[1] The *bremsstrahlung* radiation may be attenuated due to the excitation filters used [59].

the methods. In the case of the Fundamental Parameters calibration, it is also unknown which algorithm was applied to account for the matrix effects. Furthermore, the detection and posterior quantification of some elements raises doubts, which once the matrix effects are accounted, induces errors.

One other issue may be related to noise being misinterpreted as a peak. The distinction between noise and relevant information is related with how the peaks are investigated. Unfortunately, the user guide of this device, [125], is not clear on how the peaks are investigated, meaning that it does not specify if the monotony of a region is checked or if the region around the tabulated peak is integrated and used for the posterior quantification. If the monotony is checked, then it must have some kind of mechanism to distinguish noise from slight peaks (an intensity threshold, a minimum number of points, the application of a filter,...); otherwise, it could wrongly account for elements due to noise or overlapping with other peaks. Nonetheless, in several instances where noise seems to have been misinterpreted as relevant peaks, the quantitative analysis provided by the PXRF device reported relative errors larger than 20%, which suggests that these elements should have been excluded from the quantitative analysis [125]. Unfortunately, as referred before, they were not and, thus, the overall results present low reliability [89, 88].

Section 4.2.1 shows a detailed analysis of which elements seem to have been correctly identified. It also specifies for each element, how many samples showed relative errors equal or greater than 20 %. Also note that in all samples more than one element showed relative errors equal or greater than 20 %.

Issues regarding the accuracy of the quantitative results given by this instrument were also found by other researchers. In [19], the authors compare the performance of different PXRF instruments, including of the NITON XL3t GOLDD+ XRF Analyser, using a National Institute of Standards and Technology (NIST) reference material, NIST 2709a, which has a silica-dominated matrix. The results show that the “accuracy in measuring a basic suite of elements on a well constrained, standard reference material in both mining and soil modes is poor to very poor”. However, it is not clear if the source of the inaccuracy is instrumental or related to the software. In one other report, [113], where the *Mining* mode was used, the source seems to have been instrumental, since, for example, Zn and Cu were correctly quantified in a different mode (*Zn-Cu Mining* mode). The performance of a similar device (contemporary without GOLDD ™ technology) was studied on [78] on soil chemistry analysis, showing once again poor accuracy in the detection and quantification of elements when compared to a bench-top equipment. The authors of the three documents agree that the accuracy could probably be improved by using different calibration settings. Nonetheless, the quantitative results obtained by this instrument indicate that it has good precision and high reproducibility.

Although, some spectral artefacts may exist throughout the spectra, this instrument provided well defined spectra, which are essential for this project, even in cases where the concentration of a given element was expectedly low (e.g. in fine drawings). Thereby, the conclusions drawn upon the spectra seem reliable and the relative intensities normalised to the Ag L_3M_5 peak or to the Ag KL_3 (depending on the spectral range used), also known as *rates* (R), can be used to drawn conclusions. This process provides semi-quantitative data, allowing the comparison of the same element in different samples [22, 73] and is described in Section 4.2.1.

Issues found related with automatic peak identification

As referred before, the misidentification of elements is a quite serious and almost unavoidable problem. Since the quantitative process executed by the PXRF is an automatic non-supervised one, including the identification of elements, this section provides a detailed account of the issues related with the identification of each identified element. As for the quantification, it is more difficult to ascertain if it is correct, since it is not possible to deduce the quantification of each element by observation of the spectra.

This section reports the number of samples of the sample set that contain a particular element and of these, how many show relative errors equal or greater than 20 %, since the results with such large errors are commonly excluded from the quantitative analysis [125]. Reasons why or why not each element should be considered in further discussions are also presented. For each element, the spectra were examined, particular those showing largest relative concentrations and/or smallest relative errors, and a few are shown in Figure 4.5, where the spectra of the grid that held some of the paintings is also shown, when relevant. Moreover, the elements are presented in the order in which they are given in the file acquired from the device and not by increasing Z and tabulated values of X-Ray transition energies presented here were taken from [126].

The following analysis shows that a high number of elements seem to have been wrongfully identified. Moreover, it seems that large errors are correlated with ill-defined peaks and misinterpretation of noise. As a result, it can be concluded that only the elements Pb, Au, Hg, Cu, Fe, Ca, K, S, Sn, Al and Si are to be considered reasonable identified.

Mo ($Z = 42$)

The element Mo was detected in fifteen samples and of these, four samples show a relative error equal or greater than 20 %.

According to the user guide of the device,[125], Mo should be investigated using the *Main Range*, however, the expected main peaks, at 17.442 keV and at 19.601 keV, were only found on the *High Range*. Moreover, these peaks are present in all *High Range* spectra of the complete sample set and also on the spectrum acquired from the grid that held the paintings *Aparição* and *Trinity (Eternal Father) (P90)*, meaning that they may be due to systematic errors.

There is also the possibility that the Mo L_3M_5 at 2.293 16 keV has been identified. However this raises three issues: if Mo is present, then its typically more intense peaks should appear in the spectra using the more sensitive excitation filter (*Main Range*); once more, it is not clear how the peaks are investigated by the PXRF instrument, since it argues that a specific excitation filter (range) is more sensible to certain elements and at the same time uses other ranges in their detection and quantification and, without knowing how the peaks are deconvoluted, it is very difficult to be certain that Mo was correctly accounted.

Given that the process of detection of Mo is unclear, the presence of Mo is not discussed in further sections.

Sr ($Z = 38$)

The element Sr was detected in sixty-eight samples and of these, sixteen samples show a relative error equal or greater than 20 %.

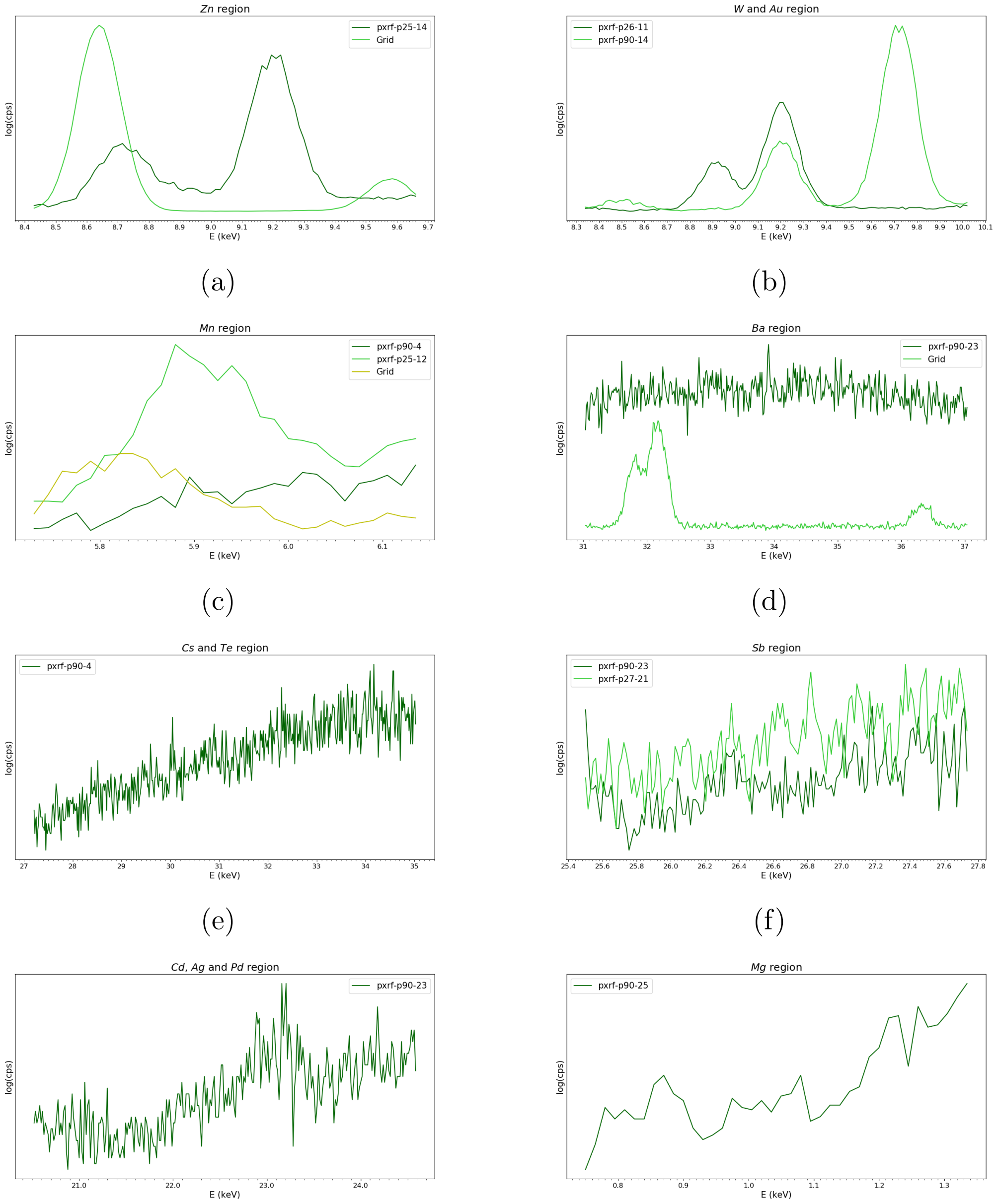

(a) (b)

(c) (d)

(e) (f)

(g) (h)

Figure 4.5: Regions of the PXRF spectra concerning the elements Zn, W, Mn, Ba, Cs, Te, Sb, Cd, Pd and Mg in samples where their relative concentration was maximal.

In the *Main Range* spectra of the complete sample set an ill-defined peak was found at $\sim$ 14.12 – 14.24 keV, with its position varying, meaning that it may have varying causes. Still, in this range of energies, it can be assigned to the Sr KL_3 transition, however, no other peaks related to Sr were found. It can also be assigned to other elements such as Hg, Au and Kr.

Given that is not possible to verify the identification of Sr, Sr can be excluded from further discussions, still it is included in an exploratory Principal Component Analysis (PCA) analysis.

Rb ($Z = 37$)

The element Rb was detected in sixty-three samples and of these, forty-eight samples show a relative error equal or greater than 20 %.

The Rb KL_3 transition is tabulated at 13.375 keV and a slight peak is found close to this value in all *Main Range* spectra of this sample set. However, the Pb L_1M_5 transition is tabulated at 13.377 keV, being safe to assume that it contributes to the quantification and even identification of the element Rb.

Given that in the majority of samples where Rb was identified the quantification of Rb shows large relative errors and that the main peak can be assigned to Pb, Rb is not considered in the following sections.

Pb ($Z = 82$)

The element Pb was detected in all samples of the sample set with a maximum relative error of 3.5 %.

The detection of Pb does not raise doubts, since it can be confirmed by several peaks.

Au ($Z = 79$)

The element Au was detected in twenty-four samples and of these, only one shows a relative error equal or greater than 20 %.

Au seems to have been misidentified in three instances, sample `pxrf-p90-7`, which has a relative error of 31.0 %, and samples `pxrf-p90-6` and `pxrf-p25-14`. The spectra of these samples do not show the expected peak at 9.7133 keV nor any other that can been assigned to Au. Also, the samples do not have a gilded or yellow aspect. Instead, the samples are of red colour and their spectra show several peaks that can be assigned to Hg, including the more intense peak, corresponding to the Hg L_3M_5 transition, at 9.9888 keV. Moreover, the quantitative analysis provided by the PXRF device found the concentration of Hg below the limit of detection, meaning that in these cases both Au and Hg were misidentified.

In the case of sample `pxrf-p27-19`, its spectrum shows the presence of Au, however the quantitative analysis found its concentration below the limit of detection.

In sum, there are instances where Au was certainly misidentified instead of Hg, which is a concerning situation, since these elements are very important to the aspect of the sample. Still, due to its importance in this project, Au is mentioned in the following sections. Nonetheless, note that most results related with Au discussed throughout this dissertation were acquired using SEM/EDS and not PXRF.

Se ($Z = 34$)

The element Se was detected in one hundred and nineteen samples and of these, one hundred and five samples show a relative error equal or greater than 20 %.

No peaks that could have been assigned to Se were found in any range of any spectra.

As a result of the high relative error associated with Se (sample `pxrf-p27-22` has the minimum value with 15.3 %) and the fact that no peaks associated with Se were found, it can be concluded that the identification was due to noise. Therefore, the presence of Se is no further discussed.

As ($Z = 33$)

The element As was detected in all samples except one (`pxrf-p90-26`) with relative errors ranging from 1.7 to 11.9 %.

Although the quantification of As shows small relative errors, As was misidentified due to its main peak, As KL_3 at 10.5318 keV, overlapping completely with the main peak (in the range of energies studied) of Pb, Pb L_3M_5 at 10.5515 keV. Also, the spectra analysis did not provided any other peaks that can be assigned to As.

As a result, As is not considered in further discussions.

Hg ($Z = 80$)

The element Hg was detected in one hundred and nineteen samples and of these, fifty-two samples show a relative error equal or greater than 20 %. For an element as important as Hg, since its presence is associated with a single pigment, vermilion, such a high number of samples showing relative errors greater than 20 % is highly concerning.

Hg seems to have been misidentified in sixty-three instances, however, fifty-two of these samples show relative errors equal or greater than 20 %. This conclusion was drawn after inspection of the PXRF spectra in all ranges, although in [125] the *Main Range* is referred as the most sensitive to Hg, and no peaks that could have been assigned to Hg were found. Moreover, in several of these samples the peak at 9.7133 keV assigned to Au was found and was correctly identified as such.

There were also eleven instances where several peaks of Hg were found, but the semi-quantitative analysis found their concentration below the limit of detection. Two of them were already referred when discussing the identification of Au.

Still, due to its importance in the study of pigments, Hg is referred in further discussions.

Zn ($Z = 30$)

The element Zn was detected in one hundred and twenty one samples and of these, sixty-seven show a relative error equal or greater than 20 %.

Zn was identified in fifty-eight samples (e.g. `pxrf-p25-14`) due to a secondary peak of Hg (Hg L_3M_1 transition at 8.721 keV) while the Zn KL_3 transition is expected at 8.638 86 keV and of these, only twenty-seven have relative errors greater than 20 %. Moreover, the peak in the spectra is centred at ~8.71 keV and the spectra lack secondary family members/peaks of Zn. Figure 4.5a shows the region of interest of Zn in the spectra of sample `pxrf-p25-14`, the sample of the sample set reporting the largest relative concentration and relative error less than 20 %.

As for the other sixty-three samples, forty show relative errors greater than

20 %, can hardly be classified as peaks (they seem more to be noise) and even if they are, they look centred at ~8.46 keV, not 8.638 86 keV. Moreover, the grid that held some of the paintings had Zn in its composition (confirmed by several peaks) and the more intense peak in its spectrum had a defined aspect centred at 8.639 keV.

Therefore, Zn is not considered in further discussions and is considered non-present in all samples.

W ($Z = 74$)

The element W was detected in seventy-six samples and of these, fifty-three show a relative error equal or greater than 20 %.

All samples with relative errors smaller than 20 %, with the exception of sample `pxrf-p26-11`, have Au in their composition. Moreover, the peak presents itself at ~8.48 keV, which is closer to the Au L_3M_1 transition tabulated at 8.4939 keV than the W L_3M_5 transition tabulated at 8.3976 keV.

In the case of sample `pxrf-p26-11`, it does not show any peak from 8.3 keV to 8.7 keV, and thus it is not clear how the element was identified in this sample. Its spectrum in the region of interest can be seen on Figure 4.5b along with the spectrum of sample `pxrf-p90-14` which reports the smallest relative error and contains Au.

Therefore, the element W is considered not present throughout the sample set and is not included in further discussions.

Cu ($Z = 29$)

The element Cu was detected in one hundred and eighty three samples of the sample set and of these, twenty two show a relative error equal or greater than 20 %.

There are fourteen samples where Cu seems to have been misinterpreted due to noise. However, all of these show relative errors ranging from 21.3 to 42.1 %.

Still, Cu was correctly identified and confirmed through the presence of secondary peaks assigned to Cu in most instances, and therefore it is considered in further discussions.

Ni ($Z = 28$)

The element Ni was detected in sixty-five samples and of these, sixty-three show a relative error equal or greater than 20 %. Moreover, the other two samples, `pxrf-p90-1` and `pxrf-p90-8`, have relative errors still large (17.3 % and 18.9 %).

Also, a peak centred at ∼7.48 keV, close to the tabulated value of the more intense peak, the Ni KL_3 transition (7.478 25 keV), appears in all spectra of the complete sample set.

Since there are no other peaks that can be assigned to Ni in the spectra, but instead a peak at ∼9.20 keV, assigned to Pb or Ga, in all spectra, it can be concluded that the peak at ∼7.48 keV is an escape peak.

Therefore, Ni is not referred in the further discussions.

Co ($Z = 27$)

The element Co was detected in thirty-two samples and all of these show relative errors equal or greater than 20 %.

The only peak present in the spectra that can be assigned to Co corresponds to the Co KL_3 transition tabulated at 6.9303 keV. However, this is very close to the Fe KM_3 transition tabulated at 7.057 98 keV and thus, is likely due to the presence of Fe.

There are two other explanations for the presence of this peak. For one, sometimes the presence of Co is mistaken with the escape peak of the Cu KM_3 transition tabulated at 8.905 29 keV [111], an element present in all spectra of the sample set. On the other hand, by observation of the spectra in the four ranges, it seems that the peaks on the spectra were mistaken with noise.

In conclusion, Co is considered non-existent in all samples of the the sample set.

Fe ($Z = 27$)

The element Fe was detected in all samples of the sample with only seven having relative errors equal or greater than 20 %.

The detection of Fe does not raise doubts, since several peaks can be assigned to it. Thus, Fe is considered in further discussions.

Mn ($Z = 25$)

The element Mn was detected in ninety four samples and of these, seventy-six show a relative error equal or greater than 20 %.

Similar to Mo, the *Main Range* spectra of the complete sample set do not show any peaks that can be assigned to Mn, however, the *Low Range* spectra of all samples of the sample set show a very slight peak at ∼5.9 keV close to the Mn KL_3 transition tabulated at 5.898 75 keV. This peak also exists on the spectrum of sample of the grid that held some of the paintings although it is slightly dislocated to the left, its relative concentration is greater and its relative error is lesser than any sample of the sample set. Figure 4.5c shows the spectra of sample `pxrf-p90-4`, the sample with the largest relative concentration, of sample `pxrf-p25-12`, a sample where the relative concentration Mn was found to be lower than the limit of detection, and of the grid for comparison. Furthermore, this peak in the *Low Range* spectra may be due to a sum peak of the Ag L_3M_5 transition, tabulated at 2.984 31 keV.

Given that it is not clear how Mn was identified, the element Mn is excluded from further discussions.

Cr ($Z = 24$)

The element Cr was detected in three samples and with relative errors ranging from 52.7 to 56.5 %.

Despite the large measurement errors, a slight peak is present throughout the complete sample set. However, the Cr KL_3 transition is sometimes mistaken with the escape peak of the Fe KM_3 transition [111] and in this case it probably was, since there are no other peaks that can be assigned to Cr.

Therefore, Cr is considered non-existent throughout the sample set.

Ti ($Z = 22$)

The element Ti was detected in one hundred and six samples and of these, forty one show a relative error equal or greater than 20 %.

The *Low Range* spectra of the whole sample set present a peak at ∼4.5 keV near the tabulated value of the Ti KL_3 transition, 4.504 86 keV. However, it is possible that this peak is the escape peak of Fe KL_3 [59].

The spectra also show slight protuberances at ∼4.95 keV near the tabulated value of the Ti KM_3 transition, 4.931 81 keV. Still, the presence of the peaks throughout the whole sample set indicates that Ti may be an impurity either on a common layer, or due to systematic errors.

These reasons suggest that Ti is not present in the samples studied, still it is included in an exploratory PCA analysis.

V ($Z = 23$)

The element V was detected in six samples and of these, four show a relative error equal or greater than 20 %.

The transition V KL_3 is tabulated at 4.952 20 keV, very close to the peak referred in the previous section. Thus, it seems that V was wrongfully accounted.

Therefore, V is not considered in further discussions.

Sc ($Z = 21$)

The element Sc was detected in forty-two samples and of these, twenty-seven show a relative error equal or greater than 20 %. Also, the other samples show errors greater than 10 %.

This element seems to have been misidentified due to the proximity of a peak of Ca, given that the Sc KL_3 transition is tabulated at 4.0906 keV and the Ca KM_3 transition is tabulated at 4.0127 keV. Moreover, there are no other peaks that can be assigned to Sc.

In sum, Sc is not considered in further discussions.

Ca ($Z = 20$)

The element Ca was detected in all samples of the sample set with a maximum relative error of 6.8 %.

The detection of Ca does not raise doubts, since it can be confirmed by two peaks.

K ($Z = 19$)

The element K was detected in one hundred and forty-nine samples and of these, twenty-eight show a relative error equal or greater than 20 %.

In the whole sample set, the *Light Range* have a peak at ~3.32 keV which can be assigned to the K KL_3 transition tabulated at 3.3138 keV.

The identification of K in almost all samples of the sample set does not raises doubts, since it is usually associated with Ca and it was also identified in several samples using SEM/EDS. Therefore, K is considered in further discussions.

S ($Z = 16$)

The element S was detected in all samples with relative errors ranging from 0.6 to 1.3 %.

Although there is only one peak that can be assigned to S (at ~2.4 keV) and this overlaps with one other peak of Pb, there is not much doubt that S exists in all samples. The main reasons are that in the range of energies studied, this is the only peak that could have been identified and the peak at ~2.4 keV in the spectra cannot be fitted to a single Gaussian distribution but two instead.

Furthermore, S was detected using SEM/EDS of the selected samples, particularly in their preparatory layers.

In conclusion, S is considered in further discussions.

Ba ($Z = 56$)

The element Ba was detected in one hundred and sixteen samples and of these, eighty five show a relative error equal or greater than 20 %.

Once more it is not clear how the element Ba was identified and quantified throughout the sample set, since no peaks were found in any spectra that can be assigned to Ba. Although the *High Range* is described as having the optimal sensitivity, all spectral ranges were investigated. Figure 4.5d shows the spectra of sample `pxrf-p90-23`, the sample with greatest relative concentration and lesser relative error of the sample set, and of the grid that held some of the paintings, which the spectrum reveals has Ba in its composition.

Therefore, Ba is considered non-existent throughout the whole sample set.

Cs ($Z = 55$)

The element Cs was detected in one hundred and fifty eight samples and of these, only four show a relative error equal or greater than 20 %.

In the case of Cs no relevant peaks were found in any spectral range. Figure 4.5e shows the region where the more intense Cs peaks were expected for sample pxrf-p90-4, the sample of the sample set with the greater relative concentration of Cs. Therefore, Cs is considered non-existent throughout the whole sample set.

Te ($Z = 52$)

The element Te was detected in one hundred and sixty four samples and of these, only nine show a relative error equal or greater than 20 %.

In the case of Te no relevant peaks were found in any spectral range. Figure 4.5e shows the region where the more intense Te peaks were expected for sample pxrf-p90-4, the sample of the sample set with the greater relative concentration of Te and lesser relative error.

Therefore, Te is considered non-existent throughout the whole sample set.

Sb ($Z = 51$)

The element Sb was detected in one hundred and one samples and of these, only thirteen show a relative error equal or greater than 20 %.

Once more, no peaks were found in any spectral range that could have been assigned to Sb. Figure 4.5f shows the region of interest of Sb for samples pxrf-p90-23, the sample with greater relative concentration, and pxrf-p27-21, the sample with lesser relative error. Therefore, Sb is considered non-existent throughout the whole sample set.

Sn ($Z = 50$)

The element Sn was detected in one hundred and sixty four samples and of these, thirty two show a relative error equal or greater than 20 %.

The peak corresponding to Sn KL_3 transition is not an easily fitted one, since it does not has a bell-shaped aspect and it is on a region subjected to a high degree of noise. Therefore, in some instances where the Sn KL_3 peak has low intensities and consequently no secondary peaks exist, noise may have been misinterpreted. Still, the aspect of the sample may serve as a clue in these cases.

Being an important pigment in the colour and aspect of the samples, Sn is considered in further discussions.

Cd ($Z = 48$)

The element Cd was detected in one hundred and thirty three samples and of these, forty three show a relative error equal or greater than 20 %.

There is only one slight peak that can be assigned to Cd, located at ∼23.0 keV close to the tabulated value of Cd KL_3 transition, ∼23.1736 keV. However, this peak can also be assigned to Ag, which is present in all samples due to the anode of the PXRF instrument. Figure 4.5g shows the spectrum of sample `pxrf-p90-23` in the region of interest for Cd, since it is the sample of the sample set with the largest relative concentration of Cd. Moreover, Ag and Cd show a Pearson coefficient of $r = 0.98$ in the samples where both were detected.

Therefore, Cd is considered non-existent throughout the whole sample set.

Ag ($Z = 47$)

The element Ag was detected in one hundred and thirty one samples and of these, forty three show a relative error equal or greater than 20 %.

Given that the anode of the PXRF instrument has Ag in its composition and that the mode *TestAll Geo* does not compensate this contribution, it is not possible to identify nor quantify the element Ag in the samples. Figure 4.5g shows the spectrum of sample `pxrf-p90-23` (the sample with the largest relative concentration) in the region of interest for Ag, where an ill-defined peak can be attributed to it.

Therefore, the PXRF analysis regarding the presence of Ag is no further discussed.

Pd ($Z = 46$)

The element Pd was detected in one hundred and twenty one samples and of these, sixty six show a relative error equal or greater than 20 %.

No peaks that could reasonably have been assigned to Pd were found on any range of any spectra. Figure 4.5g shows the spectrum of sample `pxrf-p90-23` in the region of interest for Pd, since it is the sample of the sample set with the largest relative concentration of Pd. Moreover, Ag and Pd show a Pearson coefficient of $r = 0.98$ in the samples where both were detected, indicating that the identification of Pd may have been incorrect.

Therefore, the PXRF analysis regarding the presence of Pd is no further discussed.

Al ($Z = 13$)

The element Al was detected in all samples of the sample set with only four showing a relative error equal or greater than 20 %.

Given that one peak (corresponding to the Al KL_3 transition) can be assigned to Al and to no other element nor artefact, it seems safe to assume that Al was correctly identified. Moreover, Si, which is usually associated with Al, was also found throughout the sample set.

The SEM/EDS analysis also shown the presence of both Al and Si within the preparatory layers.

Therefore, Al is considered in further discussions.

P ($Z = 15$)

The element P was detected in all samples of the sample set with relative errors ranging from 1.0 to 10.1 %.

The *Light Range* spectra show a broad and intense peak at $\sim$2.15 keV, close to the tabulated value of the P KL_3, 2.0137 keV. However, it can also be assigned to other elements, such as Pb. Thus, given its intensity it seems safe to assume that it is due to Pb and not P.

In conclusion, P is not considered in further discussions.

Si ($Z = 14$)

The element Si was detected in all samples of the sample set with relative errors ranging from 1.2 to 4.0 %.

The case of Si is very similar to Al, reporting a single peak that can be assigned to Si. However, it is a very defined peak that cannot be assigned to other elements.

The SEM/EDS analysis also shown the presence of both Al and Si within the preparatory layers.

Therefore, Si is considered in further discussions.

Cl ($Z = 17$)

The element Cl was detected in all samples of the sample set with relative errors ranging from 1.1 to 3.4 %.

Similarly to P, Cl seems to have been misidentified due a very defined peak assigned to the Pb M_3N_4 transition at ~2.63 keV.

Therefore, Cl is not considered in further discussions.

Mg ($Z = 12$)

The element Mg was detected in thirty samples of the sample set with relative errors ranging from 34.9 to 65.4 %.

No peak that can be assigned to Mg was found in any spectra, meaning that probably noise was classified as Mg. Figure 4.5h shows the spectrum of sample pxrf-p90-25, which reports the largest relative concentration and smaller relative error regarding Mg, and, as it can be observed, no peak can be found at 1.2536 keV (tabulated Mg $KL_{2,3}$ transition) nor at 1.3022 keV (tabulated Mg KM transition).

Therefore, it is considered that Mg is not present in this sample set.

Calculation of relative intensities (semi-quantitative process)

The data is acquired in four spectral ranges, *Light Range*, *Low Range*, *High Range* and *Main Range*. The four spectral ranges were examined from a qualitative point of view, since each spectral range has optimal sensitivity for a defined range of elements [2]. However, only the *Light Range*, from 0 keV to 5 keV, and the *Main Range*, from 5 keV to 30 keV, are presented throughout this dissertation, since the main peaks related to all elements studied here can be found within these two ranges, providing a general overview of each spectrum.

---

[2] These ranges are mentioned on Section 3.1.4.

In the following, a semi-quantitative analysis is implemented. In it, the net peak areas of the relevant peaks are normalized using the Ag KL_3 peak for elements found on the *Main Range* and Ag L_3M_5 peak for elements found on the *Light Range*, and after relative intensities or rates, R, are calculated. This calculation corresponds to the first steps of the Fundamental Parameters Method and is described in [116]. Samples containing Au were discarded from this analysis, given that Ag is a major constituent of gold alloys. Moreover, in regard to gold alloys, the PXRF analysis is merely exploratory and, given their importance, micro-samples were extracted and analysed with SEM/EDS.

The first step of this approach is the identification of the maximum number of relevant peaks, since neither a qualitative analysis nor a quantitative can be achieved without it. Given that the data provided by the equipment is somewhat noisy, it is important to apply a smoothing filter to reduce the amount of "false" peaks.

As an example, Figure 4.6 shows the peaks found for the acquired spectrum with (a) no filter, (b) a median filter and (c) a Savitzky-Golay filter. This spectrum is from sample `pxrf-p27-48`, a sample containing Au and Hg, whose most intense peaks are located at 9.7133 keV and 9.9888 keV [126], respectively. A list of possible peaks is returned by `PeakUtils` library and for the filters, a window of length of twenty-five was used and on the Savitzky-Golay filter a polynomial order of ten. In this figure, it can be observed, that with the original data an excessive number of peaks was suggested (thirty-six), with the application of the median filter only eleven peaks were suggested and with the application of the Savitzky-Golay filter twenty-one peaks were suggested. Moreover, when comparing the filtered spectra with the unfiltered one, it can be concluded that the median filter eliminated several relevant peaks (e.g. at ∼2.14 keV) and altered the shape of several peaks to trapezoids while the Savitzky-Golay did not eliminate nor significantly changed any. Still, the latter failed to detect a few small peaks, including at ∼4.00 keV and at ∼15.16 keV.

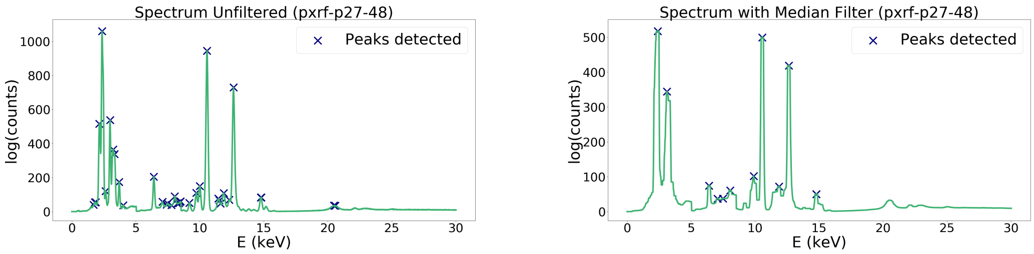

(a) Unfiltered.

(b) With median filter.

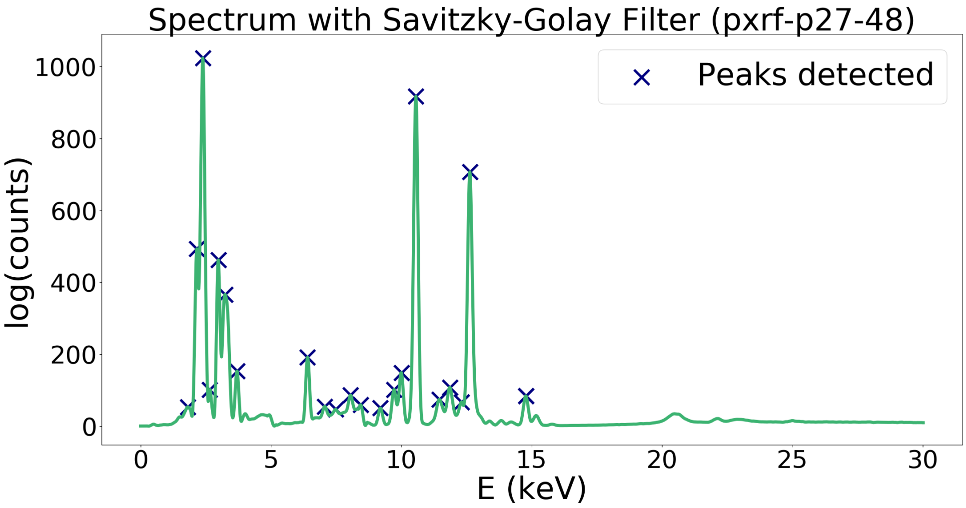

(c) With Savitzky-Golay filter.

Figure 4.6: Example of spectra unfiltered, with a median filter and a Savitzky-Golay filter, for comparison. When unfiltered an excessive number of peaks were detected (thirty-six), while using a median filter the shape of the peaks changes and only eleven peaks were detected, and when the Savitzky-Golay filter was employed, twenty-one peaks were correctly detected.

Given that the routine from `PeakUtils` failed to detect all peaks, a new routine was implemented. This new routine, explained below, not only allows for peak detection but also identifies said peaks, provides peak fitting and calculates net peak areas. For the creation of this new routine, some assumptions were made:

1. All peaks can be adjusted to Gaussian distributions;
2. An estimate of the possible position of the target peak is known as well as of its neighbours peaks;
3. The width of each peak does not vary greatly within samples; and
4. Baseline corrections were performed making the offset of each peak null.

For this routine, a list of peaks has to be created containing the abscissas of two points that will definitely belong to each side of the peak, if it exists, allowing the detection of peaks. This can be troublesome depending on the sample set studied. Thus, if the spectra differ greatly from each other or if too many relevant peaks overlap, the creation of this list can be exhaustive. Fortunately, in this case study it can be applied given that for starters, the spectra collected do not differ greatly, since several elements belong to the preparatory layers and therefore appear in virtually all samples. Also, Bernardo Manuel's palette is similar in the four works of art investigated. In each entry of this list it should also be specified what is the least convoluted side (*left* or *right*, whereas *left* is the default), since in several cases both sides of the peak show some degree of convolution. This side will be used to calculate the fitting parameters and symmetry will be assumed.

This list can be created using object-oriented programming, where each peak corresponds to an instance of an object and each attribute denotes a specific information related to the peak, and thus a possible entry is

```
au_l3m5 = Peak(x1=9.645, x2=9.800, side="left")
```

The first step, corresponds to the detection of the peaks. To do so, the monotony between the values $x1$ and $x2$ is checked, and if it goes from ascending to descending, then a peak may exist. Moreover, the side specified on the entry is investigated, and the point where the spectra changes once again its monotony is considered a reference point. Thus, the difference between the highest point and the reference point is calculated, and if inferior to an user-defined threshold (the default is zero), it will not be considered a peak, allowing to differentiate peaks from noise.

Once the peak has been detected, the coordinates of the highest point become known. The x-coordinate corresponds to an estimate of the centre of the peak and the y-coordinate to an estimate of its amplitude, since the offset is null due to the baseline corrections. The only fitting parameter that is still unknown is the standard deviation, σ. The standard deviation is calculated using the two points known, the highest point of the peak and the reference point. The difference of the y-coordinates of both points is calculated, and using Equation (4.1) the convoluted fraction of that side is known, and the double of the difference of the x-coordinates of both peaks provides the full width at *fraction* of maximum ($FWFM$) of the Gaussian distribution. Using Equation (4.2), an initial estimate of σ is computed.

$$f = 1 - \frac{(y_{\text{peak}} - y_{\text{ref}})}{y_{\text{peak}}} \tag{4.1}$$

$$\sigma = \frac{FWFM}{\sqrt{2ln\frac{1}{f}}} \tag{4.2}$$

Figure 4.7 demonstrates how a peak is found and how the estimates of the parameters, namely σ, are calculated. As such, the peak is found if between x_1 and x_2 the monotony changes, which in this case occurs. Furthermore, the central peak at (x_{peak}, y_{peak}) is convoluted both on left and right side, however, it is less convoluted on the left side and, thus this is the side that will provide a reference, at coordinates (x_{ref}, y_{ref}). The ratio of $\frac{y_{\text{peak}} - y_{\text{ref}}}{y_{\text{peak}}}$ corresponds to the deconvoluted height fraction of the peak, meaning that f correspond to the convoluted height fraction of the peak. As for the value $FWFM$, it corresponds to the difference $x_{\text{peak}} - x_{\text{ref}}$ multiplied by two, since it is assumed that the peaks can be fitted to Gaussian distributions.

Next, the estimated parameters are used to create a true Gaussian distribution by performing a reflection of the investigated side along the centre of the peak.

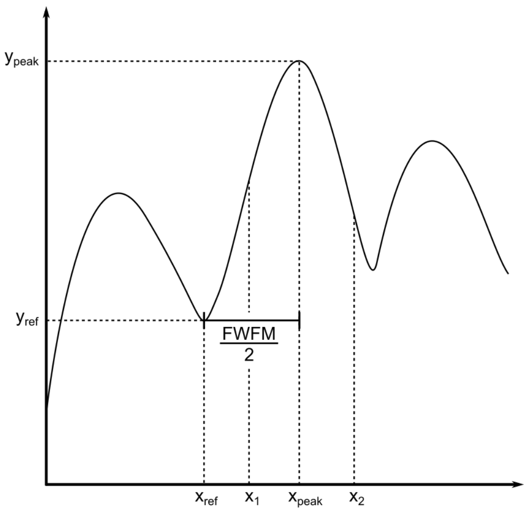

Figure 4.7: Example on how to find a peak and its parameters.

To this new distribution, the routine `curve_fit` from the `scikit-learn` library is implemented for better parameters estimates and therefore more accurate fits.

The net peak area is calculated by integrating each peak using the function `integrate.quad` from `SciPy`. The uncertainties were calculated using the covariance matrix of the fitting and then propagated through the integral using the package `uncertainties`.

To simplify the filling of the list of peaks, the `PeakUtils` peak detection routine can be used to obtain estimates for most peaks. For this purpose, a complex spectrum, i.e., a spectrum with a high amount of close peaks, is preferred. Once again, sample `pxrf-p27-48` is a good example, particularly because it has in its element matrix both Au and Hg, whose peaks can be difficult to detect and to adjust due to their proximity.

The concentrations of each element detected cannot be calculated, since the calibration factors and corrections related with matrix effects were unknown. Therefore, the net peak areas of the relevant peaks were normalized using the Ag KL_3 peak for elements found on the *Main Range* and the Ag L_3M_5 peak for elements found on the *Light Range* and the relative intensities are calculated after. The relative intensities correspond to a rate, R, between the measured intensity of a element (net peak area) and its intensity in a pure sample [116]. It should be noted that this strategy provides less information than the approach followed by the internal software of the PXRF, however, given the expressed reasons, it seems a valid approach. Therefore, if another approach is possible or if the results given by the PXRF seem reliable, then the researcher should not follow this strategy, since it provides incomplete results [3].

Relative intensities, or rates (R), were only calculated for the elements S, Ca, Fe, Cu, Au, Hg and Pb, since these are major elements of each sample and mainly responsible for their aspect, whereas the other elements are only referred on a qualitative basis. Thus, the relative intensities for each of the enumerated elements were calculated according to [116], by using the main peaks of each element, with the exception of S. In the case of S, the $\mathrm{S\,KM_3}$ peak was used, since the $\mathrm{S\,KL_3}$ overlaps completely with the more intense $\mathrm{Pb\,M_5N_7}$ peak. The coefficients needed for the calculations were extracted from several sources and theoretical values were preferred [70, 29, 72, 106]. The calculated values can be observe on Table A.1 [4].

4.2.2 SEM/EDS Data Analysis

As explained in Section 3.2, two types of information can be obtained when employing SEM/EDS, morphological and compositional. For the morphological data, no rigorous treatment is applied since it corresponds to a mapping of the elements selected and thus simple observation suffice. The elemental compositional data, corresponds to spectra very similar to PXRF since in both energy dispersive X-rays are employed.

Even though the spectra acquired with SEM/EDS can easily be treated in the same manner as the PXRF spectra were, this was not the only approach followed. In the laboratory TAIL-UC, the equipment TESCAN Vega3 SBH SEM is associated with the *Quantax* software from *Bruker*. This software provides an interface for analysis both simple and practical. In it, the user, after a spectrum was acquired, selects the relevant peaks, leaving the identification and quantification of said peaks to the software. All steps of the process are supervised, including the

---

[3] This strategy corresponds to the first steps of the Fundamental Parameters Method.

[4] In Table A.1, the uncertainties are expressed on their concise form. For example, 5.01(2) should be read as 5.01 ± 0.02 while 5.01(200) should be read as 5.01 ± 2.00.

removal of the background and the deconvolution of peaks. As for the quantification method, it uses P/B-ZAF Spectrum Analysis Background [21], where the ratios of peak intensities to the background (*bremsstrahlung*) are used instead of absolute peak intensities. This means that absorption and enhancement effects, measurement errors, and detector artefacts more or less cancel each other, since the characteristic X-rays and *bremsstrahlung* radiation are of the same physical nature. Moreover, it is a true standardless method, since it is completely independent from scaling factors like beam current, acquisition time and solid angle of the detector.

4.2.3 µRS Data Analysis

All collected samples, except the ones containing gilded layers, were examined through µRS in several different points in order to have a better representation of the sample.

In the majority of the cases, the samples suffered some level of degradation. This happened due to the nature of the samples, which are composed of a preparatory layer, the chromatic layer and a much thicker layer of coating (varnish or another media) than the latter. Thus, when the laser was set at a low power, it did not report any peaks and was overcome with fluorescence; and at higher powers, it degraded the sample, leaving sometimes only the preparatory layer. Also, given that the peaks from the µRS spectra are not very prominent, they can easily be interpreted as noise.

As a result, the application of a filter eliminates some peaks and an automatic peak detection routine, even a supervised one, fails to detect all peaks and/or detects noise as peaks, the latter when a low threshold is defined. Therefore, the detection of peaks in the µRS spectra was performed by observation of each spectrum individually.

Since examination of µRS spectra is not as straightforward as the examination of ED-XRF spectra, particularly in this data set, where several samples suffered degradation or presented very subtly bands due to fluorescence phenomena, the spectra were first compared with each other in order to find similarities and samples with well defined peaks were studied first.

Chapter 5

Results and Discussion

In the following chapter, the results obtained are discussed. The values in Table A.1 [1] are referred along the following sections as *rates* (R), and are interpreted as semi-quantitative results, while the results given by the PXRF instrument are referred as *relative concentrations*, and can be either quantitative or semi-quantitative depending on their quality, namely their relative measurement error.

5.1 Multivariate Analysis

Given the high number of samples obtained via PXRF and variables (elements detected), PCA, a multivariate analysis and dimension reduction technique, was employed. This technique allows the clustering of similar observations, correlation between dependent variables and correlation between variables and observations. Since the goal of PCA is to reduce the number of variables in a system, one recommendation is that the researcher eliminates unnecessary variables or variables that represent the same factor. However, this process should be addressed cautiously, and it is sometimes better to decide which variables should be kept after an exploratory PCA analysis. Moreover, in this project, there are elements whose identification is not easily verified.

---

[1] In Table A.1, the uncertainties are expressed on their concise form. For example, 5.01(2) should be read as 5.01 ± 0.02 while 5.01(200) should be read as 5.01 ± 2.00.

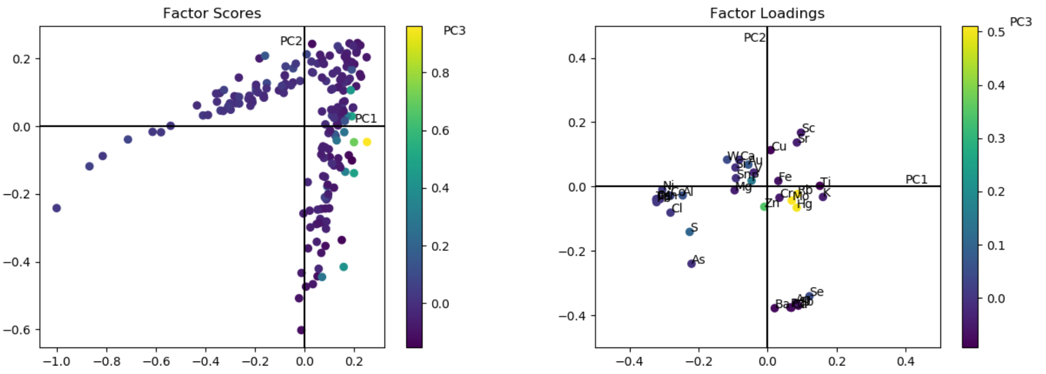

(a) Factor scores.

(b) Factor loadings.

Figure 5.1: PCA results (first three components) using relative concentrations of all samples and elements. The $x-axis$ represents the first component, the $y-axis$ the second and the colour gradient the third.

First a PCA analysis [1] was performed using all the relative concentrations given by the PXRF instrument. No identified elements were excluded, since even wrongfully accounted elements may be associated with others. One such example, is the case of Ag and Cd, where Ag is present due to the anode of the instrument [2] and Cd seems to have been incorrectly identified due to the presence of the former. Therefore, Figure 5.1 shows the factor scores (on the left) and the factor loadings (on the right) using the three first principal components. However, note that this is a simplified approach given that the first nine components have eigenvalues greater than one.

Figure 5.1a shows three sets of similar samples, where the first, on the second and third quadrants of the first two principal components, corresponds in Figure 5.1b to Pb, S and Al, among others, the second, mainly on the fourth quadrant, corresponds to the elements Ag, Cd, Pd and Ba, and the third set, expressed in the colour gradient, is associated with Au, Hg, Mo and Rb. Therefore, the first set does provide a bit of information concerning the composition the samples, the second set does not provide any useful information, since it exists due to the presence of the anode, and the third does in fact highlight the samples

---

[2] This contribution could be compensated if a different mode, such as *Precious metals*, had been used.

containing Au and Hg, however, it also takes into account samples where these elements were wrongfully accounted.

Given the discussion on Section 4.2.1 and the results obtained using relative concentrations, a new PCA analysis was performed, where only the elements Al, Si, S, K, Ca, Ti, Fe, Cu, Au, Sr, Hg, Pb and Sn were chosen and the factor loadings were calculated using rates [3]. Considering Figure 5.2, it can be speculated that the variables Ti and Fe represent the same factor, and that the same occurs for the elements S, Si and Al, as well as Hg and Sr. Taking into account the discussion in Section 4.2.1, it strongly seems that Ti was wrongfully identified due to the presence of Fe and that Sr was identified due to the presence of Hg. As for the elements S, Si and Al, S is associated with a great variety of pigments whereas the simultaneous existence of Si and Al is very common, both as impurities and as a pigment (green earth), thereby they both seem to represent the same factor. Therefore, only Si will be used since its first three factor loadings are larger than the ones of Al. In sum, for the final PCA analysis, only the elements Si, S, K, Ca, Fe, Cu, Hg, Pb and Sn were considered.

PCA was implemented according to [1] using both the data calculated by the PXRF device and rates calculated according to [116]. Note that, the rates calculated lack calibration factors and matrix effects corrections, and therefore in some instances the dependency, and thus correlation expressed on the PCA results may be incorrect. In the first case, three components accounted for 57 % of the variance of the whole data set while in the second, three components accounted 58 % of the variance. Figure 5.3 shows the factor scores and factor loadings obtained using the relative concentrations given by the PXRF device while Figure 5.4 represents the factor scores and factor loadings using the rates calculated according to [116] and normalised using Ag peaks. These figures are coloured 2D plots, since the observation of 3D plots can be quite difficult in printed form. Thus, the distribution along the third principal component can not be divided in quadrants, however, this component seems to be mainly associated with the elements Fe, Cu, Au and Hg in the first case, and Cu and Hg in the second.

As for the dispersion of the factor scores, in Figure 5.3 the majority of samples

---

[3] Au was kept, given that it is an important element regarding pigments (gold alloys) and other element(s) may be associated with it.

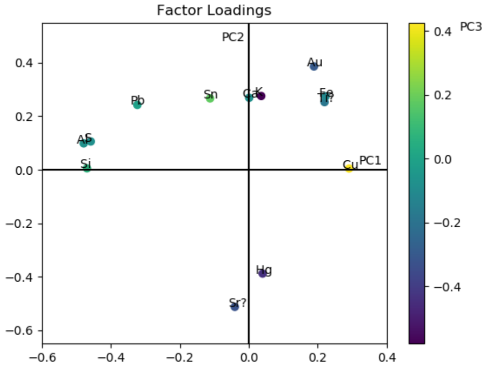

Figure 5.2: Factor loadings of an exploratory PCA analysis, in order to decide which elements should be used in a posterior analysis. The $x - axis$ represents the first component, the $y - axis$ the second and the colour gradient the third. From this figure and the discussion in Section 4.2.1, it can be concluded that Fe and Ti represent the same factor, which can also be said for Hg and Sr, as well as Al and Si.

seem to be characterised by their content of Cu and Hg while in Figure 5.4 the majority are similar in their content of Pb and S. The dispersion of factor loadings is similar in both cases, although in Figure 5.3 the proximity of Pb, S and Sn may hinder the distinction between samples containing lead tin yellow, Pb_2SnO_4, and lead sulphates, such as $PbSO_4$, and in Figure 5.4 the proximity of Fe and Ca may hinder the distinction between lighter and darker brown samples.

Even though in Figure 5.3 and in Figure 5.4 the samples are well distributed by each quadrant, the clustering of such a high number of samples can be difficult to perform simply by observation. Therefore, a Affinity Propagation Clustering method from the `sklearn` library using the first four principal components (these present eigenvalues larges than one), was applied to the PCA factor scores of both cases. In the first case, using the scores in Figure 5.3, twenty clusters were formed while in the second case only fifteen were. These clusters are mentioned in the following sections when relevant and can also be found on Table A.3 and Table A.2. In the case of Table A.3, several clusters can be associated to specific colours, and therefore pigments.

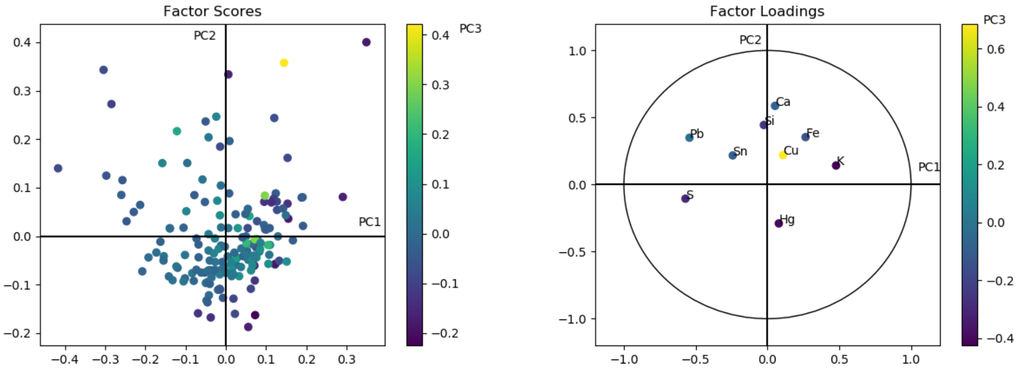

(a) Factor scores.

(b) Factor loadings.

Figure 5.3: PCA results (first three components) using the quantitative data given by the PXRF instrument.The $x-axis$ represents the first component, the $y-axis$ the second and the colour gradient the third.

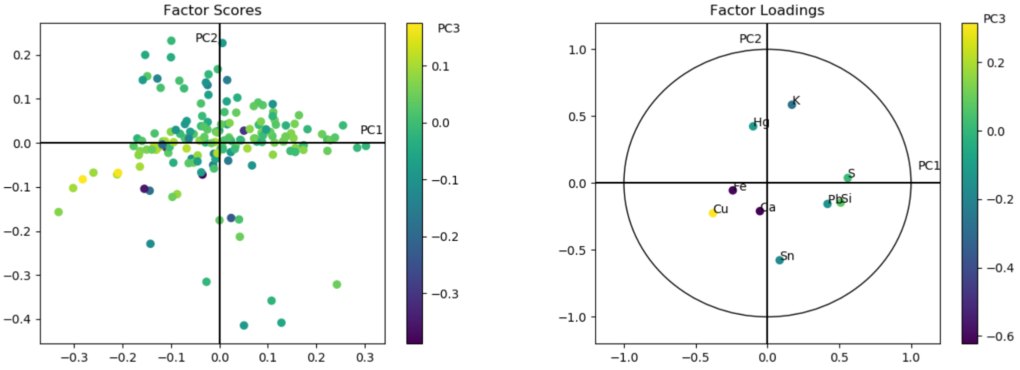

(a) Factor scores.

(b) Factor loadings.

Figure 5.4: PCA results (first three components) using the rates calculated. The $x - axis$ represents the first component, the $y - axis$ the second and the colour gradient the third.

5.2 Preparatory and surface layers

In general, all samples acquired by PXRF contained the elements Al, Si, S, Ca, Fe, Cu and Pb, although the intensities of the peaks associated to each element varied. The consistence of these elements in the whole sample set suggests that they are associated with the preparatory layer. The preparatory layer is formed by the ground layer, which is in turn a succession of layers, and the priming layer (also known as *imprimatura*), which seems to only be present in this polyptych in the painting *Trinity (Eternal Father) (P90)*. Thus, although all these elements may exist in the preparatory layer, or more specifically on the ground layer, based on the SEM/EDS analysis, they do not seem to belong to the same sub-layer.

Figure 5.5 shows an image and spectra obtained via SEM/EDS analysis regarding several layers of sample P26-3. In the spectrum at the left bottom, only a few elements were found, among them, Al and Pb, meaning that perhaps an impurity was analysed; in the right top, the elements S and Ca, associated to *gesso*, and Si, probably an impurity, were found; in the right bottom, the spectrum of a gold alloy is shown; and, in the left top, the spectrum of the layer underneath the gold alloy, known as *bolus* is shown, containing Mg, Al and Si, and thus suggesting the use of green earth (*terre-verte*). In its turn, Figure 5.6 shows an image and spectra obtained via SEM/EDS analysis and an OM photomicrograph of sample P27-5 for better comprehension. On the spectrum on the top, peaks of Ca and S exist, associated to *gesso*, whereas Mg, Si and Fe seem to be impurities. On the spectrum on the bottom, Pb and Ca appear to be the major elements while the others seem to be impurities.

As for the analysis of the collected µRS spectra, particularly those where the sample was most degraded, it conclusively pointed to the presence of *gesso* within the preparatory layer, except in the layer of *Lamentation of Christ (P26)*. The most intense band is located at $\sim 1009\,\mathrm{cm^{-1}}$, which can be assigned to gypsum, $\mathrm{Ca(SO_4)\cdot 2\,H_2O}$, however, they lack the bands associated with $\mathrm{H_2O}$ ($\sim 3395\,\mathrm{cm^{-1}}$) [23]. Gypsum (fine *gesso*) is associated with the mineral anhydrite (coarse *gesso*), $\mathrm{Ca(SO_4)}$, its dehydrated form. These compounds were usually applied mixed or in layers with gypsum on top, since gypsum is less porous and therefore easier to paint. Moreover, given their chemical nature, transformations from anhydrite to

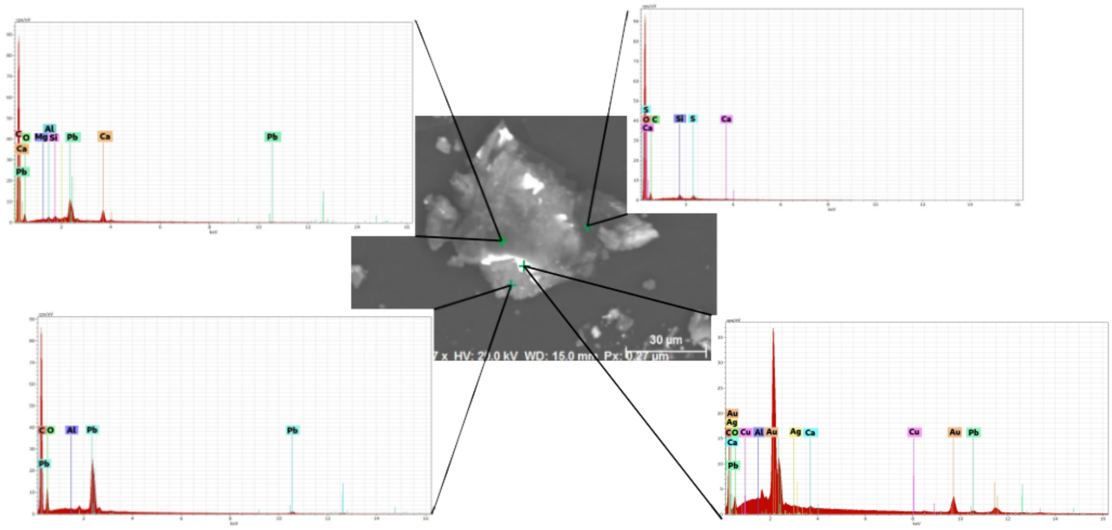

Figure 5.5: Image and spectra of sample P26-3 obtained by SEM/EDS, showing layers of *gesso* and *bolus*.

gypsum and vice-versa due to temperature and/or humidity, among other factors, may occur. As such, the distinction between the two is not a goal in this project and can be concluded that *gesso* exists within the preparatory layers of *Annunciation (P25)*, *Apparition of Christ to the Virgin (P27)* and *Trinity (Eternal Father) (P90)*.

In the samples extracted from *Lamentation of Christ (P26)*, no distinct bands were found, however, the percentage of S presented on the PXRF spectra of *Lamentation of Christ (P26)* is similar to the others, which could mean that the µRS laser did not reach the preparatory layer. Also, given that all the PXRF spectra show a high percentage of S, it can be assumed that the preparatory layer is thicker than the chromatic and surface layers combined.

Figure 5.7 shows the µRS spectra of preparatory layers of the four paintings and the spectra of gypsum [99] and anhydrite [98] for reference. It also shows microscopic images of samples P90-5 and P26-2, where the latter suffered degradation due to the µRS laser, leaving an inner layer exposed.

Moreover, µRS analysis of this sample set did not indicated the presence of quartz which was identified in the preparatory layers of *Lamentation of Christ (P26)* and *Apparition of Christ to the Virgin (P27)* in a previous study [6], where

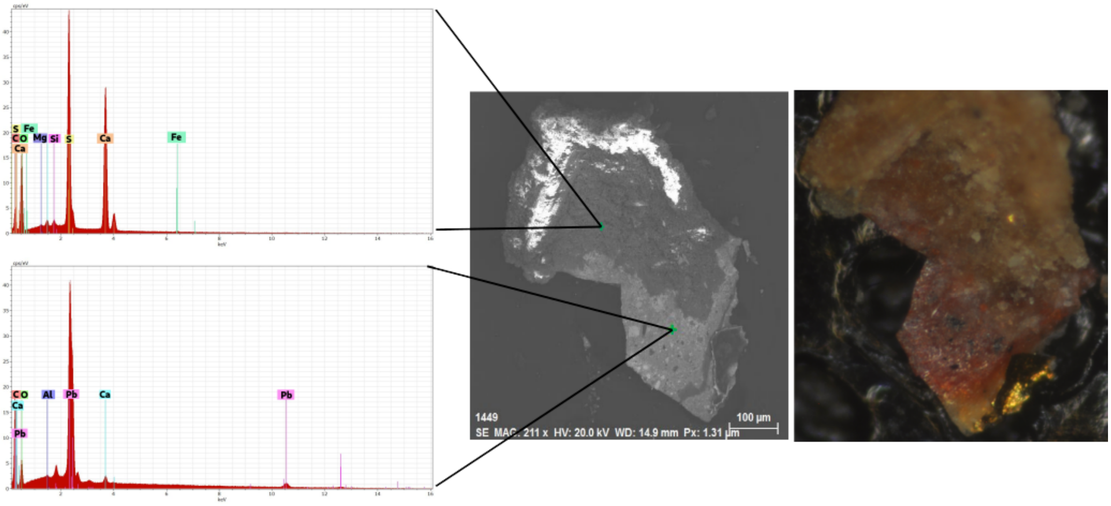

Figure 5.6: Image and spectra of sample P27-5 obtained by SEM/EDS, and OM photomicrograph, showing *gesso* and several impurities.

it is not clear if quartz were found in well defined layers or if its presence is only due to isolated grains.

Concerning the priming layer, with exception of *Trinity (Eternal Father) (P90)*, it seems that the chromatic layer was applied directly on *gesso*, and that no priming layer is present. This was first hypothesised while observing the paintings, particularly in flawed regions. As for *Trinity (Eternal Father) (P90)*, a green layer is visible in some flaws of the background, but not of painted characters. Further investigation using µRS, suggests the use of green earth through a band at ~556 cm^{-1} in sample P90-6. This band is also present in another sample of green colour, and thus its association is extensively discussed on Section 5.4.4.

One other component present throughout the four works of art is the coating, which, based on the µRS analysis, seems to differ between paintings. Figure 5.8 shows the µRS spectra of coating samples from each painting, except from *Trinity (Eternal Father) (P90)*, from which no suitable samples were identified. The µRS spectra of samples P25-3-2 and P26-2-1, from *Annunciation (P25)* and *Apparition of Christ to the Virgin (P27)* respectively, show the amide I band at ~1665 cm^{-1}, the CH_2 scissoring at ~1450 cm^{-1}, a sharp aromatic ring breathing band at ~1002 cm^{-1} and also C–H bands from 3100 cm^{-1} to 2700 cm^{-1}, implying

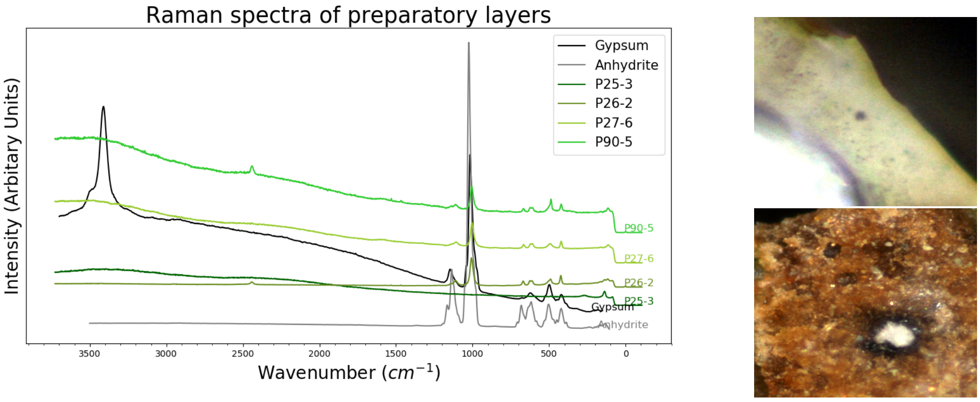

Figure 5.7: Raman spectra of samples P25-3, P26-2, P27-6 and P90-5 (on the left), which present bands associated with *gesso*, photomicrographs of samples P26-2 (on the top) and P90-5 (on the bottom). The spectra of samples P25-3, P27-6 and P90-5 show bands associated with gypsum (in black) [99] and anhydrite (in grey) [98] while the spectrum of sample P26-2 does not show them.

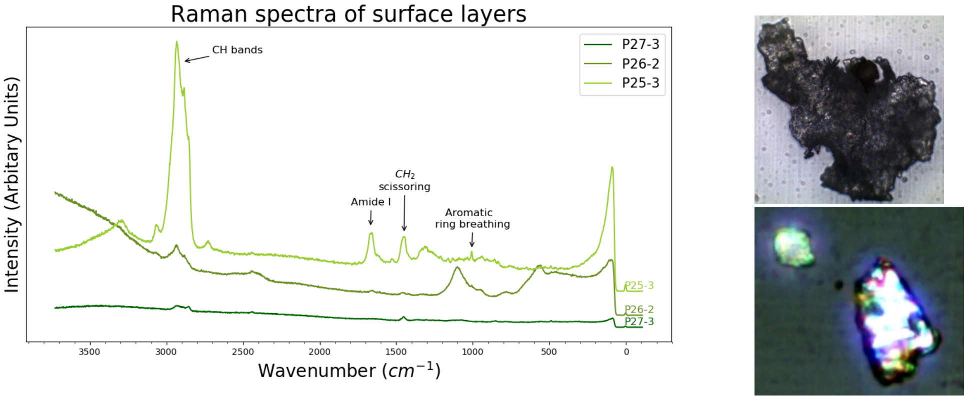

Figure 5.8: Raman spectra of samples P25-3, P26-2 and P27-3 (on the left), which present bands associated with coatings, photomicrographs of samples P25-3 (on the top) and P27-3 (on the bottom). The spectra of samples P25-3 and P26-2 indicate a proteinaceous media while the spectrum of sample P27-3 suggests a polysacharideous media.

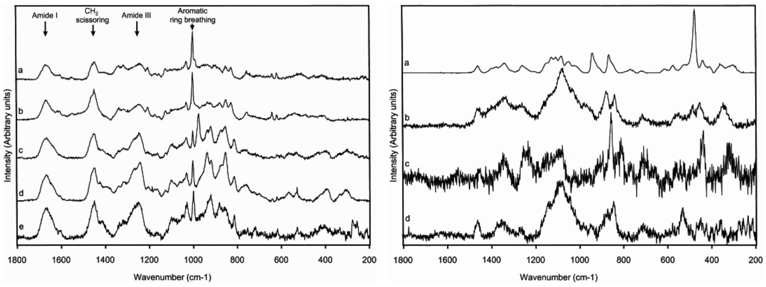

Figure 5.9: Proteinaceous media (on the left) and polysaccharideous media (on the right) for reference. On the left, (a) albumin, (b) casein, (c) gelatin, (d) isinglass and (e) fish glue are shown while on the right, (a) starch, (b) gum arabic, (c) tragacanth, (d) cherry gum. Taken from [122].

Table 5.1: Main results concerning the preparatory and surface layers.

Material	Painting	PXRF	SEM/EDS	µRS
Gesso	P25, P26, P27, P90	Ca, S	Ca, S	Intense band at ~1009 $\mathrm{cm^{-1}}$
Proteinaceous media	P25, P26	n/a	n/a	Amide I at ~1665 $\mathrm{cm^{-1}}$, CH_2 at ~1450 $\mathrm{cm^{-1}}$, sharp band at ~1002 $\mathrm{cm^{-1}}$, C−H at 3100−2700 $\mathrm{cm^{-1}}$
Polysaccharideous media	P27	n/a	n/a	CH_2 at ~1450 $\mathrm{cm^{-1}}$, C−H at 3100−2700 $\mathrm{cm^{-1}}$

that a proteinaceous media was employed [122], which can be seen for comparison on Figure 5.9. Sample P27-3-7 does not have the amide I band, a sharp aromatic ring breathing band at ~1002 $\mathrm{cm^{-1}}$ nor any bands in the 1800 $\mathrm{cm^{-1}}$–1500 $\mathrm{cm^{-1}}$ region, indicating the presence of a polysaccharideous media. Moreover, in general, this spectrum resembles the characteristic spectra of polysaccharideous media [122], which can be observed at Figure 5.9.

Table 5.1 shows a summary of the results obtained concerning the preparatory and surface layers.

5.3 Background layer

In this section, the backgrounds of each painting are investigated. Here, the term *background* is applied to refer to large areas of apparently the same aspect belonging to the scenery. The term *background* does not comprise features of the characters nor of the floors, which present several details [4].

Furthermore, the background is a feature virtually constant throughout the paintings, particularly in *Annunciation (P25)* and *Trinity (Eternal Father) (P90)*, and its analysis is somewhat useful for effects of comparison between samples, since it is admissible that some details have been painted over the background.

5.3.1 *Annunciation (P25)*

The background of *Annunciation (P25)* is well represented with a total of seven samples using PXRF and one extracted sample. The extracted sample, , was analysed using µRS, but, unfortunately, did not yield conclusive results. In general, the PXRF spectra of this background are very similar, including of samples pxrf-p25-9, pxrf-p25-2 and pxrf-p25-8. The PXRF spectra of these three samples and two more (pxrf-p25-1 and pxrf-p25-7) can be observed in Figure 5.10.

Sample pxrf-p25-9 has a blueish aspect, which, given the similarity of its spectrum with the spectra of the other samples, is most likely due to organic components undetected via PXRF. Moreover, this region has a very different aspect when compared with the whole painting and was painted slightly overlapping the tallest flower of the vase [5], indicating that this layer may have been applied during an intervention or an unsuccessful cleaning action. As for sample pxrf-p25-2, it is darker than samples pxrf-p25-1, pxrf-p25-7 and pxrf-p25-8. This darker tone does not seem to be due to the presence of Cu, meaning that a carbon-based pigment was probably applied. The source of this pigment is not clear, however, sample pxrf-p25-2 reports the highest rates of Ca and S among the four samples, elements associated with carbon-based black pigments of animal source. These results are also consistent with the relative concentrations given by the PXRF instrument.

---

[4] The term *background* here applied has a similar meaning to the theatrical term *backdrop*.

[5] The poor quality of Figure 1.1 does not allow the observation of these details.

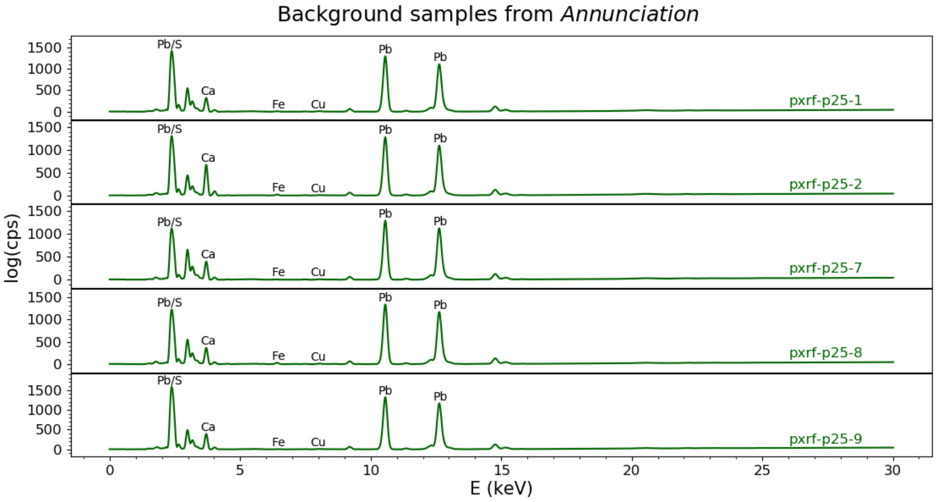

Figure 5.10: Background samples from *Annunciation (P25)*. The spectrum of sample pxrf-p25-9 does not differ greatly from the others, even though it has a blueish aspect. This probably means that the blue colour derives from organic materials.

5.3.2 *Lamentation of Christ (P26)*

Of the four paintings, the background of *Lamentation of Christ (P26)* is the most complex and detailed, having a brown sky covered by green trees and dark ruins along with small white details. In the middle of the painting, which is incidentally the middle of the ruins, there is a portico showing a lighter sky and vegetation. Lastly, in the second plane of this painting, the ground is also as brown as the skies.

Seven samples using PXRF were obtained of the background of *Lamentation of Christ (P26)*, providing an overview of it. The dark brown tones of samples pxrf-p26-32 and pxrf-p26-32a were likely achieved using a copper-based pigment, given the high rates of Cu. The vegetation on the portico, sample pxrf-p26-25, has high rates of Pb and S for a green sample and is, therefore, brighter, and the sky on the portico has Hg, associated with vermilion, a red pigment. The white details, the moon (pxrf-p26-23) and the bird (pxrf-p26-24) have high rates of Pb and S. Since high rates of Pb and S are present in lighter regions, suggests that lead sulphate was employed. The subject of white areas is further discussed in

Section 5.4.1

5.3.3 *Apparition of Christ to the Virgin (P27)*

The background of *Apparition of Christ to the Virgin (P27)* is mainly composed of a framed outside view of the primary scene. Details as the man (speculated to be Saint John) kneeling are not here considered as background.

Of this region, seven samples were acquired using PXRF and one was extracted. The extracted sample was analysed with µRS, however, it did not yield conclusive results. The lack of evidence, given that the samples did not suffer degradation and that the µRS spectra is not overcome with fluorescence, may imply that a red ochre was used, a pigment with tabulated slight bands while using a 532 nm laser [37, 24]. Moreover, the PXRF results indicate the presence of Fe.

The darker tone, used on the left corner of the painting (pxrf-p27-1), has the highest rate of Cu of the background. The landscape is much lighter than the edge and frame of the window, and the increasing presence of Pb suggests once again that a lead pigment was used. Also the presence of Hg in the reddish sky (pxrf-p27-2) suggests the use of vermilion.

5.3.4 *Trinity (Eternal Father) (P90)*

Trinity (Eternal Father) (P90), the centrepiece of this polyptych, is very different from the other paintings, in the sense that the gloomy dark tones have been abandoned over a bright yellow one. Likewise, on the corners a black paint was applied forming a fleur de lis frame, which may have been painted to replace a real frame.

From *Trinity (Eternal Father) (P90)*, only two samples, pxrf-p90-1 and pxrf-p90-29, were studied from the yellow background using PXRF due to its consistency and four from the frame, from pxrf-p90-25 to pxrf-p90-28, since it contained several layers and small yellow stars drawn over it. These spectra are shown on Figure 5.11, where the highest rates of Ca and Cu correspond to darker regions. Moreover, three samples were extracted, one of the yellow background, one of the frame region and one other of a lower layer visible due to a flaw.

From the PXRF analysis, the yellow background is composed of the general elements referred on Section 5.2, however, it should be noted that this painting

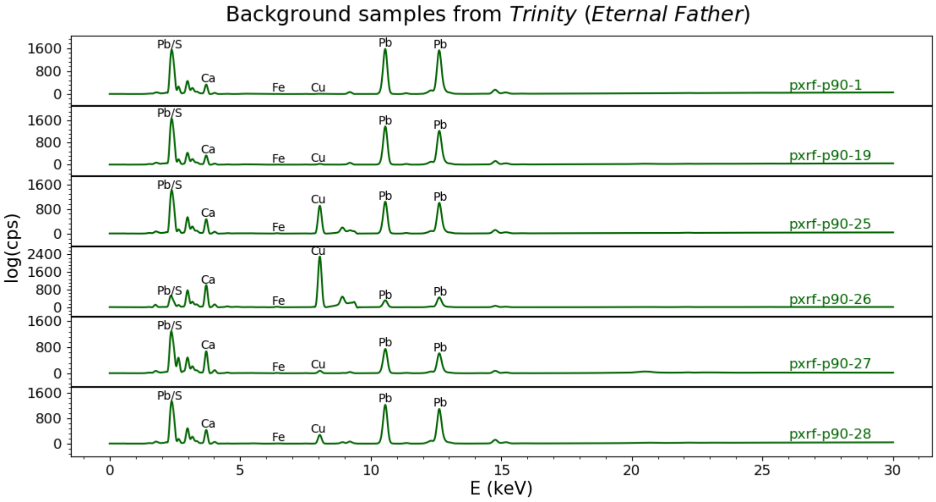

Figure 5.11: PXRF spectra of background samples from *Trinity (Eternal Father) (P90)*. The elements Pb, associated with white, Ca and Cu, both associated with darker tones, are the ones that vary greatly.

has the highest rates of Pb in general, which is normally related with the largest amounts of lead white. However, the µRS analysis of sample P90-7, which pertains several layers, showed a peak, not a doublet, at ∼1050 cm^{-1}. A doublet in this region is an evidence of lead white, but a single peak is associated with non-basic lead carbonate, $PbCO_3$. The use of a non-basic lead carbonate as a pigment here should not be discarded but it may also be an issue related with the resolution of the experimental setup (∼4 cm^{-1}), that failed to detect a doublet. This subject is further discussed in Section 5.4.1, since more than one spectrum shows this band.

As for the frame, it has a much higher content of Cu, particularly in the dark layer directly below the painted stars.

5.4 Chromatic layer

The following sections pertain the pigments analysis and conclusions reached, one of the focus of this project. Each section corresponds to a colour and results from all the techniques employed are referred. Table 5.2 shows a summary of the results obtained.

5.4.1 White Areas

White pigments are very difficult to identify using PXRF, particularly in this polyptych where Ca, S and Pb belong to the preparatory layer. In the preparatory layer, *gesso* and the element Pb were found, the latter as an impurity within these layers.

Fortunately, the PCA provided new insights regarding this issue. All white samples, with the exception of pxrf-p25-12 seem to have a similar content of S and Pb, as observed on Figure 5.4. Moreover, Clusters 5 and 15 from Table A.3 comprise all white samples and all non-reddish carnations, with the exception of samples pxrf-p25-12 and pxrf-p27-17. Sample pxrf-p25-12 scored less in the second principal component, which can be associated with the presence of Ca given its white colour whereas sample pxrf-p27-17 scores more, which is still associated with S. The association of white samples in two clusters and in the first and fourth quadrants of Figure 5.4, suggests that a white lead sulphate (Flemish white), $PbSO_4$, or in its basic form $PbSO_4 \cdot PbO$, was used through this polyptych. This hypothesis is also supported by the results given by the PXRF instrument, where the relative concentration of S is greater for white samples (even greater than in samples containing vermilion, HgS). This is a peculiar result, since Flemish white is not usual, and is not even considered an historical pigment [48], however, given the large amount of samples investigated it seems that Bernardo Manuel did indeed use it. Still, there is also the possibility that lead sulphate may appear due to previous interventions, in particular the treatment of blackened white lead with ethereal peroxide [107]. It should also be noted that the location of the paintings between 1667 and 1915-1917 [6] is unknown and thus it could have been subjected to incorrect cleaning actions. Nonetheless, it would be interesting to study more extensively the use of white lead sulphates in this polyptych as well as in other artworks by Portuguese artists.

The µRS examination of samples P25-7, which corresponds to sample pxrf-p25-12, and P90-7, related to white grains, showed a single peak at $\sim 1050\,\mathrm{cm}^{-1}$ (Figure 5.12) which can be assigned to the $\upsilon_1(CO_3)$ symmetrical stretching band. While a doublet, at $1049\,\mathrm{cm}^{-1}$ and $1053\,\mathrm{cm}^{-1}$, is usually associated with the basic

---

[6] It may have belonged to the Institute of Coimbra in-between.

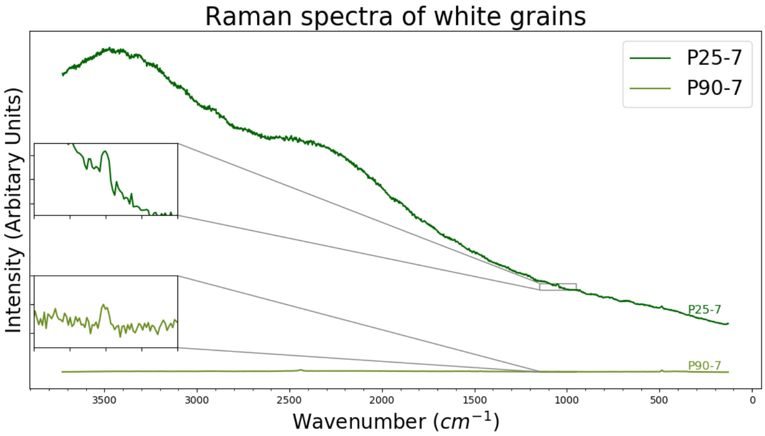

Figure 5.12: Raman spectra of white grains from samples P25-7 and P90-7. The region from 950 cm^{-1} to 1050 cm^{-1} is enlarged to emphasize the presence of a singlet in both spectra. The presence of a singlet in this region may be associated with the presence of non-basic lead carbonate or may be due to deficiencies of the experimental setup.

form of lead carbonate, known as lead white or by its scientific name lead hydroxycarbonate, a single peak implies the non-basic form, referred as lead carbonate or non-basic lead carbonate [48].

As for their geological origin, basic lead carbonate and non-basic lead carbonate can be extracted from the minerals hydrocerussite and cerussite, respectively. Likewise, non-basic lead carbonate is also a sub-product formed when metallic lead is converted into lead white and a degradation product of lead white due to atmospheric factors [30]. However, lead white is remarkable for its permanence and stability, and thus the hypothesis of non-basic lead carbonate having over time derived from the degradation of lead white is highly improbable.

The presence of non-basic lead carbonate may not have been premeditated, since its use is very unlikely in painting [124] however it is not unheard of, having been employed throughout the Ages [124, 85, 17] and even in Portugal [30, 123]. Therefore, the use of non-basic lead carbonate as a pigment, albeit unusual, should not be disregarded and, given the results obtained from the µRS, this conclusion does not seem far-fetched.

One other justification for the rising of a single band at ~1050 cm^{-1} is related with the spectral resolution of the experimental setup. Unfortunately, the spectral resolution of the experimental setup is not known, although other studies with similar setups propose the value $\sim 4\,\mathrm{cm}^{-1}$. Moreover, from a theoretical approach, the length of the illuminated grating must be larger than 7.39 mm [7]. This means that perhaps a doublet should appear instead of a singlet, but due to the setup a single band appears.

The use of a lead carbonate in the region of samples pxrf-p25-12 and P25-7 instead of a lead sulphate as is implied by the PCA results in the others white regions of the polyptych, including other flowers, may be an evidence that this flower may not have been present on the original painting. Moreover, even for the inexperienced eye, the vases and flowers on *Annunciation (P25)* and *Apparition of Christ to the Virgin (P27)* seem quite different, one other indication that they may have been painted by different painters. For a more reliable conclusion, an art historian should be consulted, since this difference may be associated with symbolism. As for sample P90-7, it was extracted from a red spot above the wing of the right angel on *Trinity (Eternal Father) (P90)*. However, a similar spot was not found on the left side, which given the symmetry of the painting suggests that this red paint may have been added during a posterior intervention.

Lastly, the PXRF analysis and the SEM/EDS analysis allowed to discard the use of barium white, zinc white and lithopone, since the elements Ba and Zn have not been detected.

5.4.2 Black Areas

The majority of black pigments used in Art are of organic origin, having in their composition carbon and so being classified as carbon-based pigments. Nonetheless, Bernardo Manuel seems to have used pigments rich in Cu to represent black not only in the backgrounds but also in small details. For example, the jewels worn by the Archangel Gabriel in *Annunciation (P25)*, corresponding to samples pxrf-p25-32 and pxrf-p25-40, and by Christ in *Apparition of Christ to the Virgin (P27)*, corresponding to sample pxrf-p27-49, have a black tone clearly due to a copper-

---

[7] This value is calculated using the Rayleigh criteria and it was further explained on Section 3.3.4.

based pigment, since the rate of Cu in these samples is very high, particularly when compared with samples pxrf-p25-33 and pxrf-p27-48, their respective backgrounds.

In general, there are not many black surfaces in this polyptych[8], however, black pigments are also used to darken surfaces. The most widely used black pigments are carbon-based, for which the PXRF analysis (or any ED-XRF analysis) is not suitable, since it cannot detect the elements C and O. As for the extracted samples, they are not numerous and mainly correspond to shade carnations. The samples of carnations were investigating using µRS analysis, but did not provide conclusive results. Nonetheless, the µRS analysis of sample P27-9 showed carbon bands. Given that sample P27-9 was extracted from a brown area, this subject is further discussed on Section 5.4.6 where its spectrum is shown (Figure 5.21).

5.4.3 Red Areas

Bernardo Manuel used the colour red in this polyptych mainly to paint robes of important figures and to add a red tone to carnations and lips. An hypothesis is the use of vermilion, HgS, to employ a red vivid tone.

Vermilion is very easily identified by elemental analysis, and was successfully so by PXRF and SEM/EDS, since the element Hg is not associated with other notable pigments nor layers other than the chromatic layer and is, as mentioned before, a very bright pigment. As for the µRS analysis of samples containing Hg it did not yield conclusive results, and thus it is not possible to affirm if either a natural or an artificial pigment was used.

Given the association of Hg with vermilion, the PCA using the relative intensities becomes very straightforward in distinguishing samples composed by vermilion. Thereby, red surfaces painted with vermilion are contained in Clusters 10, 11 and 14 of Table A.3.

Vermilion was used to colour the mantles of Archangel Gabriel (pxrf-p25-50) in *Annunciation (P25)*, and of Christ (pxrf-p27-50[9]) and of the clothes of the angels (pxrf-p90-18 and pxrf-p90-30) in *Trinity (Eternal Father) (P90)*. In *Lamentation of*

---

[8] The poor quality of the images of the paintings may suggest otherwise, however, most surfaces are mainly brown or green.

[9] Vermilion was also found in samples pxrf-p27-48 and pxrf-p27-49, indicating that vermilion was applied first.

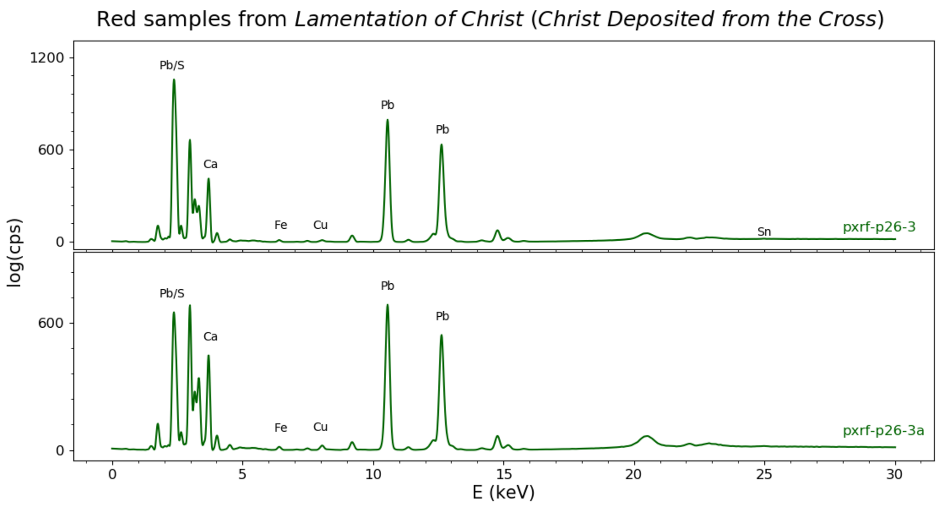

Figure 5.13: Red samples from *Lamentation of Christ (P26)*. Samples pxrf-p26-3 and pxrf-p26-3a do not have Hg nor high rates of Fe.

Christ (P26), vermilion was used more extensively to colour all clothes (pxrf-p26-1, pxrf-p26-2, pxrf-p26-4, pxrf-p26-5, pxrf-p26-6 and pxrf-p26-7) with the exception of the shirt of Nicodemus (pxrf-p26-3 and pxrf-p26-3a). As for representing blood, vermilion was only detected conclusively in sample pxrf-p26-7a along with Fe, indicating the increasing presence of red ochres, samples pxrf-p27-47 and pxrf-p90-14 also represent blood, however, the traces of Hg and Fe found are not as significant. In carnations, vermilion was used to colour cheeks (pxrf-p26-41, pxrf-p26-42, pxrf-p27-29, pxrf-p27-39, pxrf-p27-44 and pxrf-p90-7) as well as in all other instances of carnations, although with smaller rates, except in sample pxrf-p26-39. Sample pxrf-p26-39 was extracted from a very dark carnation where no element stands out using PXRF, meaning that it was probably darkened with a carbon-based black. Vermilion was also used for lips and in small details as flowers (pxrf-p25-14 and pxrf-p27-16), colouring skies (pxrf-p26-25 and pxrf-p27-2) as well as others (pxrf-p27-19, pxrf-p27-22, pxrf-p27-26, pxrf-p25-51 and pxrf-p25-58).

Bernardo Manuel also used red ochres, as the increasing presence of Fe indicates, to reproduce red and brown surfaces. Red ochre has a more brownish aspect than vermilion and thereby it was mainly used to paint hair and to draw lines in this polyptych. One such example of the latter is sample pxrf-p90-11, which corresponds to red and green drawings on a yellow surface. The pigments employed to paint the shirt of Nicodemus, corresponding to samples pxrf-p26-3, pxrf-p26-3a (the spectra of both is shown in Figure 5.13) and P26-5, were not identified. The µRS analysis did not yield any relevant bands and the PXRF analysis did not report Hg. As for the presence of Fe, the PXRF spectra shows low rates in both samples, $R_{Fe} = 15.20(27)$ in sample pxrf-p26-3 and $R_{Fe} = 19.82(29)$ in sample pxrf-p26-3a, particularly when compared with others, as for example sample pxrf-p26-4 where $R_{Fe} = 23.47(46)$. Therefore, it is not clear what compounds were applied

As for the use of red ochres for achieving a brownish aspect, it is discussed in Section 5.4.6.

5.4.4 Green and Blue Areas

In this section, the green and blue regions are discussed. The blue regions are included here since it can be difficult to differentiate blue from green and because blue is not a common colour in this polyptych. In fact, the only instance of blue, corresponding to samples pxrf-p25-9 and P25-5, seems to have been applied during a posterior intervention.

In general, the green areas of this polyptych have a higher rate of Cu than the background, implying that a copper-based pigment was applied. Also, no other element associated with green pigments, such as Cr, Zn or As, was identified. If any of these elements had been identified, it would indicate that an intervention had been performed or that the polyptych had been wrongfully dated, since their presence is associated with pigments synthesised in 19th century and beyond [14].

Of the green regions sampled, the only one that did not show intense peaks related to Cu was pxrf-p27-24. Curiously enough, the PXRF spectrum of sample pxrf-p27-25, obtained to analyse a detail painted above the surface of sample pxrf-p27-24, shows not only much more intense peaks of Cu, but also Sn, associated with lead tin yellow. One possible explanation is that the region where sample pxrf-p27-24 was obtained, which seemed darker than the green region of sample pxrf-p27-25, was in fact painted with a black carbon-based pigment. This is also sustained by the fairly small rate of Cu, $R_{Cu} = 54.63(96)$ in sample pxrf-p27-24 whereas the same rate in sample pxrf-p27-25 is $R_{Cu} = 1559.79(4515)$. This difference is also

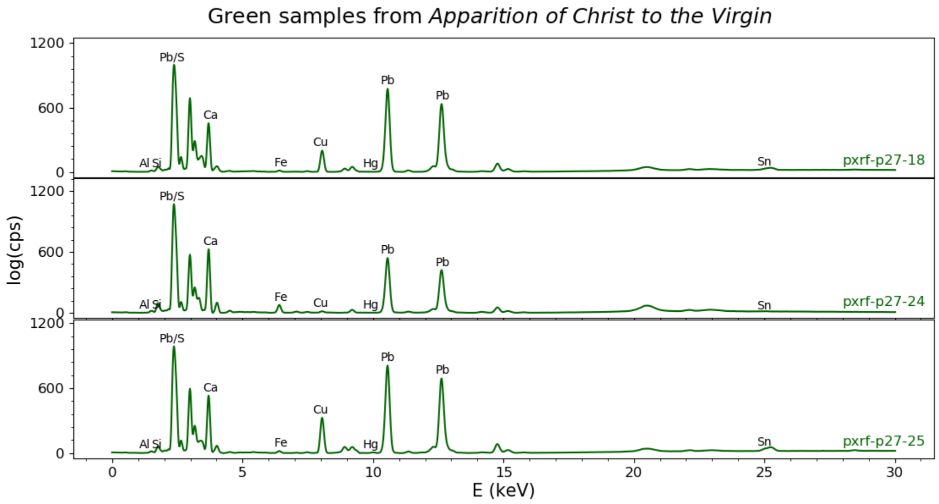

Figure 5.14: Green samples from *Apparition of Christ to the Virgin (P27)*. Despite the dark green aspect of sample pxrf-p27-25, it has Hg in its composition.

supported by the relative concentrations given by the PXRF instrument. This implies that maybe in this case the dark tone was not achieved by applying a copper-based pigment but a carbon-based one, undetectable through the PXRF analysis. Furthermore, sample pxrf-p27-25 is very peculiar, being a mixture of Cu, Hg and Sn, among others. One can speculate that Bernardo Manuel tried to paint this tassel in the same manner that he painted the tassel on the flag that Christ holds, but created an undesirable colour, due to incompatibilities with the background, and mixed or applied over a paint containing Cu and Hg after, which also create an yellow tone. Sample pxrf-p27-18 also has Sn in its composition, however, in this case is feasible that lead tin yellow was used to create lighter vegetation. Figure 5.14 shows the PXRF spectra of samples pxrf-p27-18, pxrf-p27-24 and pxrf-p27-25 for comparison.

As for the µRS analysis, samples P25-6 and P90-6 reported interesting results when green grains were analysed. The green in sample P25-6 seems to correspond to a lower layer of the yellow brownish paint, as Section 5.4.4 shows, and therefore it is attributed to the green of the wing of the Angel while in sample P90-6 the green tone belongs to the *imprimatura* layer. In both cases, a band at $\sim 550\,\mathrm{cm}^{-1}$ is observable, as Figure 5.15 shows. This band can be attributed to pigments

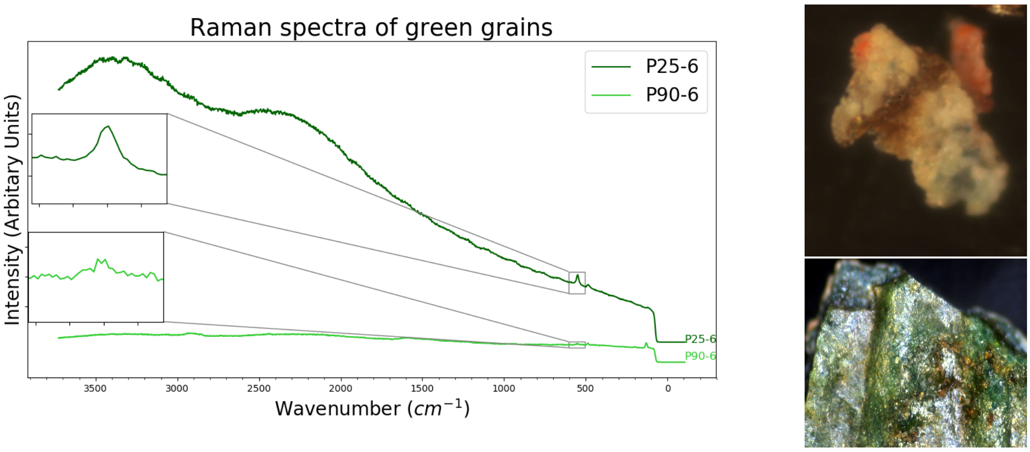

Figure 5.15: Raman spectra of samples P25-6 and P90-6 (on the left), photomicrographs of samples P25-6 (on the top) and P90-6 (on the bottom). The spectra of both samples shows a band at ~550 cm^{-1}, which can be assigned to Si–O–Al vibrations present on green earth pigments.

with chromium oxides (Cr_mO_n) in their composition, such as chromium oxide and viridian, which are green, and zinc yellow. The issue of associating this band to this type of pigments is that they were all synthesised in the 19th century, meaning that this paint must have been applied in an intervention. However, being underlayers, and in the case of P90-6 an *imprimatura*, this intervention would have caused major changes in the polyptych. Fortunately, this band can also be assigned to the Si–O–Al in-plane vibrations [43]. The elements Si and Al and the colour green allows one to assume that green earth (*terre-verte*) was employed. Moreover, the existence of this prominent band and lack of others, suggests the presence of celadonite, a clayey mica constituent of green earth [91].

5.4.5 Yellow Areas

With a few exceptions, where it was considered relevant to discuss the subject, gilded surfaces are not discussed here, but instead on Section 5.5.

In the majority of the yellow regions of all four paintings, lead tin yellow was identified using PXRF and SEM/EDS, since the presence of Sn and high rates of Pb are strong enough indicators of the presence of lead tin yellow. As for the µRS spectra of the extracted samples, it did not show any characteristic bands of lead

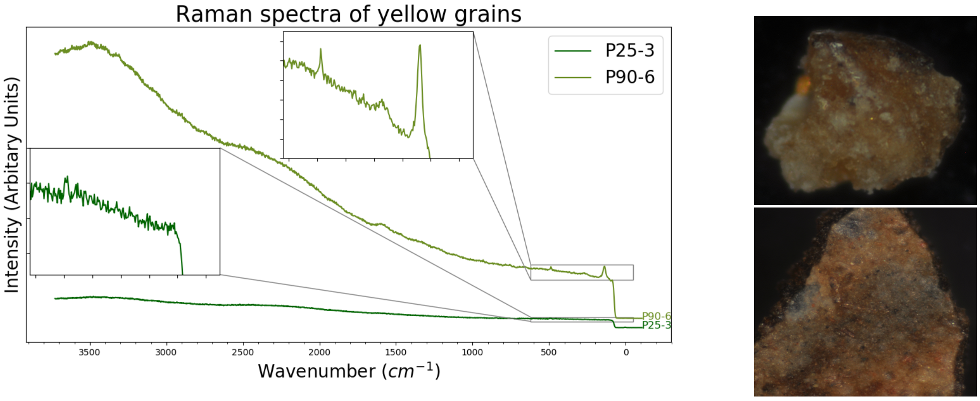

Figure 5.16: Raman spectra of samples P25-3 and P90-6 (on the left), and photomicrographs of samples P25-3 (on the top) and P90-6 (on the bottom). The spectrum of sample P90-6 show a band at 138 cm^{-1}, which may be associated with the degradation of lead tin yellow, while the spectrum of sample P25-3 does not.

tin yellow, although the band at 138 cm^{-1} in the sample P90-6 (Figure 5.16) may be associated with the degradation of plattnerite, PbO_2, and thus with lead tin yellow. The spectrum of sample P90-6 in Figure 5.16 shows a band at 485 cm^{-1}, which appear in several other samples and may be due to $C-H$ bonds [10] [75]. Moreover, Figure 5.16 shows the spectrum of another yellow grain in sample P25-3, where no bands were discernible. However, it should be noted that the yellow samples extracted were so due to presence of gold alloys, which could have affected the µRS analysis, since gold alloys reflect most of the incident radiation, and therefore, lead tin yellow is present only on a few samples.

In *Annunciation (P25)*, lead tin yellow was used on the surfaces related to the Archangel Gabriel, bright yellows related with divine intervention and in a few brown surfaces. In his wing, vermilion was applied to perform the red threads seemingly overlaying lead tin yellow while the paint used on his sceptre has Sn (pxrf-p25-55) and Cu (pxrf-p25-56), but not Hg, in its composition. As for his clothes, the PXRF spectra of samples pxrf-p25-42 and pxrf-p25-49 show the peak associated to Sn KL_3 while the spectrum of sample pxrf-p25-39 does not. Sample pxrf-p25-39 does not seem to have Sn in its composition, but instead a somewhat high rate of Cu, $R_{Cu} = 1199.51(1726)$, suggesting once more the use of copper-

---

[10] The covalent bond is not necessarily single and molecules, such as CH_3 may be involved [75].

based pigments to produce darker tones. Moreover, the presence of Cu may have prevented the peaks associated with Sn from rising, particularly if Cu was applied after lead tin yellow. Nonetheless, note that sample pxrf-p25-34, which corresponds to the crown of the Archangel, has both Cu and Sn in its composition.

The Holy Spirit takes a central place in this artwork, with a large cloud and a dove placed between the Virgin and the Archangel. Moreover, the yellow surface on the inside of the cloud, which corresponds to sample pxrf-p26-4, was painted using lead tin yellow while the ray expelled by the dove has not only lead tin yellow in its composition but also vermilion, to reproduce the red tones, and a gold alloy to increase even more the brightness of this region. The halo of the Virgin (samples pxrf-p25-21 and pxrf-p25-30), another symbol of divine intervention, was also painted with lead tin yellow and a gold alloy of high purity, i.e. , with low contributions of Cu and Ag. Figure 5.17 shows the elemental mappings [11] of sample P25-3 concerning the elements Sn and Au on the right, and spectra acquired on the marked points, on the left.

In *Lamentation of Christ (P26)*, the vegetation occupies a great portion of the painting and therefore the vivid colours are left for the clothes. Thus, lead tin yellow was only used on the clothes of Joseph of Arimathea and on the mantle of one of the Holy Women, corresponding to samples pxrf-p26-38 and pxrf-p26-14 respectively.

Apparition of Christ to the Virgin (P27), as *Lamentation of Christ (P26)*, does not have a high number of yellow surfaces (excluding gilded surfaces). However, Bernardo Manuel used lead tin yellow in the sceptre of Christ (pxrf-p27-57) and therefore both its aspect and PXRF spectrum are very similar to sample pxrf-p25-55. The PXRF spectra of both samples can be observed on Figure 5.18. Lead tin yellow was also used to reproduce the tassels corresponding to samples pxrf-p27-25 and pxrf-p27-54, however, pxrf-p27-25 has a more complex PXRF spectrum with Cu and Hg present, which when mixed, create an yellow tone. As discussed in Section 5.4.4, this mixture may have been applied due to incompatibilities with the background.

The painting *Trinity (Eternal Father) (P90)* is much lighter than the other

---

[11] The elemental mappings are obtained due to the contrast, C_{tr}, of different locations, as described on Section 3.2.1.

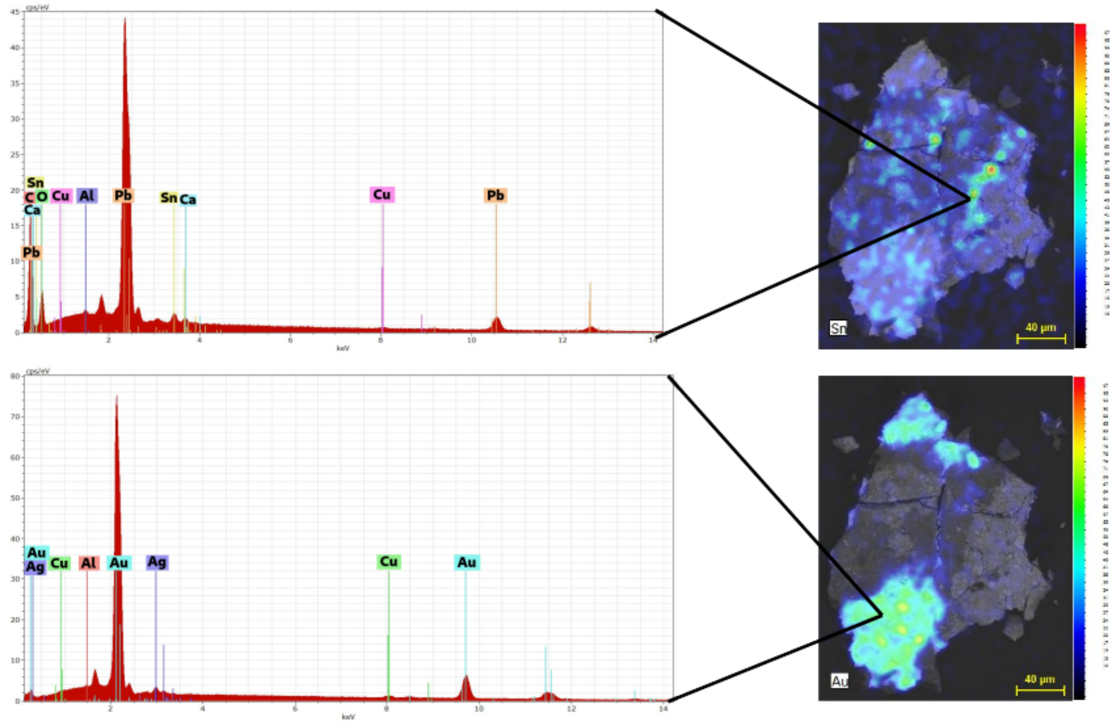

Figure 5.17: Elemental mappings of sample P25-3 concerning the elements Sn and Au on the right, and spectra acquired on the marked points, on the left. The spectrum on the top shows the presence of Sn and Pb, associated with lead tin yellow, while the spectrum on the bottom suggests a gold alloy of high purity.

paintings of this polyptych, as if to highlight the figure of the Father. Moreover, gold alloys were here used frequently and in fact all yellow regions, with exception of the background and small details, were coloured using gold alloys, even the largest ones, such as the mantle of the Father and His shield. Nonetheless, lead tin yellow was used along with a gold alloy to colour the mantle of the Father, as the PXRF spectra of samples pxrf-p90-9, pxrf-p90-10 and pxrf-p90-11 in Figure 5.19 indicates [12], and the edge of the breastplates of the Angels in pxrf-p90-30. Moreover, Figure 5.23 shows that a gold alloy was applied over a layer of lead tin yellow.

On analysed spots with PXRF of the triangular halo and of the shield, no traces of Sn nor a high rate of Fe were found, which excludes the use of lead tin yellow and of ochres. However, sample P90-3 (Figure 5.23) was extracted and analysed

---

[12] Three spots were analysed not due to differences of the yellow paint, but due to small red and green drawings along mantle.

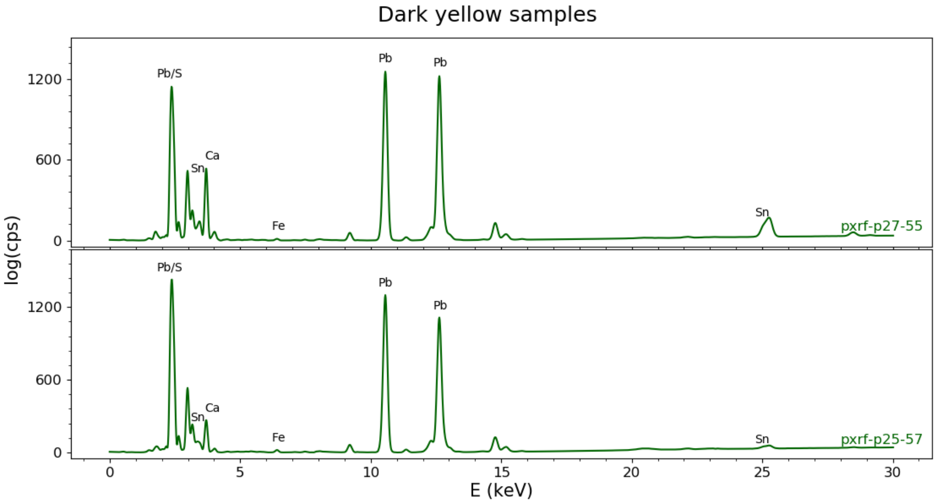

Figure 5.18: PXRF spectra of dark yellow samples.

with SEM/EDS from a similar region (the mantle), showing the presence of Sn on a layer underneath the gold alloy, indicating that the peaks associated with Sn may not have risen. Bernardo Manuel also used lead tin yellow on the wings of the Angels (pxrf-p90-24), still it should be noted that it seems to have been applied discontinuously and with similar intensities, while in the wing of the Archangel in *Annunciation (P25)* it was applied in a continuous drawing culminating in a more intense region.

Regarding the PCA analysis, it seems that the Clusters 3 and 9 from Table A.3 are formed due to the presence of lead tin yellow. Lastly, the presence of lead tin yellow in brown regions is discussed on Section 5.4.6.

5.4.6 Brown Areas

Brown colours are employed in this polyptych mainly in the backgrounds, hairs and other small details. Also, in general, the PXRF spectra of these samples indicate a high rate of Fe, which in its turn suggests the use of ochres. Figure 5.20 shows the PXRF spectra of several samples collected from the hairs of the characters of the several paintings. As for the analysis using µRS and SEM/EDS, only two samples, P27-7 and P27-9, were extracted, both located on flaws in the artwork *Apparition*

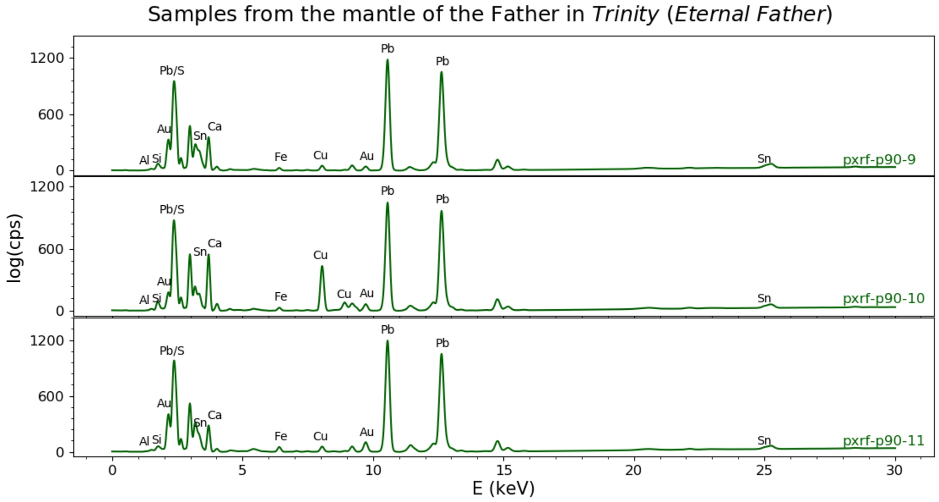

Figure 5.19: Samples pxrf-p90-9, pxrf-p90-10 and pxrf-p90-11, belonging to the mantle of the Father *Trinity (Eternal Father) (P90)*. Sample pxrf-p90-10 has green drawings, and thus its Cu contribution is larger, while sample pxrf-p90-11 has red drawings, and thus its Fe contribution is larger.

of Christ to the Virgin (P27), in order to not jeopardize the painting.

The use of brown colours on the backgrounds of the paintings are not here discussed, since they were already on Section 5.3.

In *Annunciation (P25)*, one brown surface that stands out is the table where the Virgin is leaned. Also, the book she is reading has an yellow brownish aspect. These surfaces were all analysed using PXRF, which corresponds to samples pxrf-p25-17 to pxrf-p25-20. These samples all have higher rates of Fe, from $R_{Fe} = 26.06(33)$ to $R_{Fe} = 285.42(702)$, than their possible background, sample pxrf-p25-1 with $R_{Fe} = 24.55(58)$, implying the presence of ochres.

Samples pxrf-p25-19 and pxrf-p25-20 are very similar, but the surface on pxrf-p25-20 is lighter. This is also reflected on their PXRF spectra, where pxrf-p25-20 has a well developed Hg $\mathrm{KL_3}$ peak, normally associated with the pigment vermilion. Moreover, Cu was detected on samples pxrf-p25-17 and pxrf-p25-18 and Sn in sample pxrf-p25-17, indicating that a copper-based pigment was used to reproduce a more dark tone and lead tin yellow to reproduce the yellow aspect. Still regarding the scenery, the floor is covered with standardized mosaics with brown

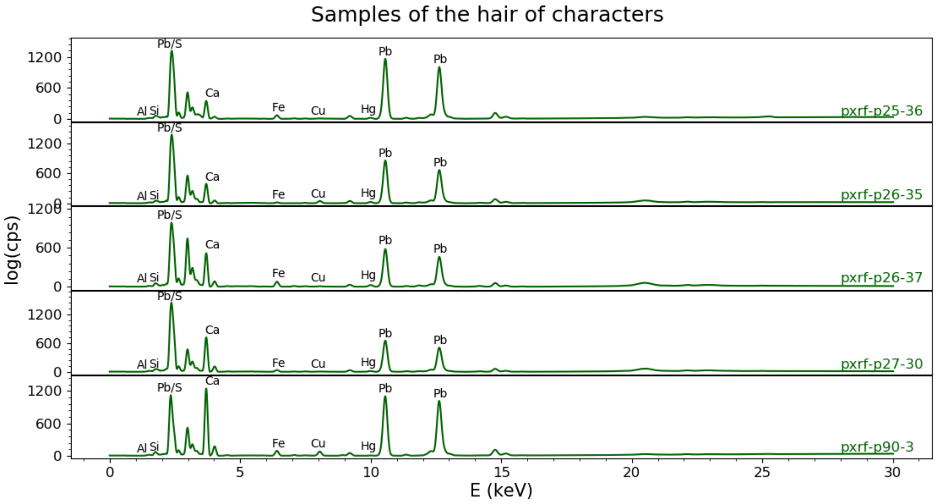

Figure 5.20: PXRF spectra of samples concerning the hair of several characters.

corners, where sample `pxrf-p25-11` was analysed. This sample shows a lower rate of Fe, $R_{Fe} = 11.35(25)$, than the samples referred before, whereas its rate of Cu, $R_{Cu} = 525.88(501)$, is much larger. These results are in agreement with the relative concentrations acquired by the PXRF device. This suggests that a copper-based pigment was used instead of an iron-based one to paint this region. A similar analysis was conducted relatively to the hair of the characters, which seems to have been painted with a mixture of ochre and vermilion, and to the the brown belt of the Archangel, which appears to have been painted using only an ochre. These results are consistent with the quantitative data calculated by the PXRF equipment.

In *Lamentation of Christ (P26)*, brown areas are mostly scattered across the background, however, as mentioned this will not be discussed here. Therefore, brown areas mainly correspond to the crosses on the right corner, the tray in the hands of the man on the right and the hairs of the characters. All brown spots analysed with PXRF, samples `pxrf-p26-33` to `pxrf-p26-37`, show the greatest rates of Fe along the samples analysed from the painting *Lamentation of Christ (P26)*, implying once more the presence of ochres. Along with the presence of ochres, the spectra suggested the use of vermilion, particularly to reproduce the dark brown hair of the characters. On sample `pxrf-p26-34`, Sn was also identified, implying

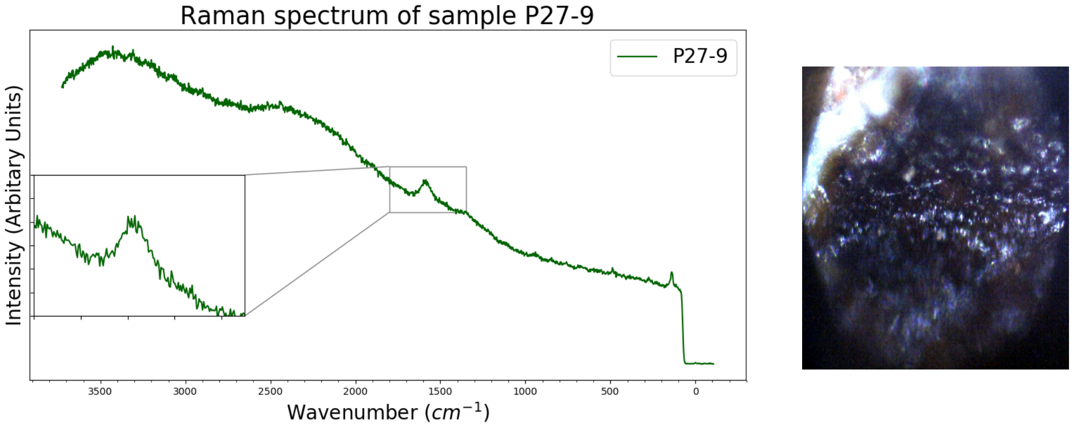

Figure 5.21: Raman spectrum of sample P27-9 (on the left) and photomicrographs of sample P27-9 (on the right). The spectrum shows a broad band at ~1580 cm^{-1}, which due to its location and broadness is associated with carbon bonds present in organic black pigments.

that lead tin yellow was also employed.

In *Apparition of Christ to the Virgin (P27)*, the use of brown is very similar to *Annunciation (P25)*, in so far as it was used on furniture, the floors and hair.

In lighter surfaces, such as samples pxrf-p27-9 and pxrf-p27-30, the rate of Fe increases while the rate of Cu decreases. In the case of sample pxrf-p27-30, the rate of Ca is also high. The presence of Ca is common in carbon-based black pigments (charcoal) of animal source, which in this case may have been applied to reproduce the several strands of hair. The hypothesis that a carbon-based black pigment was employed in the painting of brown surfaces is also supported by the µRS analysis of sample P27-9, which shows a broad band centred at ~1582 cm^{-1}. A second band should be observed at ~1340 cm^{-1} and may in fact exist, but be indiscernible. Still, the presence of the band at ~1582 cm^{-1} in the µRS spectra, along with the significant presence of Ca and the dark colour of the sample, indicates the use of an animal charcoal. The µRS spectrum of sample P27-9 is shown in Figure 5.21, where it can also be observed bands at 138 cm^{-1} and 485 cm^{-1}. In the case of the former band, it may be attributed to the degradation of plattnerite, PbO_2, and associated with a lead material, while the latter may be due to C−H bonds [13] [75].

---

[13] The covalent bond is not necessarily single and molecules, such as CH_3 may be involved [75].

Table 5.2: Main results concerning the chromatic layer.

Pigment	Colour	PXRF	SEM/EDS	µRS
Flemish white?	White	Pb, S	n/a	n/a
Non-basic lead carbonate	White	Pb	n/a	$\upsilon_1(CO_3)$ at ~1050 cm^{-1}
Copper-based	Black	Cu	n/a	n/a
Carbon-based	Black/brown	Ca?, S?	n/a	Broad band at ~1580 cm^{-1}
Vermilion	Red	Hg, S	Hg, S	n/a
Red ochres	Red/brown	Fe	n/a	n/a
Copper-based	Green	Cu	n/a	n/a
Green-earth (celadonite?)	Green	Al, Si	n/a	Si–O–Al at ~550 cm^{-1}
Lead tin yellow	Yellow	Pb, Sn	Pb, Sn	PbO_2? at ~138 cm^{-1}
Mixture of Cu and Hg	Yellow	Cu, Hg	n/a	PbO_2? at ~138 cm^{-1}

Lastly, in *Trinity (Eternal Father) (P90)*, the use of brown is restricted to hair and only one spot, the hair of the Father, was analysed using PXRF, since the hair of the angels shows low opacity and, thus, the results would have a large contribution from the background. Therefore, sample `pxrf-p90-3` does not differ greatly from the samples of hair in the other paintings, however, it does have a higher rate of Cu and Ca. Given that it is a very dark tone of brown it can be speculated that once more a charcoal was used along with a copper-based pigment.

5.5 Gold alloys

In a first approach, surfaces whose colour and brightness suggested the presence of gold alloys were subjected to a PXRF analysis. The PXRF analysis allowed the detection of Au even in situations where its content was low comparatively with other elements. However, it did not provide much more conclusive information concerning the composition of gold alloys. Along with Au, Cu and Ag are major elements of gold alloys while other elements are regarded as trace elements. In the case of Cu, it is not possible to measure only the contribution of Cu from the gold alloy, since the X-rays used in PXRF have a high penetration ability and thus, the results display contributions from inner layers. As for Ag, the analysis was performed using the mode *TestAll Geo*, which does not compensate the contribution of the Ag anode.

Given the inconclusively nature of the PXRF results regarding the composition of gold alloys and the importance of the study of these in the appreciation of Cultural Heritage assets, representative samples were extracted from the four artworks. These samples were then analysed using SEM/EDS, whose electrons do not penetrate so greatly into the sample, assessing the correct contribution of Cu, and whose anode is of W. The samples were not investigated using µRS, since metals, particularly gold alloys, have high reflectance. The small penetration of electrons allowed the study of exposed layers. Therefore, Figure 5.23 illustrates the spectra of sample P90-3 in two different layers, showing that a gold alloy was applied over a lead tin yellow, as the presence of Pb and Sn.

The extracted samples were analysed in several points, however, in Table 5.3 [14] only the points where the sum of Cu, Ag and Au contributions correspond to the larger weight percent (*wt.* %) of the sample were considered. Moreover, the last column of this table refers to the weight percentage explained by Cu, Ag and Au in each sample.

From the results on Table 5.3 it can be concluded that Bernardo Manuel employed an alloy with high content of Au compared with Ag and Cu. In fact, if only these elements are considered, the purity of the gold alloys present in this polyptych ranges from 22.79 C to 23.98 C.

For a better visualisation, the results of Table 5.3 are also expressed on Figure 5.22 in red, where they are compared with some of the results that Afonso Coxito obtained during his Masters dissertation [31]. In it, Afonso Coxito studied nineteen objects from the 15th century to the 18th century from the region of Coimbra, using SEM/EDS, PXRF and ED-XRF (bench top equipment). In Figure 5.22, the results obtained via SEM/EDS and ED-XRF analysis are shown in black, if the objects are from the 16th century, and grey, if not, while the results of the PXRF analysis, which only concern the *Triptych of Saint Clare*, attributed

---

[14] In this table, the uncertainties are expressed on their concise form. For example, 5.01(2) should be read as 5.01 ± 0.02 while 5.01(200) should be read as 5.01 ± 2.00.

Table 5.3: Composition of gold alloys considering the three major elements Au-Ag-Cu. Bernardo Manuel used gold alloys rich in Au in this polyptych.

Samples	Au [wt.%]	Ag [wt.%]	Cu [wt.%]	Total [wt.%]
P25-3	94.96(63)	3.30(49)	1.75(30)	85.87(717)
P26-3	99.90(18)	0.07(13)	0.03(13)	70.10(625)
P27-3	97.01(41)	1.13(23)	1.86(30)	99.07(845)
P27-4	98.75(28)	0.97(23)	0.28(15)	74.93(653)
P27-5	96.74(88)	0.09(36)	3.17(81)	22.07(213)
P90-3	98.45(31)	0.75(20)	0.80(22)	77.63(678)
P90-4	97.28(40)	0.61(17)	2.11(34)	91.13(783)

to Vicente Gil, the grandfather of Bernardo Manuel, the first generation of the Workshop of Coimbra, are in blue. The PXRF results are not considered as reliable as the results of the other two techniques, since they are affected by the Cu contribution of inner layers[15], however, it is important to assess the evolution of the Workshop of Coimbra.

From Figure 5.22, it can be concluded that Bernardo Manuel employed purer gold alloys than his contemporaries and his grandfather. Nonetheless, the results here obtained are in good agreement with the ones obtained in [76], related with the gilding of the Old Cathedral of Coimbra in 1583. In addition, from the position on Figure 5.22 and the aspect of the samples, Bernardo Manuel only used yellow gold alloys (a high content of Cu would provide redder alloys and a high content of Ag greener ones).

These samples were also examined concerning the amounts of Pt, Pd, Te and Sn. These elements are of special importance in uncovering the provenance of gold alloys. Moreover, the provenance of a gold alloy may indicate a time period of application, since the Portuguese gold trade networks over time are well documented. Unfortunately, these elements are of difficult detection and quantification due to the proximity of their main detectable peaks with of other elements (Pt

---

[15] Afonso Coxito refers that the Ag contribution of the anode is compensated by the software. Although, he does not specify it, he most likely employed the mode *Precious Metals*, which provides this compensation.

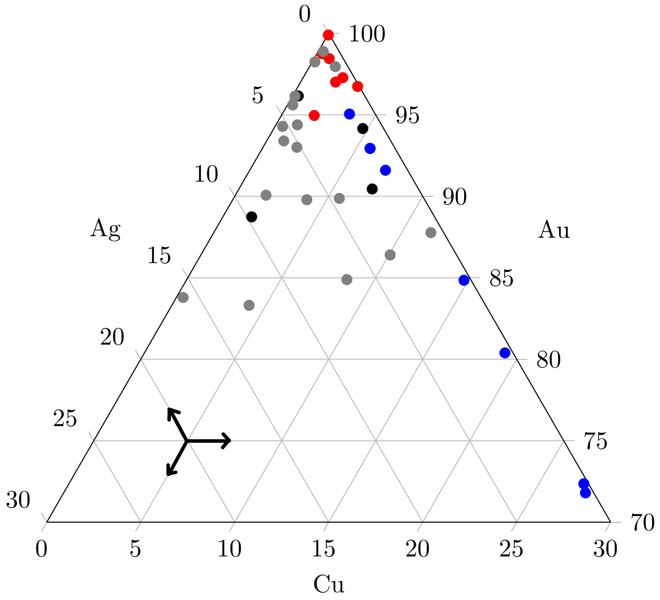

Figure 5.22: Ternary plot showing the composition of the three major elements, Au-Ag-Cu, in gold alloys. The results obtained in this project (from Table 5.3) are shown in red while in black are results obtained from gold samples applied during the 16th century [31], in grey the ones concerning objects from other centuries [31] and in blue the ones obtained from the artwork *Triptych of Saint Clare*, attributed to Vicente Gil, grandfather of Bernardo Manuel [31].

at 9.434 keV and Au at 9.705 keV, Pd at 2.883 keV and Ag at 2.984 keV, Te at 3.768 keV and Ca at 3.691 keV, and Sn at 3.444 keV and Ag (L_2N_1 transition) at 3.428 32 keV [16, 126]).

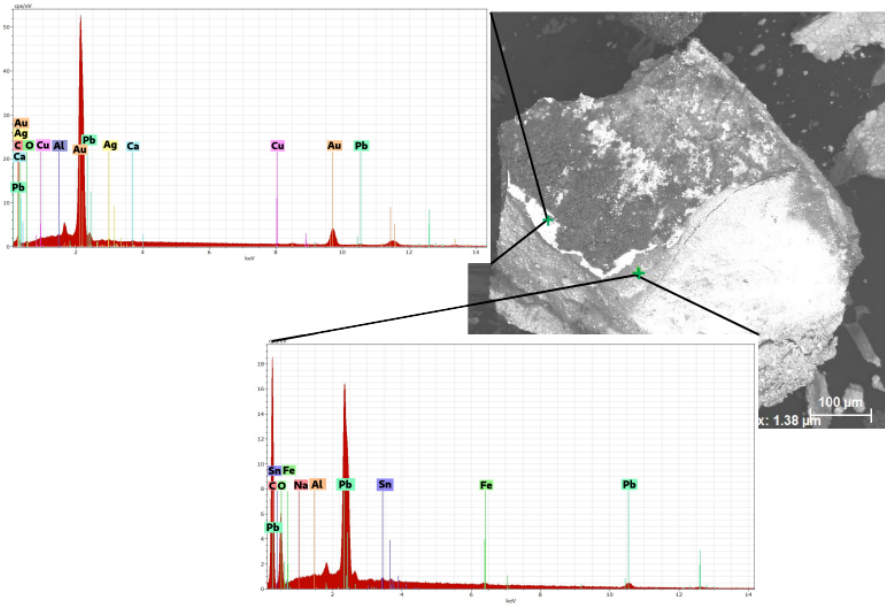

Figure 5.23: Image and spectra of sample P90-3 obtained by SEM/EDS. The spectra presented show that a gold alloy of high purity was applied over lead tin yellow.

Table 5.4: Contribution of trace elements in gold alloys (Pt, Pd, Te and Sn).

Samples	Au [wt.%]	Pt [wt.%]	Pd [wt.%]	Te [wt.%]	Sn [wt.%]	Total [wt.%]
P25-3	98.47(1213)	0.00(0)	1.31(26)	0.05(11)	0.18(12)	84.26(728)
P26-3	98.25(1235)	0.00(0)	0.00(0)	1.31(31)	0.44(20)	54.96(484)
P27-3	98.63(1216)	0.00(0)	0.00(0)	0.80(19)	0.57(17)	98.06(849)
P27-4	98.30(1218)	0.00(0)	0.09(12)	0.19(13)	1.42(28)	75.21(653)
P27-5 (1)	64.24(840)	0.00(0)	0.00(0)	23.38(334)	12.37(213)	10.99(84)
P27-5 (2)	57.10(824)	0.00(0)	0.00(0)	0.00(0)	42.90(628)	12.26(103)
P90-3	98.84(1232)	0.00(0)	0.00(0)	0.79(22)	0.37(16)	77.61(680)
P90-4	92.78(1118)	0.18(14)	0.00(0)	4.58(63)	2.46(39)	94.57(776)

Unfortunately, given the results on Table 5.4[16], it is not possible to establish a parallel between the content of the elements Pt and Pd and the historical period of their application. Still, the analysis of sample P27-5 in several points revealed a higher content of Sn and of Te than in other samples. This sample was extracted from a star on the mantle of Christ, which has a blurry aspect that does not resemble the other stars from this polyptych. Given the content of Sn and different aspect, it can be speculated that these stars were added during an intervention. As for the presence of Te, it is more common on gold alloys from India after the 16th century, however, it may have been accounted instead of Ca [16].

---

[16] In this table, the uncertainties are expressed on their concise form. For example, 5.01(2) should be read as 5.01 ± 0.02 while 5.01(200) should be read as 5.01 ± 2.00.

Chapter 6

Conclusions

In this dissertation, the spectroscopic techniques OM, PXRF, µRS and SEM/EDS were used to study a set of four paintings (a polyptych) from the 16th century attributed to Bernardo Manuel and belonging to the MNMC. Unfortunately, it was not possible to use the ED-XRF bench-top equipment due to reasons external to this project. Still, the techniques used allowed a good characterisation of the polyptych in question.

PXRF was extremely useful during this dissertation, providing an overview of the four artworks. Moreover, being a multi-elemental with low data acquisition times technique, it allowed the study of a large sample set in a short amount of time, causing as little inconvenience as possible to the staff of MNMC. As for the PXRF instrument, it provided well-defined spectra, however, the process of identification and quantification of elements reported some flaws. One major issue of this process is the lack of documentation, since the user guide of the device, [125], does not explicitly describe the methods employed. As such, in many instances it is not possible to verify if the elements were correctly identified and/or quantified. Moreover, many elements were found with large relative errors, which as the user guide describes, should be "considered qualitative or semi-quantitative at best" and all samples have more than one element with relative error larger than 20 %. For these reasons, *relative intensities* or *rates* (R) were calculated using the spectra of the whole sample set. Although the rates calculated do not take into account factors such as calibration and matrix effects, they are generally consistent with the quantitative data given by the PXRF instrument when the latter shows small relative errors.

The rates calculated and the data given by the PXRF instrument, concerning only elements that were most likely correctly identified by the PXRF instrument and/or important in the study of historical pigments, were subjected to a PCA analysis and posterior clustering, in order to correlate different elements as well as find similar samples and correlate them with the given elements. In the case of the quantitative data given by the PXRF instrument, the clusters do not appear to be associated with any pigment, since they contain samples of different colours and aspects. However, when using the rates calculated, there is a clear association of the elements Pb and S with white samples (except sample `pxrf-p25.12`), and thus, white samples are contained on Clusters 5 and 15 from Table A.3. The same occurs for samples containing vermilion, the only known historical pigment containing Hg, forming the Clusters 10, 11 and 14 and yellow samples containing lead tin yellow, associated with the presence of Pb and Sn, forming the Clusters 3 and 9.

The presence of lead sulphates, possibly as Flemish white, in such a great number of white samples is very peculiar, since Flemish white is not considered an historical pigment. However, lead sulphate exists in the Nature as anglesite, and Bernardo Manuel probably had access to it. Still, one other hypothesis is that lead sulphates appear due to posterior interventions or incorrect cleaning actions. Unfortunately, the location of the polyptych between 1667 to 1915-1917 is unknown, and, thus, its conservation and restoration conditions are also unknown.

The PXRF analysis, in all sets of data (qualitative, quantitative and rates calculated), also provided good insights concerning the presence of Fe in brown samples and of Cu in green and even black samples. The use of Cu to create black tones is particularly interesting, given that black is usually achieved using carbon-based pigments. Nonetheless, carbon-based black pigments were indeed identified using µRS, a technique, which provides good evidence of their existence.

The µRS analysis also revealed the nature of the preparatory and surface layers in some cases. It determined conclusively the presence of *gesso* in the preparatory layers *Annunciation (P25)*, *Apparition of Christ to the Virgin (P27)* and *Trinity (Eternal Father) (P90)*, the presence of a proteinaceous media in the surface layers of *Annunciation (P25)* and *Lamentation of Christ (P26)* and the presence of a polysacchariDeous media in *Apparition of Christ to the Virgin (P27)* in its surface layer. Moreover, the µRS analysis allowed to conclude that green earth (*terre-verte*), was employed as the *imprimatura* of *Trinity (Eternal Father) (P90)*, whereas in the other paintings the chromatic layer seems to have been applied directly on the preparatory layer. It was also verified that green earth was employed in a small detail on the right corner of *Annunciation (P25).* In the case of *Lamentation of Christ (P26)*, it was not possible to find any materials related with the preparatory layer, which may have occurred due to the thick surface layer preventing the laser from reaching the preparatory layer. As for *Trinity (Eternal Father) (P90)*, it appears to have a much thinner surface layer and therefore, no suitable sample relating the study of surface layer was found.

Regarding the SEM/EDS analysis, it was particularly useful in the study of gold alloys, given that the small penetration of the electrons allowed to study the gilded layer without Cu contributions from the inner layers. The results obtained showed that Bernardo Manuel used a high purity gold alloy (in general, 23 C), which suggests that during the last decades of the 16th century, the Workshop of Coimbra was still very renowned and that high-quality materials were at their disposal. The comparison of the results obtained with other objects of the same century and the painting *Triptych of St. Clare* attributed to his grandfather, Vicente Gil, and studied by Afonso Coxito during his MSc. Dissertation, shows, once more that the gilding in this polyptych is of the highest quality, but still in good agreement with other artworks. The purity of the gold alloys applied is also very similar to the ones applied in the Old Cathedral of Coimbra in 1583, which, despite the sociopolitical difficulties that Portugal was experiencing, may be an indicator of prosperity in Coimbra. Regarding the provenance of the gold alloys, no conclusively results were achieved, which is a unfortunate, given that it could provide additional evidence for the dating of the artworks, posterior interventions and even provide new information regarding the Portuguese trade routes before, during and after the formation and loss of the Portuguese Empire.

Concerning the overall characterisation of the artworks, there are definitely many similarities between the paintings, not only regarding the preparatory and surface layers, but also concerning the pigments found. These similarities support the theory that they are in fact a polyptych that can be attributed to the same artist/workshop. Still, there are a few aspects worth-mentioning that differ. For example, vermilion was only used in one instance to represent blood. Even within the same painting, there are instances that do not seem consistent. One such example is the yellow tassels in *Apparition of Christ to the Virgin (P27)*, which although similar in aspect, vary greatly in composition. Still, this is not reason enough to conclude that an intervention was performed, since it is possible that due to the different background the same pigment did not provide the same aspect, and therefore, the artist chose a different mixture.

One aspect that is more probably due to a posterior intervention can be found in the painting *Annunciation (P25)*, between the Virgin Mary and the vase. This is the only region in the whole polyptych with a blue colour and it partially covers the tallest lily of vase. Moreover, the PXRF spectrum of this sample does not differ greatly from the spectra of other nearby regions. Unfortunately, the µRS analysis did not provided answers. As for the vase, the white lily corresponds to the only instance where the colour white appears and lead sulphate was not found, and the decoration of the vase seems quite different from the vase in *Apparition of Christ to the Virgin (P27)*, however, this subject should be clarified by an art historian.

Regarding the proposed constitution of the polyptych by Ana Maria Goulão, it can be concluded that the painting *Trinity (Eternal Father) (P90)* probably occupied a prominent position, as she suggested, since gold alloys were employed often and even in large areas.

In sum, regarding the techniques employed, it can be concluded that the main strength of PXRF is providing an overview of the artworks in a short amount of time, without jeopardising them. Moreover, it pointed conclusively the presence of several pigments and suggested the presence of others. However, it does not discriminate contributions from different layers. Therefore, the complementary use of PXRF and SEM/EDS is a good strategy, since PXRF can be used as a first approach, in order to decide which micro-samples should be extracted while SEM/EDS is able to study layer per layer (as long as they are exposed). As for the µRS analysis, in this dissertation, it was very useful in determining organic medias, such as the ones from surface layers and carbon-based pigments. Concerning the results found, it can be concluded that, although a few aspects differ from painting to painting, the attribution to the same artist/workshop is supported by the results. Nonetheless, there are a few aspects that seem to have been modified during posterior interventions.

6.1 Future Work

Even though the results allowed to draw some conclusions, it would be interesting to study this polyptych using other techniques and different setups, particular in the case of the extracted samples. For example, the µRS analysis may yield more conclusive results if lasers of greater wavelengths, such as 633 nm, are used. As for techniques, X-ray imaging (radiography) is quite suitable in the study of inner layers and of the support of paintings.

In the future, it would also be interesting to investigate the artworks *St. John the Evangelist* and *St. John the Baptist* belonging to the monastery of Santa Clara-a-Nova, in order to attest the hypothesis that these were painted by Bernardo Manuel. Moreover, other paintings attributed to the Workshop of Coimbra should also be investigated, since it was a renowned and prolific Workshop during the 16th century.

Regarding the study of gold alloys, it is integrated in a larger project led by Prof. Dr. Francisco Gil, which is certainly worth continuing, since it allows to draw parallels between artists and historical periods. However, trace elements, which provide insights concerning geological provenance, could be investigated using ICP-MS, given that the major elements, namely Ag, were already studied.

Bibliography

[1] Abdi, H., and Williams, L. J. Principal component analysis. *Wiley Interdisciplinary Reviews: Computational Statistics 2*, 4 (July 2010), 433–459.

[2] Alberghina, M. F., Barraco, R., Brai, M., Fontana, D., and Tranchina, L. LIBS and XRF analysis for a stratigraphic study of pictorial multilayer surfaces. *PERIODICO di MINERALOGIA 84*, 3A (June 2015).

[3] Alexandrov, T., and Lasch, P. Segmentation of Confocal Raman Microspectroscopic Imaging Data Using Edge-Preserving Denoising and Clustering. *Anal. Chem. 85*, 12 (June 2013), 5676–5683.

[4] Amato, S. R., et al. Interpreting technical evidence from spectral imaging of paintings by Édouard Manet in the Courtauld Gallery. *X-Ray Spectrometry*.

[5] Aminzadeh, A. Fluorescence bands in the FT-Raman spectra of some calcium minerals. *Spectrochimica Acta Part A: Molecular and Biomolecular Spectroscopy 53*, 5 (May 1997), 693–697.

[6] Antunes, V. *Técnicas e materiais de preparação na pintura portuguesa dos séculos XV e XVI.* PhD thesis, Universidade de Lisboa, 2014.

[7] Antunes, V., et al. Uncover the mantle: rediscovering Gregório Lopes palette and technique with a study on the painting "Mater Misericordiae". *Appl. Phys. A 122*, 11 (Nov. 2016), 965.

[8] Antunes, V., et al. On the origin of Goa Cathedral former altarpiece: Material and technical assessment to the work of Garcia Fernandes, Portuguese painter from 16th century Lisbon workshop. *Microchemical Journal 138* (May 2018), 226–237.

[9] Arrizabalaga, I., et al. Diffuse reflectance FTIR database for the interpretation of the spectra obtained with a handheld device on built heritage materials. *Anal. Methods 7*, 3 (Jan. 2015), 1061–1070.

[10] Bailão, A., Henriques, F., Cabral, M., and Gonçalves, A. Primeiros passos de maturidade a caminho da reintegração cromática diferenciada em pintura de cavalete em Portugal. *Ge-conservación 1* (Aug. 2010).

[11] Baptista Alvares, J. Arte da pintura, symmetria, e perspectiva : Nunes, Philippe, 1767.

[12] Bardelli, F., Barone, G., Crupi, V., Longo, F., Majolino, D., Mazzoleni, P., and Venuti, V. Combined non-destructive XRF and SR-XAS study of archaeological artefacts. *Anal Bioanal Chem 399*, 9 (Mar. 2011), 3147–3153.

[13] Barroqueiro, J. Mestre Do Sardoal. `http://turismo.cm-sardoal.pt/index.php/pt/patrimonio-religioso/mestre-sardoal`. Last accessed on 07-02-2018.

[14] Bell, I. M., Clark, R. J. H., and Gibbs, P. J. Raman spectroscopic library of natural and synthetic pigments (pre- ≈ 1850 AD). *Spectrochimica Acta Part A: Molecular and Biomolecular Spectroscopy 53*, 12 (Oct. 1997), 2159–2179.

[15] Benquerença, M.-J., Mendes, N. F. C., Castellucci, E., Gaspar, V. M. F., and Gil, F. P. S. C. Micro-Raman spectroscopy analysis of 16th century Portuguese Ferreirim Masters oil paintings. *Journal of Raman Spectroscopy 40*, 12, 2135–2143.

[16] Bidarra, A., Coroado, J., and Rocha, F. Gold leaf analysis of three baroque altarpieces from Porto. *ArcheoSciences. Revue d'archéométrie*, 33 (Dec. 2009), 417–421.

[17] Boon, J., Van der Weerd, J., Keune, K., Noble, P., and Wadum, J. Mechanical and chemical changes in Old Master paintings: dissolution, metal soap formation and remineralization processes in lead pigmented ground/intermediate paint layers of 17th century paintings. *13th Triennial Meeting of the ICOM committee for conservation in Rio de Janerio* (Nov. 2015), 401–406.

[18] Bortolotti, M., Lutterotti, L., and Pepponi, G. Combining XRD and XRF analysis in one Rietveld-like fitting. *Powder Diffraction 32*, S1 (Sept. 2017), S225–S230.

[19] Brand, N. W., and Brand, C. J. Performance comparison of portable XRF instruments. *Geochemistry: Exploration, Environment, Analysis 14*, 2 (May 2014), 125–138.

[20] Brion, A., et al. Nacre extract restores the mineralization capacity of subchondral osteoarthritis osteoblasts. *Journal of Structural Biology 192*, 3 (Dec. 2015), 500–509.

[21] Bruker. Introduction to EDS analysis - Reference Manual. `http://emc.missouri.edu/wp-content/uploads/2016/01/Bruker-Introduction-to-EDS-analysis.pdf`. Last accessed on 27-08-2018.

[22] Bruker. XRF Data Differences: Quantitative, Semi-Quantitative, and Qualitative Data. `https://www.bruker.com/products/x-ray-diffraction-and-elemental-analysis/handheld-xrf/xrf-data-primer-quantitative-semi-quantitative-qualitative.html`. Last accessed on 04-09-2018.

[23] Buzgar, N., Buzatu, A., and Sanislav, I. V. The Raman study on certain sulfates. *Analele Stiintifice ale Universitatii Al. I. Cuza 55* (2009), 5–23.

[24] Caggiani, M., Cosentino, A., and Mangone, A. Pigments Checker version 3.0, a handy set for conservation scientists: A free online Raman spectra database. *Microchemical Journal 129* (June 2016), 123–132.

[25] Campos Maia, B., et al. Obras de Grão Vasco e da sua oficina.

[26] Carvalho, M., Manso, M., and Pessanha, S. Os Raios X na Arte e no Património Cultural. *Revista de Ciência Elementar 6* (Mar. 2018).

[27] Casadio, F., Daher, C., and Bellot-Gurlet, L. Raman Spectroscopy of cultural heritage Materials: Overview of Applications and New Frontiers in Instrumentation, Sampling Modalities, and Data Processing. *Top Curr Chem (Z) 374*, 5 (Oct. 2016), 62.

[28] Center for Physics of the University of Coimbra - Equipment. `http://cfisuc.fis.uc.pt/equipment.php`. Last accessed on 27-08-2018.

[29] Cesareo, R. X-Ray Fluorescence Spectrometry. In *Ullmann's Encyclopedia of Industrial Chemistry*. American Cancer Society, 2010.

[30] Correia, A. M., Clark, R. J. H., Ribeiro, M. I. M., and Duarte, M. L. T. S. Pigment study by Raman microscopy of 23 paintings by the Portuguese artist Henrique Pousão (1859–1884). *Journal of Raman Spectroscopy 38*, 11 (Nov. 2007), 1390–1405.

[31] Coxito, A. M. T. Estudo de ligas de ouro por XRF e SEM-EDS. Master's thesis, University of Coimbra, July 2016.

[32] Cruz, A. J. O estudo laboratorial e os materiais do políptico de S. Vicente. *Nuno Gonçalves. Novos Documentos. Estudo da pintura portuguesa do séc. XV* (1994), 41–45.

[33] Cruz, A. J. Pigmentos e corantes das obras de arte em Portugal, no início do século XVII, segundo o tratado de pintura de Filipe Nunes. *Conservar Património*, 6 (2007), 39–51.

[34] Cruz, A. J. A proveniência dos pigmentos utilizados em pintura em Portugal antes da invenção dos tubos de tintas: problemas e perspectivas. Jan. 2013, pp. 297–306.

[35] Cruz, A. J., Eires, E., Dias, L., Desterro, T., and Rego, C. Identification of vivianite, an unusual blue pigment, in a sixteenth century painting and its implications. *Color Research & Application 43*, 2 (2018), 177–183.

[36] Cruz, A. J., and Monteiro, P. Sobre um tratado inédito de pintura da primeira metade do século XVII: o Breve Tratado de Iluminação, composto por um religioso da Ordem de Cristo. In *Os materiais utilizados em pintura e as fontes documentais*. 2012, pp. 147–169.

[37] Cultural Heritage Science Open Source - Red Ochre, K-11574. `https://chsopensource.org/red-ochre-k-11574/`. Last accessed on 23-08-2018.

[38] DGPC -Direção Geral do Património Cultural. `http:/www.patrimoniocultural.gov.pt/en/`. Last accessed on 24-06-2018.

[39] Fitzhugh, E. W. Red Lead and Minium. In *Artists' Pigments, A handbook of their history and characteristics*, vol. 1. National Gallery of Art, Washington, 2012, pp. 109–141.

[40] Fitzhugh, E. W., and Gettens, R. J. Azurite and Blue Verditer. In *Artists' Pigments, A handbook of their history and characteristics*, vol. 2. National Gallery of Art, Washington, 2012, pp. 23–37.

[41] Frahm, E., Doonan, R., and Kilikoglou, V. Handheld Portable X-Ray Fluorescence of Aegean Obsidians. *Archaeometry 56*, 2 (Mar. 2014), 228–260.

[42] Freches, M. d. A. Deposição de Cristo no túmulo : estudo e intervenção de conservação e restauro. Master's thesis, Universidade Católica Portuguesa, Dec. 2016.

[43] Frost, R. L., Fredericks, P. M., and Bartlett, J. R. Fourier transform Raman spectroscopy of kandite clays. *Spectrochimica Acta Part A: Molecular Spectroscopy 49*, 5-6 (May 1993), 667–674.

[44] García-Bucio, M. A., Casanova-González, E., Ruvalcaba-Sil, J. L., Arroyo-Lemus, E., and Mitrani-Viggiano, A. Spectroscopic characterization of sixteenth century panel painting references using Raman, surface-enhanced Raman spectroscopy and helium-Raman system for in situ analysis of Ibero-American Colonial paintings. *Phil. Trans. R. Soc. A 374*, 2082 (Dec. 2016), 20160051.

[45] Gaspar, V. A Pintura Quinhentista do Convento de Santo António de Ferreirim (Ebook). `http://www.valedovarosa.gov.pt/mestres-de-ferreirim-chegam-em-forma-de-e-book/`. Last accessed on 27-08-2018.

[46] Gettens, R. J., Feller, R. L., and Chase, W. T. Vermilion and Cinnabar. In *Artists' Pigments, A handbook of their history and characteristics*, vol. 2. National Gallery of Art, Washington, 2012, pp. 159–173.

[47] Gettens, R. J., and Fitzhugh, E. W. Malachite and Green Verditer. In *Artists' Pigments, A handbook of their history and characteristics*, vol. 2. National Gallery of Art, Washington, 2012, pp. 159–173.

[48] Gettens, R. J., Kuhn, H., and Chase, W. T. Lead White. In *Artists' Pigments, A handbook of their history and characteristics*, vol. 2. National Gallery of Art, Washington, 2012, pp. 67–79.

[49] Ghostly Image of Scottish Queen Found Beneath Painting. `https://news.nationalgeographic.com/2017/10/hidden-painting-mary-queen-scotland-maitland-x-ray-spd`. Last accessed on 06-02-2018.

[50] Gil, M., et al. Material and diagnostic characterization of 17th century mural paintings by spectra-colorimetry and SEM-EDS: An insight look at José de Escovar Workshop at the CONVENT of N^a Sr^a da Saudação (Southern Portugal). *Color Research & Application 39*, 3 (Feb. 2013), 288–306.

[51] Gil, M., et al. José de Escovar at the Chapel of the Souls: Technical and material study of a 1603 panel painting. *Color Research & Application 41*, 3 (Jan. 2016), 252–257.

[52] Giudice, A. L., et al. Multitechnique characterization of lapis lazuli for provenance study. *Anal Bioanal Chem 395*, 7 (Dec. 2009), 2211–2217.

[53] Goldstein, J. I. Electron Beam-Specimen Interaction. In *Practical Scanning Electron Microscopy: Electron and Ion Microprobe Analysis*, J. I. Goldstein and H. Yakowitz, Eds. Springer US, Boston, MA, 1975, pp. 49–94.

[54] Goldstein, J. I., et al. Backscattered Electrons. In *Scanning Electron Microscopy and X-Ray Microanalysis*, 4 ed. Springer-Verlag, New York, 2018.

[55] Goldstein., J. I., et al. Image Defects. In *Scanning Electron Microscopy and X-Ray Microanalysis*, 4 ed. Springer-Verlag, New York, 2018.

[56] Goldstein, J. I., et al. Image Formation. In *Scanning Electron Microscopy and X-Ray Microanalysis*, 4 ed. Springer-Verlag, New York, 2018.

[57] Goldstein, J. I., et al. Scanning Electron Microscopy and Associated Techniques: Overview. In *Scanning Electron Microscopy and X-Ray Microanalysis*, 4 ed. Springer-Verlag, New York, 2018.

[58] Goldstein, J. I., Yakowitz, H., and Newbury, D. E. Introduction. In *Practical Scanning Electron Microscopy: Electron and Ion Microprobe Analysis*, J. I. Goldstein and H. Yakowitz, Eds. Springer US, Boston, MA, 1975, pp. 1–19.

[59] Grieken, R. V., and Markowicz, A. EDS Fluorescence Analysis Using X-ray Tube Excitation. In *Handbook of X-Ray Spectrometry, Second Edition,*. CRC Press, Nov. 2001, pp. 199–236.

[60] Grissom, C. A. Green Earth. In *Artists' Pigments, A handbook of their history and characteristics*, vol. 1. National Gallery of Art, Washington, 2012, pp. 141–169.

[61] Guerra, M. F. An overview on the ancient goldsmith's skill and the circulation of gold in the past: the role of x-ray based techniques. *X-Ray Spectrometry 37*, 4 (July 2008), 317–327.

[62] Guerra, M. F., and Calligaro, T. Gold traces to trace gold. *Journal of Archaeological Science 31*, 9 (Sept. 2004), 1199–1208.

[63] Guilherme, A., Cavaco, A., Pessanha, S., Costa, M., and Carvalho, M. L. Comparison of portable and stationary x-ray fluorescence spectrometers in the study of ancient metallic artefacts. *X-Ray Spectrometry 37*, 4 (July 2008), 444–449.

[64] Hahn, O., Reiche, I., and Stege, H. 7.7 Applications in Arts and Archaeology. In *Handbook of Practical X-Ray Fluorescence Analysis*, B. Beckhoff, B. Kanngießer, N. Langhoff, R. Wedell, and H. Wolff, Eds. Springer, May 2007, pp. 687–700.

[65] Helvaci, Y. Z., et al. Tracking old and new colours: Material study of 16th century mural paintings from Évora Cathedral (Southern Portugal). *Color Research & Application 41*, 3 (Feb. 2016), 276–282.

[66] HERCULES Lab. `http://hercules.uevora.pt`. Last accessed on 24-06-2018.

[67] Hernberg, S. Lead poisoning in a historical perspective. *Am. J. Ind. Med. 38*, 3 (Sept. 2000), 244–254.

[68] Heuser, D., and Walker, D. S. A comparison of elemental analysis techniques requiring no sample preparation: scanning electron microscopy and laser induced breakdown spectroscopy. *J. Anal. At. Spectrom. 19*, 7 (July 2004), 929–931.

[69] Hradil, D., Grygar, T., Hradilová, J., and Bezdička, P. Clay and iron oxide pigments in the history of painting. *Applied Clay Science 22*, 5 (Apr. 2003), 223–236.

[70] Hubbell, J. H., Trehan, P. N., Singh, N., Chand, B., Mehta, D., Garg, M. L., Garg, R. R., Singh, S., and Puri, S. A Review, Bibliography, and Tabulation of K, L, and Higher Atomic Shell X-Ray Fluorescence Yields. *Journal of Physical and Chemical Reference Data 23*, 2 (Mar. 1994), 339–364.

[71] Instituto Português de Conservação e Restauro. Retábulo de Ferreira do Alentejo (ebook). `https://issuu.com/imc-ip/docs/retabulo_ferreira_alentejo`. Last accessed on 24-06-2018.

[72] Kacal, M. R., Han, I., and Akman, F. Measurements of K shell absorption jump factors and jump ratios using EDXRF technique. *Eur. Phys. J. D 69*, 4 (Apr. 2015), 103.

[73] Kalcsits, L. A. Non-destructive Measurement of Calcium and Potassium in Apple and Pear Using Handheld X-ray Fluorescence. *Front Plant Sci 7* (Apr. 2016).

[74] Kuhn, H. Lead-Tin Yellow. In *Artists' Pigments, A handbook of their history and characteristics*, vol. 2. National Gallery of Art, Washington, 2012, pp. 83–98.

[75] Larkin, P. *Infrared and Raman Spectroscopy.* Elsevier, 2011.

[76] Le Gac, A., Seruya, A. I., Lefftz, M., and Alarcão, A. The main altarpiece of the Old Cathedral of Coimbra (Portugal). Characterization of gold alloys used for gilding from 1500 to 1900. *ArcheoSciences. Revue d'archéométrie*, 33 (Dec. 2009), 423–432.

[77] Leusch, V., Brauns, M., and Pernicka, E. Precise and Accurate Analysis of Gold Alloys: Varna, the Earliest Gold of Mankind—A Case Study. In *Recent Advances in Laser Ablation ICP-MS for Archaeology*, Natural Science in Archaeology. Springer Berlin Heidelberg, Berlin, Heidelberg, 2016, pp. 95–113.

[78] Lin, J. Performance of the Thermo Scientific Niton XRF Analyzer: The Effects of Particle Size, Length of Analysis, Water, Organic Matter, and Soil Chemistry. Master's thesis, University of Berkeley, May 2009.

[79] Liss, B., and Stout, S. Materials Characterization for Cultural Heritage: XRF Case Studies in Archaeology and Art. In *Heritage and Archaeology in the Digital Age*, Quantitative Methods in the Humanities and Social Sciences. Springer, Cham, 2017, pp. 49–65.

[80] Madariaga, J. M. Analytical chemistry in the field of cultural heritage. *Anal. Methods 7*, 12 (June 2015), 4848–4876.

[81] Mantler, M. 5.2. Basic Fundamental Parameter Equations. In *Handbook of Practical X-Ray Fluorescence Analysis*, B. Beckhoff, B. Kanngießer, N. Langhoff, R. Wedell, and H. Wolff, Eds. Springer, May 2007, pp. 311–327.

[82] Martins, C. M. B. A mineração do chumbo em época romana. O exemplo das Minas de Braçal e Malhada (Aveiro). *O Arqueólogo Português 1* (2011), 489–504.

[83] Matias, I., et al. João de Ruão sculptures – characterisation through pigment analysis. *ICOM-CC: working group sculpture and polychromy newsletter* (2010), 11–14.

[84] Miguel, C., Barrocas-Dias, C., Ferreira, T., and Candeias, A. The comparative study of four Portuguese sixteenth-century illuminated *manueline* Charters based on spectroscopy and chemometrics analysis. *Appl. Phys. A 123*, 1 (Jan. 2017), 72.

[85] Miliani, C., et al. In situ non-invasive investigation on the painting techniques of early Meissen Stoneware. *Spectrochimica Acta Part A: Molecular and Biomolecular Spectroscopy 73*, 4 (Aug. 2009), 587–592.

[86] Mindat. Charcoal: Charcoal mineral information and data. `https://www.mindat.org/min-40391.html`. Last accessed on 23-08-2018.

[87] Moura, L., Melo, M. J., Casanova, C., and Claro, A. A study on Portuguese manuscript illumination: The Charter of Vila Flor (Flower town), 1512. *Journal of Cultural Heritage 8*, 3 (July 2007), 299–306.

[88] Newbury, D. E. Misidentification of Major Constituents by Automatic Qualitative Energy Dispersive X-ray Microanalysis: A Problem that Threatens the Credibility of the Analytical Community. *Microscopy and Microanalysis 11*, 6 (Dec. 2005), 545–561.

[89] Newbury, D. E. Mistakes Encountered during Automatic Peak Identification in Low Beam Energy X-ray Microanalysis. *Scanning 29*, 4 (July 2007), 137–151.

[90] NIST: X-Ray Mass Attenuation Coefficients - Calcium. `https://physics.nist.gov/PhysRefData/XrayMassCoef/ElemTab/z20.html`. Last accessed on 19-04-2018.

[91] Ospitali, F., Bersani, D., Lonardo, G. D., and Lottici, P. P. 'Green earths': vibrational and elemental characterization of glauconites, celadonites and historical pigments. *Journal of Raman Spectroscopy 39*, 8 (2018), 1066–1073.

[92] Osticioli, I., Mendes, N. F. C., Nevin, A., Gil, F. P. S. C., Becucci, M., and Castellucci, E. Analysis of natural and artificial ultramarine blue pigments using laser induced breakdown and pulsed Raman spectroscopy, statistical analysis and light microscopy. *Spectrochimica Acta Part A: Molecular and Biomolecular Spectroscopy 73*, 3 (Aug. 2009), 525–531.

[93] Pacheco, F. *Arte de la Pintura, su Antigüedad y Grandezas.* Galiano, 1866.

[94] Pasmore, J. Recent Developments in Handheld X-ray Fluorescence (XRF) Instrumentation. In *Fall Conference & Quality Testing Show 2009* (Oct. 2009).

[95] Prati, S., Sciutto, G., Bonacini, I., and Mazzeo, R. New Frontiers in Application of FTIR Microscopy for Characterization of Cultural Heritage Materials. *Top Curr Chem (Z) 374*, 3 (June 2016), 26.

[96] Ravaud, E., et al. Development of a versatile XRF scanner for the elemental imaging of paintworks. *Applied Physics A 122* (Dec. 2016).

[97] Rodrigues, D. Vicente Gil e Manuel Vicente: «Mestres do Sardoal». In *Do Gótico ao Manuelino*, P. Ferreira, Ed., vol. 2 of *História da Arte Portuguesa.* Círculo de Leitores, 1995, pp. 237–240.

[98] RRUFF. Anhydrite R040012 - RRUFF Database: Raman, X-ray, Infrared, and Chemistry. `http://rruff.info/anhydrite/display=default/R040012`. Last accessed on 23-08-2018.

[99] RRUFF. Gypsum R040029 - RRUFF Database: Raman, X-ray, Infrared, and Chemistry. `http://rruff.info/gypsum/display=default/R040029`. Last accessed on 23-08-2018.

[100] Sandu, I. C. A., Sá, M. H. d., and Pereira, M. C. Ancient 'gilded' art objects from European cultural heritage: a review on different scales of characterization. *Surface and Interface Analysis 43*, 8 (jan 2011), 1134–1151.

[101] Santos, H. F. P. P. d. M. D. d. *O pintor Francisco João (Act.1563-1595) : materiais e técnicas na pintura de cavalete em èvora na segunda metade do século XVI.* PhD thesis, Universidade Católica Portuguesa, 2012.

[102] Santos, S. M. d. *Francisco Correia, o mesmo nome para dois pintores maneiristas : estudo artístico e técnico-material das suas obras, documentadas e atribuídas.* PhD thesis, Universidade Católica Portuguesa, May 2015.

[103] Sarala, P., Taivalkoski, A., and Valkama, J. Portable XRF: An advanced onsite analysis method in till geochemical exploration. *Special Paper - Geological Survey of Finland 57* (Feb. 2015), 63–86.

[104] Schreiner, M., Melcher, M., and Uhlir, K. Scanning electron microscopy and energy dispersive analysis: applications in the field of cultural heritage. *Anal Bioanal Chem 387*, 3 (Feb. 2007), 737–747.

[105] Shirakawa, M. A., et al. Climate as the most important factor determining anti-fungal biocide performance in paint films. *Science of The Total Environment 408*, 23 (Nov. 2010), 5878–5886.

[106] Sidhu, B. S., Dhaliwal, A. S., Mann, K. S., and Kahlon, K. S. EDXRF technique: An alternative methodology for measuring LIII subshell absorption edge jump factor and jump ratio of some high Z elements. *Radiation Physics and Chemistry 80*, 6 (June 2011), 688–691.

[107] Smith, G. D., and Clark, R. J. H. The role of H2s in pigment blackening. *Journal of Cultural Heritage 3*, 2 (Apr. 2002), 101–105.

[108] Sousa, M. J., and Cruz, A. J. Materiais e Técnica do Painel Representando a Visitação Executado para o Retábulo da Capela de Santa Isabel (Porto), pelo Pintor Maneirista Diogo Teixeira. *Estudos de Conservação e Restauro 1*, 4 (Jan. 2012).

[109] Sousa, M. J. R. d. S. *A matéria da arte e as suas circunstâncias : estratégias adaptativas do pintor maneirista Diogo Teixeira.* PhD thesis, Universidade Católica Portuguesa, Mar. 2016.

[110] Spring, M., and Grout, R. The blackening of vermilion: An analytical study of the process in paintings. National Gallery Technical Bulletin Vol 23, pp 50–61, 2002.

[111] Streli, C. 7.3. Total-Reflection X-Ray Fluorescence (TXRF) Wafer Analysis. In *Handbook of Practical X-Ray Fluorescence Analysis*, B. Beckhoff, B. Kanngießer, N. Langhoff, R. Wedell, and H. Wolff, Eds. Springer, May 2007, pp. 498–554.

[112] Strydonck, M. V. Radiocarbon Dating. *Top Curr Chem (Z) 374*, 2 (Apr. 2016), 13.

[113] Teagle, D., Ildefonse, B., Blum, P., and the Expedition 335 Scientists. Evaluation of the handheld XRF scanner aboard the JOIDES Resolution by the Expedition 335 geochemists. Supp. Mat., International Ocean Discovery Program (IODP), 2011. Last accessed on 22-07-2018.

[114] Tertian, R., and Claisse, F. *Principles of quantitative X-ray fluorescence analysis.* Heyden, 1982.

[115] TESCAN. Scanning Electron Microscope Vega3 SEM: Instructions For Use, 2011.

[116] Thomsen, V. Basic fundamental parameters in X-ray fluorescence. *Spectroscopy-Springfield 22*, 5 (2007), 46.

[117] Tomasini, E. P., Halac, E. B., Reinoso, M., Liscia, E. J. D., and Maier, M. S. Micro-Raman spectroscopy of carbon-based black pigments. *Journal of Raman Spectroscopy 43*, 11 (Sept. 2012), 1671–1675.

[118] Vai, S., Lari, M., and Caramelli, D. DNA Sequencing in Cultural Heritage. *Top Curr Chem (Z) 374*, 1 (Feb. 2016), 8.

[119] Valadas, S., et al. A multi-analytical study of the fifteenth century mural paintings of the Batalha Monastery (Portugal) in view of their conservation. *Appl. Phys. A 113*, 4 (Dec. 2013), 989–998.

[120] Valadas, S., Freire, R. V., Cardoso, A., Mirão, J., Dias, C. B., Vandenabeele, P., and Candeias, A. On the Use of the Unusual Green Pigment Brochantite (Cu4(SO4)(OH)6) in the 16th-Century Portuguese-Flemish Paintings Attributed to The Master Frei Carlos Workshop. *Microscopy and Microanalysis 21*, 2 (Apr. 2015), 518–525.

[121] Vandenabeele, P., Wehling, B., Moens, L., and Dekeyzer. Pigment investigation of a late-medieval manuscript with total reflection X-ray fluorescence and micro-Raman spectroscopy. *Analyst 124*, 2 (Jan. 1999), 169–172.

[122] Vandenabeele, P., Wehling, B., Moens, L. J., Edwards, H., De Reu, M., and Van Hooydonk, G. Analysis with micro-Raman spectroscopy of natural organic binding media and varnishes used in art. *Analytica Chimica Acta 407*, 1-2 (Feb. 2000), 261–274.

[123] Veiga, A. d. J. d. C. *Estudo arqueométrico de pinturas a óleo sobre cobre dos séculos XVII/XVIII do Museu de Évora.* PhD thesis, University of Évora, 2015.

[124] Wallert, A. Unusual pigments on a Greek marble basin. *Studies in Conservation 40*, 3 (Aug. 1995), 177–188.

[125] XL3 Analyzer User's Guide - Version 7.01. User Guide Version 7.01, Revision C, Thermo Fisher Scientific Niton Analyzers, Nov. 2010.

[126] ZSCHORNACK, G. H. *Handbook of X-Ray Data.* Springer-Verlag, Berlin Heidelberg, 2007.

[127] ZWICKY, C. N., AND LIENEMANN, P. Quantitative or semi-quantitative?–laboratory-based WD-XRF versus portable ED-XRF spectrometer: results obtained from measurements on nickel-base alloys. *X-Ray Spectrometry 33*, 4 (July 2004), 294–300.

Appendix A

Calculated rates and clusters

In this appendix, the Table A.1 corresponds to the rates calculated according to [116], whereas Table A.3 shows the clustered results of the PCA analysis using the data from the Table A.1 and Table A.2 the PCA results using the data given by the PXRF instrument. For the clustering, an Affinity Propagation using the first four principal components was employed.

Table A.1: Rates calculated for a few selected elements. Au and samples containing Au were eliminated.

Samples	R_{Al}	R_{Si}	R_{K}	R_{S}	R_{Ca}	R_{Fe}	R_{Cu}	R_{Hg}	R_{Pb}	R_{Sn}
pxrf-p25-1	1798.29(6343)	10 120.00(101)	263.05(538)	2665.72(5948)	10.85(34)	24.55(58)	121.13(492)	0.00(0)	173.90(354)	0.00(0)
pxrf-p25-2	1761.51(9791)	6980.00(70)	249.41(429)	3000.83(5968)	24.16(34)	35.10(52)	56.93(319)	0.00(0)	130.57(130)	0.00(0)
pxrf-p25-3	1846.76(6853)	11 701.00(117)	239.41(421)	3168.67(6928)	23.57(40)	0.00(0)	71.78(978)	0.00(0)	177.16(414)	267.13(883)
pxrf-p25-4	1575.61(3377)	7895.00(79)	218.67(453)	2307.02(5815)	28.01(26)	58.98(114)	125.24(317)	0.00(0)	209.31(367)	2305.02(4955)
pxrf-p25-6	1513.46(2739)	7630.00(76)	230.44(392)	2073.93(4680)	20.91(19)	74.02(90)	171.54(579)	0.00(0)	204.29(237)	0.00(0)
pxrf-p25-7	1592.28(1842)	8892.00(89)	282.79(1668)	1772.80(4350)	10.11(19)	0.00(0)	103.31(294)	0.00(0)	129.18(217)	0.00(0)
pxrf-p25-8	1716.20(4815)	9871.00(99)	248.42(478)	2294.39(5171)	11.46(33)	87.80(155)	157.71(423)	0.00(0)	226.74(398)	0.00(0)
pxrf-p25-9	1980.46(6954)	7855.00(79)	309.03(669)	3316.02(7956)	14.32(42)	0.00(0)	87.42(509)	0.00(0)	187.11(415)	0.00(0)
pxrf-p25-10	1742.41(5156)	9582.00(96)	274.22(687)	2161.04(4696)	10.97(29)	9.71(27)	77.77(435)	0.00(0)	85.32(195)	0.00(0)
pxrf-p25-11	1569.43(2048)	9596.00(96)	245.05(633)	1485.69(3972)	11.98(18)	11.35(25)	525.88(501)	0.00(0)	103.22(95)	0.00(0)
pxrf-p25-12	1576.39(4970)	7858.00(79)	214.87(266)	2201.21(5135)	25.32(27)	18.41(38)	39.81(341)	0.00(0)	76.40(141)	0.00(0)
pxrf-p25-13	2691.47(3281)	21 557.00(216)	474.26(442)	841.64(1934)	40.75(39)	104.88(256)	2485.85(6226)	0.00(0)	144.67(355)	414.14(1204)
pxrf-p25-14	1441.26(3292)	5633.00(56)	243.10(837)	1205.70(2652)	20.92(17)	28.62(94)	217.54(617)	1989.18(5168)	108.85(283)	0.00(0)
pxrf-p25-15	1527.69(1628)	7351.00(74)	217.77(413)	2017.99(4944)	18.70(21)	14.72(37)	403.41(804)	0.00(0)	168.66(311)	0.00(0)
pxrf-p25-16	1611.39(3353)	12 967.00(130)	195.31(301)	854.78(1871)	19.05(16)	27.57(46)	738.28(1114)	0.00(0)	215.17(347)	0.00(0)
pxrf-p25-17	2307.81(2891)	13 520.00(135)	0.00(0)	2901.90(6606)	13.66(36)	26.06(33)	126.96(370)	0.00(0)	127.19(139)	1666.13(2494)
pxrf-p25-18	1834.02(3084)	8248.00(82)	275.38(1141)	2488.76(5993)	11.84(34)	285.42(702)	142.68(484)	0.00(0)	124.95(311)	0.00(0)
pxrf-p25-19	1128.64(2142)	11 378.00(114)	143.44(886)	856.48(2358)	6.42(15)	209.47(224)	171.29(516)	0.00(0)	188.19(199)	1524.23(3088)
pxrf-p25-20	2167.57(5878)	8854.00(89)	491.67(1882)	2744.34(5450)	13.54(38)	211.40(275)	113.83(873)	57.96(124)	228.79(308)	626.64(1545)
pxrf-p25-22	2544.37(16956)	13 591.00(136)	328.55(532)	4271.02(8876)	12.46(50)	0.00(0)	186.03(660)	0.00(0)	177.94(178)	0.00(0)
pxrf-p25-23	1923.30(6335)	9953.00(100)	344.35(1270)	2826.19(5603)	13.99(40)	47.96(60)	63.77(586)	47.01(78)	117.57(121)	0.00(0)
pxrf-p25-24	1900.52(4051)	8753.00(88)	308.95(882)	3229.48(7318)	14.66(47)	0.00(0)	0.00(0)	52.04(129)	183.58(320)	0.00(0)

Continues on next page

Table A.1 (continued)

Samples	R_{Al}	R_{Si}	R_{K}	R_{S}	R_{Ca}	R_{Fe}	R_{Cu}	R_{Hg}	R_{Pb}	R_{Sn}
pxrf-p25-25	1725.25(5462)	5306.00(53)	307.65(481)	2367.94(4795)	9.74(42)	18.64(92)	75.51(656)	1379.68(7076)	134.52(649)	0.00(0)
pxrf-p25-26	1710.83(6028)	9711.00(97)	298.97(574)	2530.20(5552)	9.90(38)	40.17(78)	3484.17(6183)	86.87(275)	122.49(197)	0.00(0)
pxrf-p25-27	1502.97(3574)	7820.00(78)	181.73(402)	1470.57(3088)	11.74(17)	25.60(131)	9323.21(31949)	0.00(0)	78.67(262)	0.00(0)
pxrf-p25-29	1473.30(4009)	9199.00(92)	220.84(320)	1491.35(3529)	9.61(19)	21.61(99)	2103.49(9283)	0.00(0)	86.38(378)	0.00(0)
pxrf-p25-32	2098.15(3982)	13 148.00(131)	0.00(0)	1423.80(3179)	15.80(12)	25.02(67)	2540.46(4529)	0.00(0)	136.91(238)	4408.50(9042)
pxrf-p25-33	1918.98(4607)	8979.00(90)	372.00(1965)	1655.19(3894)	13.44(21)	30.41(133)	225.96(938)	0.00(0)	152.48(630)	287.32(1412)
pxrf-p25-34	1825.10(2178)	13 049.00(130)	0.00(0)	1527.01(3690)	12.83(17)	151.71(173)	2546.36(2926)	0.00(0)	120.70(131)	2544.12(3941)
pxrf-p25-36	1937.36(7323)	8103.00(81)	628.77(1677)	2691.55(5774)	12.34(35)	88.47(111)	60.08(283)	87.55(197)	89.74(111)	549.29(1095)
pxrf-p25-39	1649.16(4939)	10 609.00(106)	245.31(744)	1965.29(4928)	11.02(27)	0.00(0)	1199.51(1726)	0.00(0)	201.00(301)	0.00(0)
pxrf-p25-40	1387.91(3299)	9046.00(90)	188.04(293)	1191.17(2457)	13.49(9)	58.70(101)	13 277.58(15455)	0.00(0)	60.57(57)	0.00(0)
pxrf-p25-42	2564.54(2668)	16 864.00(169)	0.00(0)	2896.39(6408)	16.96(26)	0.00(0)	0.00(0)	0.00(0)	145.41(292)	7062.62(16324)
pxrf-p25-43	1911.06(7189)	10 163.00(102)	270.42(581)	2477.79(5880)	12.06(34)	19.29(54)	2793.22(6512)	0.00(0)	165.33(386)	0.00(0)
pxrf-p25-44	1930.74(7009)	9841.00(98)	269.21(530)	3019.68(6863)	11.25(36)	0.00(0)	119.07(607)	0.00(0)	177.56(306)	0.00(0)
pxrf-p25-48	1295.21(1370)	8950.00(90)	187.13(256)	808.43(1474)	11.92(8)	39.69(120)	9186.12(27532)	0.00(0)	62.21(181)	0.00(0)
pxrf-p25-49	2519.38(2660)	15 804.00(158)	0.00(0)	3117.52(6453)	15.74(36)	0.00(0)	367.95(1429)	0.00(0)	131.07(502)	6018.34(23776)
pxrf-p25-50	1456.89(4364)	5022.00(50)	266.92(326)	1401.49(3355)	14.48(25)	10.91(35)	31.84(97)	2001.54(4164)	42.86(94)	0.00(0)
pxrf-p25-51	1681.01(4897)	8896.00(89)	361.39(1871)	2120.58(4473)	15.85(28)	13.69(47)	475.49(1163)	151.78(388)	102.51(252)	233.35(1921)
pxrf-p25-52	2221.84(2292)	12 449.00(124)	0.00(0)	2486.92(5779)	14.02(27)	28.76(128)	2663.63(11707)	0.00(0)	151.49(666)	1046.61(4978)
pxrf-p25-53	1533.92(1650)	7138.00(71)	245.82(267)	1743.00(3854)	13.44(19)	24.27(89)	4270.63(15629)	0.00(0)	98.90(357)	0.00(0)
pxrf-p25-55	2107.97(2255)	11 027.00(110)	0.00(0)	2305.70(5125)	16.51(28)	23.09(23)	118.34(565)	0.00(0)	135.09(120)	7438.43(9816)
pxrf-p25-56	1850.91(3744)	8885.00(89)	292.90(414)	1989.66(4538)	14.33(20)	30.59(30)	1639.63(1279)	0.00(0)	137.26(125)	0.00(0)
pxrf-p25-58	1486.62(1985)	10 349.00(103)	208.35(233)	1165.55(2543)	14.55(9)	23.77(46)	4293.74(6169)	284.62(565)	60.82(83)	0.00(0)

Continues on next page

Table A.1 (continued)

Samples	R_{Al}	R_{Si}	R_{K}	R_{S}	R_{Ca}	R_{Fe}	R_{Cu}	R_{Hg}	R_{Pb}	R_{Sn}
pxrf-p25-59	1948.29(7677)	6755.00(68)	283.20(447)	3226.10(7360)	14.51(48)	0.00(0)	299.49(544)	0.00(0)	171.23(270)	0.00(0)
pxrf-p25-60	1829.27(5279)	8730.00(87)	314.28(747)	2255.76(4932)	12.71(29)	20.62(45)	189.87(429)	0.00(0)	225.56(376)	0.00(0)
pxrf-p26-1	1503.94(11410)	3177.00(32)	251.18(485)	1586.91(3947)	8.93(28)	11.93(22)	554.53(663)	1280.62(2271)	42.56(47)	0.00(0)
pxrf-p26-2	1656.31(5068)	8056.00(81)	296.05(458)	2054.31(5269)	8.85(37)	22.53(78)	39.16(160)	1024.16(3716)	63.01(208)	0.00(0)
pxrf-p26-3	1674.20(3724)	8516.00(85)	412.98(498)	1588.23(3967)	9.84(20)	15.20(27)	62.12(68)	0.00(0)	55.48(37)	0.00(0)
pxrf-p26-3a	2224.52(5078)	9772.00(98)	527.72(968)	0.00(0)	9.40(15)	19.82(29)	108.38(103)	0.00(0)	52.12(51)	0.00(0)
pxrf-p26-4	1391.12(7952)	4982.00(50)	336.27(557)	1286.45(3064)	9.22(23)	23.47(46)	34.14(64)	612.99(1280)	38.36(57)	0.00(0)
pxrf-p26-5	1840.26(9310)	8387.00(84)	310.04(436)	1823.29(3769)	8.59(24)	13.67(63)	42.71(248)	2066.34(7299)	88.55(313)	0.00(0)
pxrf-p26-6	1927.66(9324)	5089.00(51)	375.30(762)	1764.48(4428)	13.51(32)	12.96(27)	21.57(48)	1412.86(3458)	29.47(61)	0.00(0)
pxrf-p26-7	1910.11(8439)	12 188.00(122)	514.91(780)	1600.57(3493)	8.93(26)	11.72(25)	75.50(190)	516.74(1227)	69.31(97)	0.00(0)
pxrf-p26-7a	1886.64(3079)	6473.00(65)	319.32(511)	0.00(0)	12.59(14)	48.20(52)	100.99(162)	1341.30(2092)	114.65(127)	0.00(0)
pxrf-p26-8	1424.22(3639)	10 939.00(109)	162.20(404)	687.73(1559)	11.12(9)	12.78(48)	1811.74(3931)	0.00(0)	37.00(78)	0.00(0)
pxrf-p26-9	1311.44(1316)	6493.00(65)	161.89(328)	1580.76(3212)	7.70(22)	18.53(78)	4909.77(18225)	0.00(0)	53.63(195)	0.00(0)
pxrf-p26-10	1614.21(4052)	8544.00(85)	242.14(341)	2144.45(4153)	7.71(32)	15.39(48)	2322.51(3063)	0.00(0)	120.70(160)	0.00(0)
pxrf-p26-11	1877.07(6602)	14 232.00(142)	306.21(440)	2988.14(5921)	8.26(38)	0.00(0)	1035.97(2050)	0.00(0)	98.81(198)	0.00(0)
pxrf-p26-12	1590.27(1780)	7343.00(73)	182.66(391)	2267.75(4804)	6.97(25)	10.83(46)	3016.14(6048)	0.00(0)	85.20(158)	0.00(0)
pxrf-p26-14	2054.80(3165)	15 843.00(158)	0.00(0)	2679.61(5799)	10.74(34)	0.00(0)	257.69(529)	0.00(0)	149.47(226)	2962.67(5052)
pxrf-p26-15	1554.36(1947)	8147.00(81)	242.83(413)	2244.20(4779)	6.89(29)	19.45(51)	4401.44(10258)	0.00(0)	110.16(248)	0.00(0)
pxrf-p26-16	1308.57(1588)	6897.00(69)	205.41(287)	1579.70(3783)	6.41(17)	13.10(58)	2739.23(6559)	0.00(0)	74.69(170)	0.00(0)
pxrf-p26-17	1258.17(2086)	6856.00(69)	159.95(216)	1499.29(3659)	7.70(17)	15.80(47)	9609.32(26109)	0.00(0)	80.31(209)	0.00(0)
pxrf-p26-18	1713.77(5394)	11 694.00(117)	208.86(401)	2505.84(5721)	6.44(29)	0.00(0)	1706.22(5769)	0.00(0)	123.75(418)	0.00(0)
pxrf-p26-19	1349.51(1295)	7113.00(71)	169.53(298)	1434.16(2829)	6.51(16)	11.99(43)	2777.57(4053)	0.00(0)	59.85(72)	0.00(0)

Continues on next page

Table A.1 (continued)

Samples	R_{Al}	R_{Si}	R_{K}	R_{S}	R_{Ca}	R_{Fe}	R_{Cu}	R_{Hg}	R_{Pb}	R_{Sn}
pxrf-p26-20	1323.78(1673)	7802.00(78)	216.32(372)	1343.14(2866)	6.57(15)	14.28(41)	4223.88(10132)	0.00(0)	103.43(239)	0.00(0)
pxrf-p26-21	1409.19(4037)	6636.00(66)	223.38(276)	1462.69(3378)	8.00(20)	14.00(75)	3049.47(14460)	0.00(0)	81.39(383)	0.00(0)
pxrf-p26-22	1484.21(4876)	8236.00(82)	179.88(304)	2088.11(4895)	8.14(24)	15.60(51)	2789.21(3547)	0.00(0)	131.00(153)	0.00(0)
pxrf-p26-22a	1798.53(2175)	7047.00(70)	203.57(327)	0.00(0)	7.49(13)	36.73(87)	4794.29(5632)	175.65(241)	140.51(113)	0.00(0)
pxrf-p26-23	1722.30(5839)	8977.00(90)	218.44(443)	2491.67(5905)	7.61(31)	0.00(0)	1285.82(1902)	0.00(0)	119.33(163)	0.00(0)
pxrf-p26-24	1589.68(3122)	10 860.00(109)	203.99(587)	2353.82(5040)	9.24(31)	17.95(38)	705.53(816)	37.01(102)	119.10(142)	0.00(0)
pxrf-p26-25	1897.65(7033)	12 763.00(128)	231.76(358)	3255.14(6962)	8.43(38)	16.36(31)	406.23(580)	120.48(188)	130.26(194)	0.00(0)
pxrf-p26-26	1667.47(2656)	6631.00(66)	264.16(550)	2625.47(5976)	8.38(34)	13.10(39)	437.49(394)	36.80(54)	144.89(139)	0.00(0)
pxrf-p26-27	2092.94(13616)	20 123.00(201)	265.75(622)	3629.19(7904)	8.64(32)	0.00(0)	0.00(0)	0.00(0)	249.40(470)	0.00(0)
pxrf-p26-28	2039.21(7071)	9017.00(90)	270.23(439)	3125.55(7175)	6.95(28)	0.00(0)	202.55(343)	0.00(0)	135.54(215)	0.00(0)
pxrf-p26-29	1688.29(3502)	7319.00(73)	185.24(278)	2714.58(6540)	7.04(26)	0.00(0)	0.00(0)	0.00(0)	196.44(344)	0.00(0)
pxrf-p26-30	1997.67(7492)	22 392.00(224)	275.00(549)	3356.76(7242)	7.78(30)	0.00(0)	68.92(462)	0.00(0)	132.76(172)	0.00(0)
pxrf-p26-31	2103.36(8207)	16 928.00(169)	265.34(675)	3721.51(8205)	8.99(45)	0.00(0)	48.01(249)	20.51(74)	99.63(230)	0.00(0)
pxrf-p26-32	1498.35(1673)	9389.00(94)	221.76(468)	1561.64(4097)	15.05(18)	25.16(90)	1321.14(4055)	0.00(0)	64.85(197)	0.00(0)
pxrf-p26-32a	1936.64(2466)	6228.00(62)	246.10(489)	0.00(0)	11.93(13)	21.84(38)	1283.35(1943)	0.00(0)	69.61(91)	0.00(0)
pxrf-p26-33	1637.98(3699)	7430.00(74)	301.26(676)	2040.48(4673)	12.30(26)	84.54(160)	329.53(601)	0.00(0)	86.87(155)	0.00(0)
pxrf-p26-34	1770.84(2143)	8724.00(87)	605.04(1273)	2039.70(4329)	9.86(25)	105.28(136)	52.46(246)	0.00(0)	75.15(97)	571.61(1163)
pxrf-p26-35	1667.25(5587)	9744.00(97)	270.70(504)	2580.99(5958)	12.74(38)	24.31(47)	243.35(282)	119.11(215)	72.75(86)	0.00(0)
pxrf-p26-36	1699.50(8787)	10 270.00(103)	327.00(773)	2341.17(5161)	12.58(37)	83.55(125)	54.12(250)	26.09(69)	45.55(72)	0.00(0)
pxrf-p26-37	1146.09(2872)	6831.00(68)	173.04(296)	1238.31(2793)	10.46(19)	76.17(189)	34.31(225)	93.50(365)	33.10(82)	0.00(0)
pxrf-p26-38	2379.36(2688)	20 802.00(208)	0.00(0)	3245.62(6679)	12.17(27)	0.00(0)	71.02(585)	0.00(0)	127.07(165)	4495.44(7282)
pxrf-p26-39	1789.17(3522)	3803.00(38)	306.93(577)	3139.21(7087)	8.50(39)	0.00(0)	0.00(0)	0.00(0)	119.76(369)	119.58(1120)

Continues on next page

Table A.1 (continued)

Samples	R_{Al}	R_{Si}	R_{K}	R_{S}	R_{Ca}	R_{Fe}	R_{Cu}	R_{Hg}	R_{Pb}	R_{Sn}
pxrf-p26-40	1585.88(2556)	8993.00(90)	254.35(499)	2605.54(5958)	11.02(31)	16.82(59)	45.07(440)	89.47(381)	73.98(200)	0.00(0)
pxrf-p26-41	2076.06(12852)	9246.00(92)	273.55(739)	3341.66(7631)	11.56(52)	10.66(38)	93.02(575)	106.22(502)	100.83(256)	0.00(0)
pxrf-p26-42	2301.83(14567)	10 065.00(101)	308.14(1112)	3966.99(8452)	15.20(50)	10.41(26)	0.00(0)	131.22(343)	58.64(143)	0.00(0)
pxrf-p26-43a	2490.03(4611)	7504.00(75)	225.49(332)	0.00(0)	6.58(19)	0.00(0)	1056.68(3276)	0.00(0)	97.92(297)	0.00(0)
pxrf-p27-1	1380.36(1780)	11 358.00(114)	163.34(486)	455.08(1195)	7.31(8)	37.33(65)	1351.54(2242)	0.00(0)	72.93(99)	0.00(0)
pxrf-p27-2	1632.79(5153)	9584.00(96)	273.24(506)	2648.68(6221)	7.23(27)	0.00(0)	132.34(707)	400.73(2017)	163.34(809)	0.00(0)
pxrf-p27-3	1495.87(2011)	11 603.00(116)	230.79(452)	1885.17(4466)	8.55(22)	21.57(40)	53.28(438)	0.00(0)	116.24(185)	0.00(0)
pxrf-p27-4	1608.18(4915)	11 265.00(113)	357.65(555)	2042.55(4433)	13.00(28)	23.95(37)	24.14(125)	0.00(0)	24.83(22)	0.00(0)
pxrf-p27-5	1607.84(3931)	11 566.00(116)	207.90(396)	2470.52(6123)	8.32(32)	19.21(90)	82.87(570)	0.00(0)	158.72(625)	0.00(0)
pxrf-p27-6	1162.54(1774)	8016.00(80)	181.67(366)	1129.17(2665)	5.77(12)	24.41(45)	3236.00(5978)	0.00(0)	107.79(182)	0.00(0)
pxrf-p27-7	1946.24(3905)	11 669.00(117)	263.04(712)	3382.30(7007)	7.68(30)	18.39(41)	255.70(367)	0.00(0)	161.96(240)	0.00(0)
pxrf-p27-8	1408.11(2170)	8813.00(88)	177.18(496)	1093.23(2258)	12.56(10)	16.23(76)	1502.03(6611)	0.00(0)	38.95(168)	0.00(0)
pxrf-p27-9	1523.71(5646)	6920.00(69)	215.29(486)	2373.06(5393)	7.95(32)	75.76(284)	60.66(314)	0.00(0)	63.87(240)	0.00(0)
pxrf-p27-10	1724.06(1949)	8299.00(83)	302.28(440)	2469.75(4967)	8.26(29)	21.24(90)	367.59(1508)	0.00(0)	100.64(409)	0.00(0)
pxrf-p27-11	2013.97(10677)	8419.00(84)	376.14(585)	2465.01(5826)	9.47(36)	38.16(61)	59.22(130)	0.00(0)	45.64(65)	0.00(0)
pxrf-p27-12	1458.56(4315)	6912.00(69)	249.90(429)	1709.68(3728)	7.26(21)	25.44(59)	1894.82(1977)	0.00(0)	66.16(59)	0.00(0)
pxrf-p27-13	1719.53(2561)	8638.00(86)	249.33(395)	2353.07(5272)	8.15(28)	12.66(23)	227.55(410)	0.00(0)	101.68(154)	0.00(0)
pxrf-p27-14	1776.73(5189)	8401.00(84)	285.15(536)	2894.27(6491)	8.21(35)	11.57(22)	0.00(0)	0.00(0)	114.95(116)	0.00(0)
pxrf-p27-15	1914.45(3006)	8739.00(87)	247.55(582)	3373.86(6951)	8.31(39)	0.00(0)	498.13(1500)	0.00(0)	173.47(514)	0.00(0)
pxrf-p27-16	1277.05(1937)	8206.00(82)	190.31(332)	1484.78(3766)	8.16(24)	59.19(82)	54.42(156)	82.85(136)	48.37(62)	0.00(0)
pxrf-p27-17	1608.34(2489)	10 636.00(106)	258.97(416)	2570.93(5909)	7.73(34)	14.02(48)	1164.81(2428)	0.00(0)	158.03(334)	0.00(0)
pxrf-p27-18	1874.50(3003)	14 790.00(148)	0.00(0)	1531.14(3235)	10.38(17)	16.10(43)	880.38(905)	0.00(0)	57.15(55)	790.68(1149)

Continues on next page

Table A.1 (continued)

Samples	R_{Al}	R_{Si}	R_{K}	R_{S}	R_{Ca}	R_{Fe}	R_{Cu}	R_{Hg}	R_{Pb}	R_{Sn}
pxrf-p27-19	1415.33(2464)	9093.00(91)	517.67(1229)	1839.06(4348)	8.75(36)	91.16(75)	143.86(369)	42.47(87)	178.67(148)	3814.09(5732)
pxrf-p27-20	1805.89(3493)	6809.00(68)	274.44(625)	2995.67(7611)	8.64(35)	0.00(0)	152.47(709)	0.00(0)	186.70(248)	0.00(0)
pxrf-p27-21	2241.10(9906)	9487.00(95)	334.55(717)	3917.29(8717)	9.81(47)	0.00(0)	82.96(732)	0.00(0)	145.15(147)	0.00(0)
pxrf-p27-22	2200.47(15481)	5323.00(53)	299.65(760)	3252.74(6911)	10.18(61)	0.00(0)	62.00(682)	717.15(1511)	125.38(210)	0.00(0)
pxrf-p27-23	1897.13(6255)	7469.00(75)	300.04(467)	3215.86(7249)	9.20(41)	0.00(0)	126.03(656)	0.00(0)	166.53(664)	0.00(0)
pxrf-p27-24	1638.86(3749)	7131.00(71)	313.82(337)	1847.32(4439)	16.78(19)	71.50(127)	54.63(96)	0.00(0)	30.17(50)	0.00(0)
pxrf-p27-25	1851.26(2251)	11 026.00(110)	0.00(0)	1675.83(4145)	13.81(23)	25.26(78)	1559.79(4515)	22.84(85)	64.44(182)	565.19(1732)
pxrf-p27-26	1789.97(9641)	6784.00(68)	269.88(413)	2431.72(5571)	23.97(29)	104.44(172)	29.61(92)	13.35(23)	27.00(43)	0.00(0)
pxrf-p27-27	2058.25(7479)	7864.00(79)	295.24(469)	3326.54(6928)	10.75(42)	45.18(113)	61.53(389)	0.00(0)	97.53(226)	0.00(0)
pxrf-p27-28	1749.62(5090)	9450.00(95)	299.82(620)	2586.91(5472)	10.50(34)	112.07(382)	65.51(259)	31.71(118)	60.74(207)	0.00(0)
pxrf-p27-29	1997.83(13499)	5609.00(56)	285.87(764)	3011.62(6660)	9.36(41)	13.58(29)	39.34(277)	385.68(781)	60.01(116)	0.00(0)
pxrf-p27-30	1884.23(11371)	7049.00(70)	278.96(471)	2942.96(6463)	24.48(41)	37.04(51)	20.71(55)	49.28(126)	32.33(24)	0.00(0)
pxrf-p27-33	2395.39(9591)	20 836.00(208)	299.60(712)	4199.77(8696)	8.56(37)	0.00(0)	0.00(0)	0.00(0)	211.17(374)	0.00(0)
pxrf-p27-34	2079.58(12819)	4628.00(46)	296.57(724)	3165.59(7672)	8.79(41)	14.88(79)	115.07(693)	783.26(3109)	123.60(495)	0.00(0)
pxrf-p27-35	1098.71(1220)	7406.00(74)	121.24(209)	995.63(2120)	6.51(14)	36.80(114)	10 688.50(17715)	0.00(0)	54.25(76)	0.00(0)
pxrf-p27-36	2059.43(7544)	6880.00(69)	273.03(634)	3410.69(6987)	8.38(29)	0.00(0)	1490.59(2841)	0.00(0)	188.66(369)	0.00(0)
pxrf-p27-39	1894.89(6790)	14 627.00(146)	290.04(515)	3373.40(7161)	7.71(31)	0.00(0)	56.98(295)	291.58(707)	127.00(311)	0.00(0)
pxrf-p27-40	1953.05(7500)	11 400.00(114)	362.61(807)	3690.49(7459)	8.56(35)	11.52(27)	0.00(0)	87.44(214)	79.87(111)	0.00(0)
pxrf-p27-43	2257.61(9524)	22 327.00(223)	313.15(650)	3977.01(8818)	8.36(34)	0.00(0)	0.00(0)	109.05(213)	124.69(155)	0.00(0)
pxrf-p27-44	2133.53(14056)	18 496.00(185)	300.25(441)	3811.10(7846)	8.56(32)	0.00(0)	0.00(0)	527.65(991)	160.84(304)	0.00(0)
pxrf-p27-45	2071.49(8533)	15 955.00(160)	283.17(606)	3550.47(7162)	8.10(30)	0.00(0)	0.00(0)	53.77(117)	131.90(127)	0.00(0)
pxrf-p27-46	2189.61(14693)	6689.00(67)	339.32(574)	3357.86(7834)	8.81(44)	13.75(50)	0.00(0)	319.45(1120)	68.46(231)	0.00(0)

Continues on next page

Table A.1 (continued)

Samples	R_{Al}	R_{Si}	R_{K}	R_{S}	R_{Ca}	R_{Fe}	R_{Cu}	R_{Hg}	R_{Pb}	R_{Sn}
pxrf-p27-47	1975.33(7950)	11 175.00(112)	330.17(672)	3634.90(7218)	10.44(45)	18.72(40)	0.00(0)	39.41(101)	81.56(127)	0.00(0)
pxrf-p27-50	2157.79(11120)	7959.00(80)	289.81(419)	2689.46(5938)	8.49(36)	37.68(92)	111.73(776)	1019.65(1088)	219.42(220)	0.00(0)
pxrf-p27-51	2000.45(7131)	6516.00(65)	283.77(506)	1712.59(3829)	10.24(21)	18.62(109)	153.60(762)	0.00(0)	240.58(947)	0.00(0)
pxrf-p27-52	2505.88(14654)	11 746.00(117)	328.56(902)	4397.74(9211)	10.97(54)	0.00(0)	0.00(0)	0.00(0)	181.85(250)	0.00(0)
pxrf-p27-53	2170.36(6668)	8238.00(82)	284.68(597)	3501.65(7451)	9.74(44)	0.00(0)	124.52(748)	0.00(0)	137.57(453)	0.00(0)
pxrf-p27-54	2141.63(6330)	10 669.00(107)	641.80(3155)	2745.33(5858)	14.62(40)	20.01(72)	0.00(0)	0.00(0)	90.56(318)	1504.95(5631)
pxrf-p27-55	2056.77(6373)	8856.00(89)	580.72(1432)	2421.66(5035)	9.37(35)	34.78(80)	78.09(340)	1263.58(3054)	102.02(203)	772.37(1793)
pxrf-p27-56	1868.80(2461)	8911.00(89)	450.30(2244)	2630.15(5688)	9.05(41)	68.34(65)	94.56(470)	0.00(0)	99.27(95)	0.00(0)
pxrf-p27-57	2105.33(2332)	16 126.00(161)	491.15(2989)	2834.70(6821)	10.02(36)	45.46(97)	125.07(592)	0.00(0)	149.91(309)	1596.57(3956)
pxrf-p90-1	2271.50(3955)	11 613.00(116)	270.42(661)	3533.50(8610)	13.32(41)	0.00(0)	94.36(906)	0.00(0)	209.83(390)	195.85(434)
pxrf-p90-3	1617.27(7060)	4807.00(48)	185.57(260)	1516.07(3661)	33.91(36)	153.97(226)	490.82(970)	30.30(67)	110.51(163)	159.21(517)
pxrf-p90-4	2593.83(16531)	9632.00(96)	329.77(785)	4360.53(9883)	13.50(51)	0.00(0)	136.11(1041)	57.69(151)	264.50(590)	0.00(0)
pxrf-p90-5	1507.82(4851)	7138.00(71)	208.43(372)	1790.63(3840)	15.53(25)	57.74(78)	4052.18(5335)	139.99(167)	136.59(153)	0.00(0)
pxrf-p90-6	1680.48(10565)	9599.00(96)	287.45(567)	2616.57(6189)	16.39(46)	31.35(46)	275.25(250)	1551.48(2295)	145.64(134)	0.00(0)
pxrf-p90-7	2239.82(8546)	8966.00(90)	309.45(559)	3823.28(7918)	12.20(49)	21.09(31)	182.18(158)	497.81(672)	161.68(118)	0.00(0)
pxrf-p90-8	2437.88(6577)	13 255.00(133)	373.31(601)	4172.64(9024)	13.93(66)	0.00(0)	247.10(343)	0.00(0)	185.55(218)	0.00(0)
pxrf-p90-12	1737.44(9527)	6475.00(65)	201.17(295)	1972.18(3958)	12.13(25)	17.00(104)	3912.33(10783)	0.00(0)	134.92(365)	0.00(0)
pxrf-p90-15	2449.50(6945)	9750.00(97)	420.99(644)	4434.71(9938)	13.21(55)	0.00(0)	98.07(998)	0.00(0)	168.83(565)	0.00(0)
pxrf-p90-16	1408.63(7136)	20 625.00(206)	352.83(425)	1438.02(3291)	13.55(16)	14.95(26)	738.23(799)	0.00(0)	167.27(182)	0.00(0)
pxrf-p90-17	1317.91(3298)	9564.00(96)	190.00(293)	1267.56(2455)	11.02(12)	21.74(70)	6794.52(8768)	0.00(0)	70.18(79)	0.00(0)
pxrf-p90-18	1966.83(9076)	10 336.00(103)	460.67(2442)	1970.05(4424)	15.75(38)	14.66(54)	163.02(435)	350.72(861)	79.64(176)	194.48(814)
pxrf-p90-19	2447.51(13851)	7649.00(76)	389.67(587)	4015.18(8650)	14.94(50)	0.00(0)	232.51(362)	0.00(0)	155.93(145)	183.67(594)

Continues on next page

Table A.1 (continued)

Samples	R_{Al}	R_{Si}	R_{K}	R_{S}	R_{Ca}	R_{Fe}	R_{Cu}	R_{Hg}	R_{Pb}	R_{Sn}
pxrf-p90-20	2015.56(11789)	7616.00(76)	237.84(447)	2894.36(6433)	15.30(31)	0.00(0)	183.44(369)	0.00(0)	130.46(144)	209.17(407)
pxrf-p90-21	1911.44(10554)	8804.00(88)	295.98(342)	2680.56(5479)	11.77(38)	15.29(61)	1901.86(6153)	0.00(0)	144.65(468)	0.00(0)
pxrf-p90-22	1874.04(4638)	9278.00(93)	285.34(486)	2756.53(5487)	12.41(42)	14.69(27)	1991.30(2732)	0.00(0)	134.59(188)	0.00(0)
pxrf-p90-22a	2579.11(15604)	7431.00(74)	359.24(1066)	4501.56(10256)	13.73(54)	0.00(0)	151.76(1578)	0.00(0)	269.22(1014)	0.00(0)
pxrf-p90-23	2038.38(11968)	6942.00(69)	285.90(811)	3207.10(7373)	13.12(39)	14.19(17)	291.10(308)	0.00(0)	148.27(113)	305.16(616)
pxrf-p90-24	1960.22(9925)	8611.00(86)	260.30(357)	2490.92(5184)	13.15(34)	16.53(38)	3222.48(6295)	0.00(0)	140.54(271)	1014.92(2193)
pxrf-p90-25	1875.37(5332)	7668.00(77)	288.75(339)	2703.35(5798)	15.06(37)	28.96(71)	7632.15(12337)	0.00(0)	145.31(206)	0.00(0)
pxrf-p90-26	1503.20(2372)	8262.00(83)	183.11(483)	547.31(955)	19.81(21)	62.27(142)	16 004.40(29042)	0.00(0)	36.90(61)	0.00(0)
pxrf-p90-27	2253.63(7910)	12 572.00(126)	181.21(494)	2693.13(5734)	23.65(26)	14.36(34)	366.01(669)	0.00(0)	56.92(108)	0.00(0)
pxrf-p90-28	1942.67(11345)	9091.00(91)	258.13(520)	2783.87(6306)	15.15(40)	15.99(54)	1937.42(5505)	0.00(0)	142.50(401)	0.00(0)

Table A.2: Clusters obtained using relative concentrations given by the PXRF instrument.

# cluster	# samples	Samples in cluster
# 1	2	pxrf-p90-3, pxrf-p25-18
# 2	12	pxrf-p90-28, pxrf-p90-23, pxrf-p90-22, pxrf-p90-21, pxrf-p90-19, pxrf-p90-12, pxrf-p25-60, pxrf-p25-53, pxrf-p25-52, pxrf-p25-43, pxrf-p25-32, pxrf-p25-26
# 3	1	pxrf-p90-26
# 4	2	pxrf-p90-25, pxrf-p90-24
# 5	1	pxrf-p90-16
# 6	3	pxrf-p26-7a, pxrf-p26-6, pxrf-p25-50
# 7	6	pxrf-p26-7, pxrf-p26-3a, pxrf-p26-3, pxrf-p27-54, pxrf-p27-4, pxrf-p27-11

Continues on next page

Table A.2 (continued)

# cluster	# samples	Samples in cluster
# 8	24	pxrf-p90-15, pxrf-p26-42, pxrf-p26-39, pxrf-p26-31, pxrf-p26-30, pxrf-p26-28, pxrf-p26-26, pxrf-p26-25, pxrf-p27-53, pxrf-p27-50, pxrf-p27-47, pxrf-p27-46, pxrf-p27-45, pxrf-p27-44, pxrf-p27-43, pxrf-p27-40, pxrf-p27-39, pxrf-p27-29, pxrf-p27-23, pxrf-p27-21, pxrf-p27-2, pxrf-p27-15, pxrf-p27-14, pxrf-p25-9
# 9	23	pxrf-p90-20, pxrf-p26-43a, pxrf-p26-41, pxrf-p26-40, pxrf-p26-35, pxrf-p26-24, pxrf-p26-23, pxrf-p26-22, pxrf-p26-18, pxrf-p26-11, pxrf-p26-10, pxrf-p27-51, pxrf-p27-5, pxrf-p27-3, pxrf-p27-27, pxrf-p27-17, pxrf-p27-13, pxrf-p27-10, pxrf-p25-7, pxrf-p25-51, pxrf-p25-39, pxrf-p25-10, pxrf-p25-1
# 10	18	pxrf-p26-9, pxrf-p26-8, pxrf-p26-32a, pxrf-p26-32, pxrf-p26-22a, pxrf-p26-21, pxrf-p26-20, pxrf-p26-19, pxrf-p26-16, pxrf-p26-15, pxrf-p26-12, pxrf-p27-8, pxrf-p27-6, pxrf-p27-12, pxrf-p27-1, pxrf-p25-58, pxrf-p25-29, pxrf-p25-11
# 11	10	pxrf-p26-37, pxrf-p27-9, pxrf-p27-56, pxrf-p27-28, pxrf-p27-26, pxrf-p27-16, pxrf-p25-8, pxrf-p25-36, pxrf-p25-34, pxrf-p25-19
# 12	4	pxrf-p27-19, pxrf-p25-6, pxrf-p25-20, pxrf-p25-2
# 13	2	pxrf-p25-55, pxrf-p25-3
# 14	7	pxrf-p90-8, pxrf-p90-4, pxrf-p90-22a, pxrf-p90-1, pxrf-p25-49, pxrf-p25-44, pxrf-p25-42
# 15	15	pxrf-p90-27, pxrf-p90-18, pxrf-p26-4, pxrf-p26-36, pxrf-p26-34, pxrf-p26-33, pxrf-p27-57, pxrf-p27-30, pxrf-p27-25, pxrf-p27-24, pxrf-p27-18, pxrf-p25-33, pxrf-p25-23, pxrf-p25-17, pxrf-p25-12
# 16	6	pxrf-p90-17, pxrf-p26-17, pxrf-p27-35, pxrf-p25-48, pxrf-p25-40, pxrf-p25-27
# 17	7	pxrf-p26-5, pxrf-p26-2, pxrf-p26-1, pxrf-p27-55, pxrf-p27-34, pxrf-p27-22, pxrf-p25-25
# 18	14	pxrf-p90-7, pxrf-p90-6, pxrf-p26-38, pxrf-p26-29, pxrf-p26-27, pxrf-p26-14, pxrf-p27-7, pxrf-p27-52, pxrf-p27-36, pxrf-p27-33, pxrf-p27-20, pxrf-p25-59, pxrf-p25-24, pxrf-p25-22
# 19	6	pxrf-p90-5, pxrf-p25-56, pxrf-p25-4, pxrf-p25-16, pxrf-p25-15, pxrf-p25-14
# 20	1	pxrf-p25-13

Table A.3: Clusters obtained using rates calculated.

# cluster	# samples	Samples in cluster
# 1	11	pxrf-p25-2, pxrf-p25-3, pxrf-p25-4, pxrf-p25-6, pxrf-p25-12, pxrf-p25-15, pxrf-p25-16, pxrf-p27-19, pxrf-p27-24, pxrf-p27-30, pxrf-p90-27
# 2	4	pxrf-p25-13, pxrf-p25-18, pxrf-p25-20, pxrf-p90-3
# 3	3	pxrf-p25-17, pxrf-p25-52, pxrf-p26-14
# 4	3	pxrf-p25-19, pxrf-p25-34, pxrf-p27-26
# 5	12	pxrf-p25-9, pxrf-p25-22, pxrf-p25-24, pxrf-p26-27, pxrf-p27-21, pxrf-p27-33, pxrf-p27-52, pxrf-p90-4, pxrf-p90-8, pxrf-p90-15, pxrf-p90-16, pxrf-p90-22a
# 6	11	pxrf-p25-8, pxrf-p25-23, pxrf-p25-33, pxrf-p25-36, pxrf-p25-60, pxrf-p26-33, pxrf-p26-34, pxrf-p27-28, pxrf-p27-54, pxrf-p27-56, pxrf-p27-57
# 7	26	pxrf-p25-1, pxrf-p25-7, pxrf-p25-39, pxrf-p25-43, pxrf-p25-56, pxrf-p26-10, pxrf-p26-11, pxrf-p26-15, pxrf-p26-18, pxrf-p26-22, pxrf-p26-23, pxrf-p26-24, pxrf-p27-3, pxrf-p27-5, pxrf-p27-10, pxrf-p27-13, pxrf-p27-17, pxrf-p27-51, pxrf-p90-12, pxrf-p90-20, pxrf-p90-21, pxrf-p90-22, pxrf-p90-23, pxrf-p90-24, pxrf-p90-25, pxrf-p90-28
# 8	5	pxrf-p25-27, pxrf-p25-40, pxrf-p25-48, pxrf-p27-35, pxrf-p90-26
# 9	5	pxrf-p25-32, pxrf-p25-42, pxrf-p25-49, pxrf-p25-55, pxrf-p26-38
# 10	11	pxrf-p25-14, pxrf-p25-25, pxrf-p25-50, pxrf-p26-1, pxrf-p26-2, pxrf-p26-4, pxrf-p26-5, pxrf-p26-6, pxrf-p27-55, pxrf-p90-6, pxrf-p26-7a
# 11	14	pxrf-p25-10, pxrf-p25-11, pxrf-p25-26, pxrf-p25-51, pxrf-p26-3, pxrf-p26-7, pxrf-p26-35, pxrf-p26-36, pxrf-p26-40, pxrf-p27-4, pxrf-p27-9, pxrf-p27-11, pxrf-p90-18, pxrf-p26-3a
# 12	12	pxrf-p26-9, pxrf-p26-12, pxrf-p26-16, pxrf-p26-17, pxrf-p26-19, pxrf-p26-20, pxrf-p26-21, pxrf-p27-6, pxrf-p27-12, pxrf-p90-17, pxrf-p26-22a, pxrf-p26-43a
# 13	13	pxrf-p25-29, pxrf-p25-53, pxrf-p25-58, pxrf-p26-8, pxrf-p26-32, pxrf-p26-37, pxrf-p27-1, pxrf-p27-8, pxrf-p27-16, pxrf-p27-18, pxrf-p27-25, pxrf-p90-5, pxrf-p26-32a

Continues on next page

Table A.3 (continued)

# cluster	# samples	Samples in cluster
# 14	11	pxrf-p26-28, pxrf-p26-42, pxrf-p27-2, pxrf-p27-22, pxrf-p27-29, pxrf-p27-34, pxrf-p27-39, pxrf-p27-40, pxrf-p27-46, pxrf-p27-50, pxrf-p90-7
# 15	23	pxrf-p25-44, pxrf-p25-59, pxrf-p26-25, pxrf-p26-26, pxrf-p26-29, pxrf-p26-30, pxrf-p26-31, pxrf-p26-39, pxrf-p26-41, pxrf-p27-7, pxrf-p27-14, pxrf-p27-15, pxrf-p27-20, pxrf-p27-23, pxrf-p27-27, pxrf-p27-36, pxrf-p27-43, pxrf-p27-44, pxrf-p27-45, pxrf-p27-47, pxrf-p27-53, pxrf-p90-1, pxrf-p90-19